THE UNIVERSITY *of* EDINBURGH

Optical Coherence Tomography to Detect Macrophages in Atheroma in vivo

Clara Vergez

PhD

The University of Edinburgh

2020

DECLARATION

I can confirm that this thesis has been entirely composed by myself. The work represents experiments and studies undertaken by me, whilst working within a multidisciplinary team and any contributions from others has been clearly indicated. None of this work has been submitted for any other degree or professional qualification.

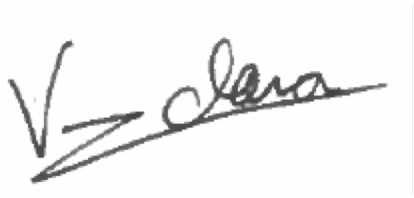

Clara Vergez

Dedicated to Tom

ABSTRACT

Introduction. Macrophages play a key role in atherosclerotic plaque instability, they engender plaque rupture, leading to thrombosis and myocardial infarction. Their detection in coronary artery plaques would enable stratification of patients for better treatment of "vulnerable" phenotypes. Intra-coronary Optical Coherence Tomography (OCT) enables visualisation of vulnerable plaque morphology and has the potential to detect the signal variance created by increased numbers of macrophages.

Aims. Our aim was to enhance the detection of macrophages using OCT in combination with intracellular contrast agents; and to demonstrate it in-vitro, ex-vivo and in-vivo. This was first endeavoured using clinically approved ultra-small superparamagnetic particles of iron oxide (USPIOs): an MRI contrast agent which is readily uptaken by macrophages in coronary plaques. The second approach was to design a novel OCT contrast agent based on different lanthanide ions with either a carbonate or fluoride structure.

Methods. A "phantom" artery model was designed and 3D printed for standardised in-vitro imaging with intra-coronary OCT. Particle-laden macrophages were tested in this system to determine OCT contrast enhancement. Cell viability assays were performed to determine toxicity of novel lanthanide particles. Aortic plaques of Apo-lipoprotein E knockout mice, treated with USPIO or saline were OCT imaged and sectioned for histological analysis. Patients presenting with acute coronary artery disease were randomised to receive USPIO or saline treatment, followed by OCT imaging of the culprit plaque and non-culprit control. The local pixel Standard Deviation (SD) of OCT images were processed in Matlab as a metric of contrast enhancement. A local SD hotspot visualisation tool was developed in Matlab for use with the phantom, murine and human OCT images.

Results. In all 7 phantoms, USPIO-laden macrophages significantly increased the mean SD compared to untreated macrophages ($p<0.001$). USPIO treated mouse plaques (n=3) showed significantly higher mean SD than control plaques (n=3) ($p<0.05$). USPIO treated patients (n=8) demonstrated a significantly increased mean SD compared to control patients (n=10) in culprit and non-culprit plaques ($p<0.05$). Within patients the mean SD was significantly higher for culprit compared to non-culprit plaques in both USPIO and control groups. The initial OCT screening of 10 novel lanthanide particles revealed the carbonate structures to be

most efficacious for contrast enhancement compared to the fluoride ones. Phantoms made with particle-laden macrophages revealed the Gadolinium carbonate particle with Polyacrylic acid coating to have the highest mean SD increase compared to untreated macrophages. This particle also showed low levels of cell toxicity.

Conclusions. USPIO administration was associated with a significant increase in OCT contrast in a novel in-vitro phantom model, an ex-vivo atherosclerotic mouse study and in a human clinical trial. USPIO enhances the detection of macrophages and may facilitate patient stratification. Additionally, novel OCT contrast agents have been made which show great potential for further enhancing macrophage detection in this same context.

LAY SUMMARY

The heart muscle's oxygen is carried by blood vessels called coronary arteries. Fat can build up inside the wall of these arteries, forming a dangerous package called a plaque. If the wall breaks and the content of the plaque meets the blood, a clot will quickly form and block the vessel, causing a heart attack. The muscle is no longer getting its oxygen supply from the coronary arteries and it starts to die. It won't pump the blood properly and the rest of the body will not be getting the oxygen it needs - if not treated immediately, the patient could pass away. One of the main causes of the plaques breaking are immune cells called macrophages. These cells enter the plaque and start to break down the fibre which keeps it intact and separate from the blood. The following thesis focusses on finding a way to tag these macrophages so we can find the plaques which are more likely to cause a heart attack. This would help cardiologists find patients which are at higher risk of suffering a future heart attack so that they can treat them more appropriately to avoid it. That way, those fatty plaques can be reduced in size and the macrophages may be stopped from entering and breaking them open. The research was centred around Optical Coherence Tomography (OCT), an imaging technique which works in a similar way to ultrasound but using light waves instead of sound waves to create grayscale images of the layers of the artery wall. Different metal nanoparticles were used to tag macrophages and their detectability was tested in the lab, in mice and in human patients with a clinical OCT system. A few of the tested particles were found to be significantly better at detecting macrophages on OCT images compared to no treatment. These particles therefore have great potential to detect "vulnerable plaques" in patients.

ACKNOWEDGEMENTS

My PhD journey has filled these past 5 years with extreme highs and extreme lows, I have many many people to thank for helping me through it in a multitude of ways.

I would first like to thank my supervisors, Dr Pierre Baganinchi, Dr Marc Dweck and Prof Marc Vendrell for their insight and support throughout my PhD project. Pierre, you never lost faith in me and were always extremely encouraging and supportive, I would definitely not have completed my thesis were it not for your kindness and emotional support in the last few months of year 5. Marc D, your excitement, positivity and expertise in all things clinical cardiology was very much appreciated. Thank you also for being so understanding and accommodating of my tight schedule in the last two weeks before submission, I really appreciated your speedy edits! Marc V, thank you for creating a fun and supportive environment in the DynaFluors group which I thoroughly enjoyed being a part of and thank you for all your chemistry expertise and support for the work in Chapter 6.

Thank you to Dr Nick Cruden, Dr Simon Wilson and Dr Andrew Mitchell for all your amazing work on the clinical study included in this thesis. Thank you to Dr Rodger Duffin for coordinating and overseeing the care and treatment of the mice used in this thesis. And a special thank you to Dr Mark Miller for patiently teaching me how to dissect and excise mouse hearts and aortas. For helping me figure out the logistics of OCT imaging the tiny mouse aortas I have to thank Simon, Rodger and Mark again. Last but not least, I am extremely thankful to Dr Calum Gray at the Clinical Research Imaging Centre for all the work on the image analysis software, without which no part of this project would have been possible!

I can't extend enough thanks to the OPTIMA programme and all the people involved. In particular I want to thank Dr Jean O'Donoghue who is just so understanding and supportive. Jean, you really pulled me out of a tough spot with my writing by just being there to speak to, giving me practical info and most importantly helping me open up to my supervisor when I didn't feel able to. Thank you also to the MRC and the EPSRC for funding the OPTIMA programme which has provided me with awesome opportunities including entrepreneurship courses, a funded placement and numerous social events with the lovely big OPTIMA family, many members of which have become lifelong friends.

To all my friends, old and new: Jess, Katie, Jo, Philip, Shauni, Duncan, Andrea, Mela, Dominic, Rachel, Cecilia, Mairi and Jen, thank you all for being essential sources of distraction / entertainment / moral support in the form of board game nights, dinners, wedding parties, zoom quizzes, walks and cycling adventures! In particular, Jess and Duncan, you have been the two friends I leaned on the most when I was at my lowest, you've listened, given helpful words and lots of love and for that I will be forever grateful. Jess, in my last two weeks of writing up you were such a huge help. Thank you for showing me the forest app (which totally saved me), bringing me baked goods as writing fuel, dropping by to just say hi and sending me a lovely message of support every single morning of my last week, it really meant a lot to me.

I want to thank my amazing parents who have always been incredibly loving and supportive throughout all my endeavours. Maman, I really really appreciated all the talks we had about my PhD and thesis writing, you helped me externalise and make sense of my feelings and I love that we have such a close relationship. Also, your zoom yoga classes have meant a lot to me, they connected us (and friends and family!) through exercise during lonely and scary lockdown times. Papa, your positivity and enthusiasm for so many things is incredibly infectious. Many times you have brightened up my day with a hilarious text message or photo and I don't think you even realised it. I loved our many chats about my flat, DIY, the pets, gardening and cycling when you knew I didn't feel able to talk about the PhD.

Finally I want to thank Tom, you are my whole world and I could not have found a better person to have by my side through life and through the PhD. Thank you for being number one in my support system: always there to listen, console and comfort me. You never got tired or frustrated with me, you were always unconditionally loving and caring and that is exactly what I needed. You have filled my life with so much happiness and I can't wait to celebrate with you, Javi and Maeby (my perfect little family)!

ABREVIATIONS

a.u.: Arbitrary Units

ACS: Acute Coronary Syndrome

Apo: Apolipoprotein

$ApoE^{-/-}$: ApoE knockout mouse model

CAD: Coronary Artery Disease

DMSO: Dimethyl Sulfoxide

DPBS: Dulbeco's Phosphate Buffer Saline

Dy: Dysprosium

Er: Erbium

FD-OCT: Fourier-Domain Optical Coherence Tomography

Gd: Gadolinium

HDL: High-Density Lipoprotein

HMMs: Human Monocyte derived Macrophages

IV-OCT: Intra-Vascular Optical Coherence Tomography

IV-US: Intra-Vascular Ultrasound

LDL: Low-Density Lipoprotein

LDL-R: Low-Density Lipoprotein Receptor

$LDL\text{-}R^{-/-}$: Low-Density Lipoprotein Receptor knockout mouse model

MI: Myocardial Infarction

MMP: Matrix-Metalloproteinases

MSD: Mean Standard Deviation

Nd: Neodymium

NSD: Normalised Standard Deviation

OCT: Optical Coherence Tomography

PAA: polyacrylic acid

PCI: Percutaneous Coronary Intervention

PEG: polyethylene glycol

PEI: polyethyleneimine

RAW cells: RAW264.7 murine macrophage-like cell line

ROI: Region of Interest

SD: Standard Deviation

SMC: Smooth Muscle Cell

SS-OCT: Swept-Source Optical Coherence Tomography

TCFA: Thin-Capped Fibroatheromas

TD-OCT: Time-Domain Optical Coherence Tomography

TEM: Transmission Electron Microscopy

TF: Tissue Factor

USPIO: Ultra-small Super-paramagnetic Particles of Iron Oxide

VLDL: Very Low-Density Lipoprotein

WT: Wild-Type

Yb: Ytterbium

CONTENTS

LIST OF FIGURES

1 CHAPTER ONE: INTRODUCTION

1.1 CORONARY ARTERY DISEASE AND ATHEROGENESIS

1.1.1 Introduction and definitions

Coronary Artery Disease (CAD), also named Coronary Heart Disease is the deadliest type of cardiovascular disease, and the leading cause of death worldwide[1,2]. As of 2020 CAD is responsible for the death of 14% of British men and 8% of British women[2]. Whereas the term "cardiovascular diseases" encompasses all diseases involving the heart and blood vessels, CAD more specifically designates a group of diseases caused by impaired blood flow (ischemia) from the coronary arteries to the heart muscle (myocardium) which can then become damaged due to the lack of oxygen (hypoxia)[1–5]. The coronary arteries descend from the aorta, wrap around the heart (Figure 1-1) and provide blood (and thus oxygen) to the myocardium. The coronary arteries are relatively narrow vessels which when restricted by atherosclerosis can cause the patient intense chest pain referred to as angina.

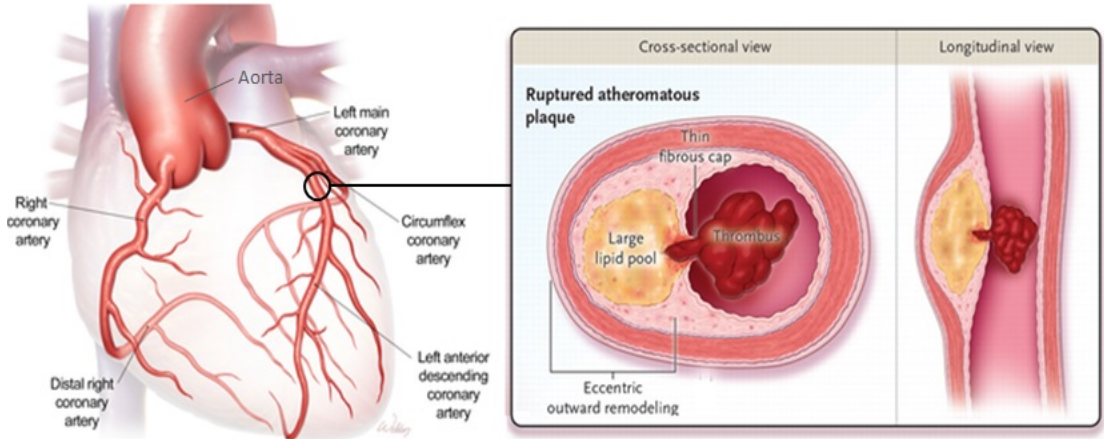

Figure 1-1: Diagram showing the coronary arteries and a rupturing atheromatous plaque which has formed in the left anterior descending coronary artery. This artery has undergone eccentric outward remodelling to make space for the plaque which allows there to be minimal narrowing (i.e. stenosis) of the artery which can be seen on the longitudinal view. However not all plaques are non-stenotic, they can be more or less stenotic depending on many factors such as composition, age, history of rupture and repair. Adapted with permission from ([5]), Copyright Massachusetts Medical Society.

It is useful to consider CAD in two forms: stable and unstable disease. Stable disease is characterised by fixed narrowing in the artery which prevents adequate blood flow reaching the heart muscle during exercise[5–7]. This causes stable angina which is defined as intense chest pain which occurs during physical activity or stress[5–7]. Unstable disease or Acute Coronary Syndromes (ACS) are caused by inflamed atherosclerotic lesions which can rupture

and then precipitate the formation of blood clots in the arteries[5–7]. These block off blood supply to the heart muscle, causing prolonged ischemia and eventually myocardial infarction[5–8]. The character of the pain (unstable angina) is different: frequently occurring at rest and being prolonged and associated with other features such as sweating, nausea and vomiting[7,8]. When the coronary arteries get blocked by a thrombus (blood clot) it causes ischemia to the myocardium which, if prolonged, results in heart muscle death and myocardial infarction (MI)[5–7]. It should also be noted that the difference between MI with and without ST-segment elevation has been overlooked here for the sake of simplicity.

Underlying all of these CAD syndromes is the process of atherosclerosis: the formation of fibro-fatty plaques in the artery wall causing thickening, hardening and sometimes narrowing of the walls[4,9,10]. The formation of these atherosclerotic (or atheromatous) plaques, also known as atheromata or atherosclerotic lesions is a complex process with complex potential repercussions.[4,9,10]

1.1.2 Atheromata: formation and progression

The formation of plaques begins with a change in the permeability of the endothelial cells lining the arterial cavity, enabling LDL (low-density lipoprotein) from the blood to migrate into the tunica intima of the coronary artery wall[4,11,12]. Usually these endothelial cells, shown in green on Figure 1-2 (A), do not enable attachment of leukocytes (white blood cells), however, in response to certain stimuli (such as pro-inflammatory mediators), and because of the presence of LDL, they start expressing adhesion molecules which bind to monocytes and T cells, enabling their extravasation to the intima (Figure 1-2 (A)) [4,11–13]. Once inside the arterial wall, monocytes differentiate into macrophages and then avidly phagocytose (ingest) free LDL to become foam cells (a term employed to describe their foamy appearance)[4,12,13]. Additionally, smooth muscle cells (SMCs) from the tunica media of the arterial wall migrate into the intima and start to produce extracellular matrix proteins such as collagen and elastin which together with the newly migrated SMCs produce a fibrous cap which covers the plaque, imparting stability and reducing the risk of plaque rupture and MI (Figure 1-2 (B))[4,12,13].

Within the new plaque, macrophages and SMCs can die and their inefficient clearance leads to the accumulation of extracellular lipids which form the lipid or necrotic core of the plaque (Figure 1-2 (C))[4,12–14]. Moreover, plaque macrophages produce pro-coagulant factors such as tissue factor (TF) which render the necrotic core thrombogenic (i.e. prone to cause

coagulation of the blood)[15,16]. Many studies ([17–20]) have also shown that the inflammatory macrophages and foam cells of the plaque, which are activated by plaque T cells, produce matrix-metalloproteinases (MMP) which break down collagen in the fibrous cap[4,12,13]. This, along with the production of other factors which can induce the death of plaque SMCs or reduce their collagen production, leads to the thinning and weakening of the fibrous cap[4,12,13]. Eventually the cap may rupture and expose the thrombogenic necrotic core, resulting in thrombosis and potentially MI[4,12,13] (Figure 1-2 (C)).

Atheromata (plaques) cause clinical syndromes in two ways. Firstly, stable plaques can cause stenosis of the vessels which limits the coronary arterial flow, leading to ischemia and symptoms of angina. Secondly, unstable inflamed plaques can rupture, triggering thrombus formation and vessel obstruction either at that site or in a downstream vessel via distal embolization[12]. Importantly not all plaque rupture events cause MI, with some simply resulting in subclinical plaque growth and healing. This depends in part on the thrombogenicity of the plaque contents and the stickiness of the blood. The latter is in turn dependent on multiple factors, for example plasminogen activator inhibitor-1 (PAI-1), which reduces the blood's natural ability to combat persistent thrombi, the levels of which are increased in obese and diabetic patients[13]. Different patients therefore have different predispositions to ACS dependent on their plaque burden, plaque type and blood thrombogenicity[12,13].

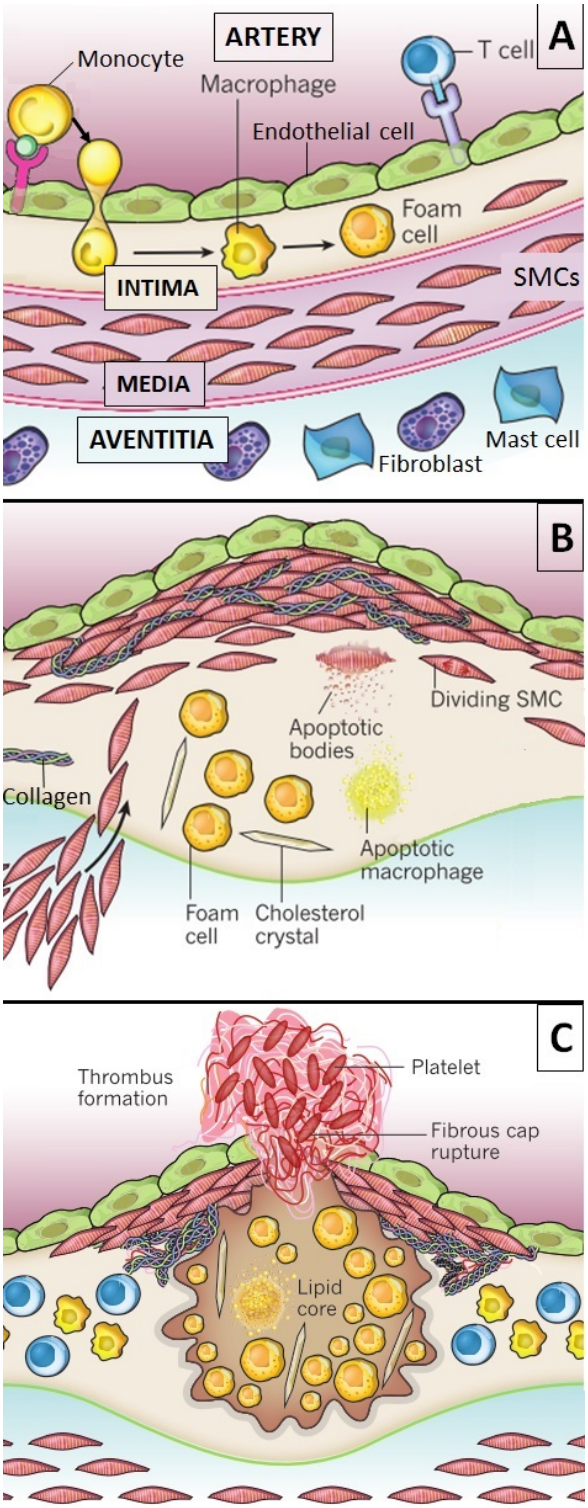

*Figure 1-2: Diagram showing the different stages of atheroma formation starting from the top and progressing through to rupture of the plaque at the bottom. **(A)** Macrophages and T cells infiltrate the tunica intima of the artery wall, initiating plaque formation. **(B)** SMCs (smooth muscle cells) migrate from the tunica media to the tunica intima and produce collagen to form the fibrous cap which closes the plaque off from the blood flow. **(C)** The*

fibrous cap ruptures and leads to thrombus formation. Adapted with permission (rightslink license number 4961350222324) from ([12]), Copyright Springer Nature.

1.1.3 The lipoprotein metabolism and animal models of atherosclerosis

Animal models have been and still are an extremely useful tool to our understanding of the chronic inflammatory disease that is atherosclerosis. The most commonly used animal models of atherosclerosis are mice, rabbits, pigs and a few different species of nonhuman primates[21]. As was touched on previously, atherosclerosis involves both the innate and adaptive immune systems which get activated in response to hyperlipidaemia: raised levels of lipids or lipoproteins in the blood[12,21–23]. The lipoprotein metabolism is vast, complex and differs between species, only a few key elements will be covered here.

In short, lipoproteins are complexes formed between lipids (cholesterol, phospholipids, cholesterol esters and some triacylglycerols) and proteins called apolipoproteins[22–24]. These complexes travel through the blood and extracellular fluids and have different destinations depending on their type[22–24]. The four main types of lipoproteins are LDL (low density lipoprotein), HDL (high density lipoprotein), VLDL (very low density lipoprotein) and chylomicrons and each of these are made up of different types of apolipoproteins (apo) [22–24]. HDL, often deemed "the good cholesterol" is part of the reverse transport pathway, it picks up excess cholesterol and delivers it to tissues in need[22–24]. Conversely, unless LDL is taken up by cells in the liver through the LDL receptor (LDL-R) it can accumulate in artery walls and increases the risk of coronary artery disease[22–24].

In humans, LDL is the primary lipoprotein while in wild type (WT) mice it is HDL[21,25]. This, as well as a few other differences in cholesterol metabolism is the reason why WT mice are naturally atheroresistant, even when fed a high fat diet[21,25]. However, mouse models of atherosclerosis are most easily made by knocking out apolipoprotein E (apoE) or the LDL receptor[21,25]. ApoE is the primary ligand for the LDL receptor on hepatic cells and is a key component of VLDL[26,27]. This means that when apoE or LDL-R is knocked out, there is a significant reduction in uptake of VLDL by the liver which results in its accumulation in the blood[26,27]. Because VLDL in the blood eventually gets cleaved into LDL, lower levels or dysfunction of either apoE or LDL-R leads to higher LDL levels in the blood which in turn increases the risk of atherosclerosis. Indeed, apoE$^{-/-}$ mice and LDL-R$^{-/-}$ mice develop hypercholesterolemia and atherosclerosis in the aorta when fed a high fat diet[21,25]. In humans

there is a genetic disease called familial hypercholesterolemia which is caused by the dysfunction of the LDL-R and significantly increases the risk of cardiovascular disease[28].

In contrast to the mouse, larger animals have more similar lipoprotein profiles to humans and therefore can have advantages for certain studies[21,25]. In particular, pigs develop spontaneous atherosclerosis in the coronary arteries which can be accelerated with a high cholesterol diet, making them an attractive model for many studies[21,25]. In rabbits, a natural strain exhibiting familial hypercholesterolemia was identified in 1980 and selectively bred by Dr Watanabe to produce rabbits with coronary thin capped fibroatheromas which spontaneously developed myocardial infarction[29,30]. This strain; the Watanabe heritable hyperlipidaemic (WHHL) rabbit has a defect in the LDL receptor and was instrumental in the discovery of the cause of human familial hypercholesterolemia 3 years later[31]. A number of non-human primates are also used for atherosclerosis studies thanks to the close similarities of their lipoprotein profile to that of humans[21,25]. However, all these large animals are more expensive in price and upkeep and atherosclerosis takes longer to develop than in mice[21,25]. For these reasons, as with many other disease models, mice have been the favoured species for the study of atherosclerosis[21,25].

1.1.4 Revascularisation procedures for treatment and prevention

There are many different CAD treatments such as anti-platelet therapies to thin the blood, LDL-lowering medication to stabilise the plaque and importantly, lifestyle measures to modify risk factors such as high blood pressure, obesity and smoking[12,13]. These are often used in combination, depending on the specific syndrome and predisposition of patients[12]. Whilst these represent the most effective forms of treatment, due to length constraints they will not be expanded further upon here. Instead the focus will be on coronary artery revascularisation procedures that are required in some patients with advanced or unstable forms of coronary artery disease.

Coronary angiography is an x-ray based technique developed in the 1950s which enables the visualisation of blood vessels thanks to the injection of radio-opaque contrasting agent (Figure 1-3). The advent of this technique lead to the development of coronary artery bypass surgery, a procedure whereby vessels from elsewhere in the body are grafted distal to sites of stenosis. Subsequently, coronary angioplasty was developed: a non-surgical procedure which involves the inflation of a balloon at the site of stenosis (to enlarge the vessel to its original size) and subsequent stent placement (Figure 1-3), implantation of a metallic scaffold

to keep the artery permanently open[32]. Angiography permits the visualisation of artery sections with the most severe stenosis, that can then be targeted with revascularisation therapies[32]. In unstable patients with MI, stent placement is a quick and effective method of opening up the artery and restoring blood flow. Moreover it can help stabilise the plaque and help prevent recurrent MI[32,33]. In patients with stable angina, stent implantation is an effective method of relieving severe symptoms and therefore improving quality of life.

However, in major randomised trials, stent placement in severe stable stenoses has not proved successful in reducing the risk of subsequent MI[32,33]. Surprisingly, angiographic studies of patients before and after they suffered MI demonstrated that the culprit plaques which gave rise to the occluding thrombus were most commonly non-obstructive in nature (luminal stenoses <70%) and would not have warranted revascularisation procedures[33–37]. Culprit plaques do however have certain characteristics when analysed on histology or with imaging techniques. These include a large necrotic lipid core, a thin fibrous cap, inflammation, micro-calcifications and a very thin fibrous cap. Whilst they often have a large plaque volume they are frequently not stenotic because of outward (positive) remodelling of the artery (Figure 1-1)[12,32,38,39]. Improved techniques are therefore required, that assess both lesion severity and plaque type. The ability to identify plaques with a thin fibrous cap and extensive inflammation would be of particular clinical use for assessing the severity of patient disease and potentially in improving the prediction of future clinical events.

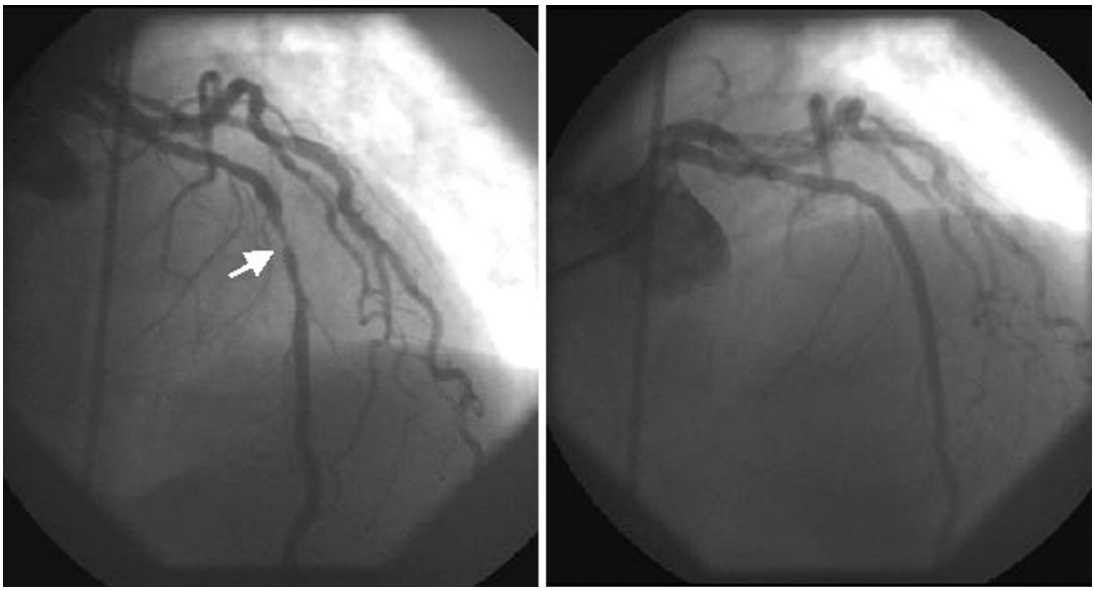

Figure 1-3: Coronary angiogram of a 48 year old woman with unstable angina, showing severe stenosis in the mid-left anterior descending coronary artery marked by the arrow (left

picture), successfully stented in the right picture. Reused with permission (rightslink licence num 4961351450013) from ([7]), copyright BMJ publishing group Ltd.

1.1.5 The Vulnerable Plaque and the Vulnerable Patient

Each of the pathological features that characterise the culprit represents a potential imaging target that might be used to identify plaques at high risk of future rupture (the vulnerable plaque). In 1989, James E. Muller first described dangerous lesions as "vulnerable plaques"[40] which were soon after defined as having a large lipid core and a thin fibrous cap with high levels of macrophage infiltration[41,42]. This has since been a subject of intense research and whilst we now have an array of invasive and non-invasive imaging techniques capable of identifying all the individual components of the "vulnerable plaque"[43] (see Figure 1-4), this strategy has to date failed to improve the clinical care of patients with atherosclerosis[44,45]. A detailed description of the vulnerable plaque literature is beyond the scope of this thesis but a summary figure is provided (Figure 1-4) and reference made to several excellent review articles on the subject[42,44–46].

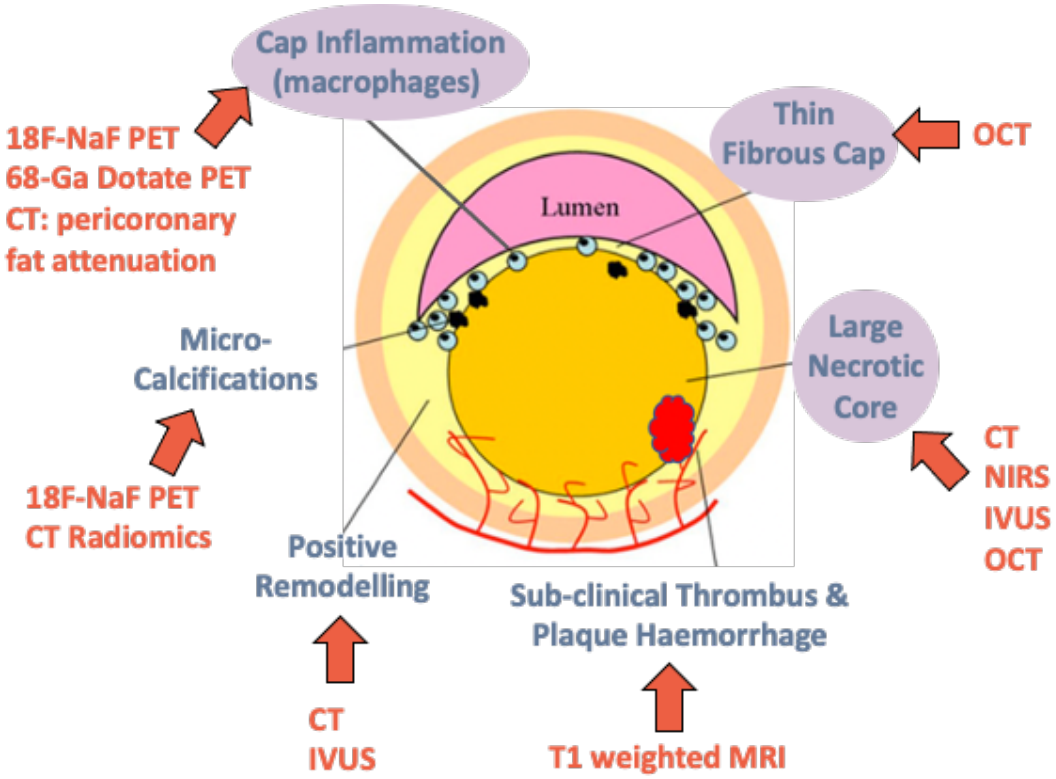

Figure 1-4: Summary of the key vulnerable plaque characteristics and the imaging modalities which can detect each of them. Circled are the three traditionally defining features of the vulnerable plaque.

Why then has vulnerable plaque imaging failed to impact clinical practice? In brief the positive predictive value of vulnerable plaque characteristics identified to date has been too low to be of clinical use[45]. In numerous prospective studies the vast majority of vulnerable plaques identified do not go on to cause myocardial infarction, but rather heal or rupture sub-clinically[47–51]. Plaque rupture and healing are in fact most often asymptomatic but lead to progressive stenosis[52,53].The concept, however, works better at the patient level. Patients in whom vulnerable plaques are identified consistently appear at higher risk than patients with more stable patterns of disease[54,55]. The vulnerable plaque identified at the time of imaging may not itself cause an event, but the patient is prone to developing these unstable plaques, one of which may well cause an event in the future.

On this background, attention is focusing upon methods to identify vulnerable plaques with improved positive predictive value, potentially by combining more than one high risk characteristic. Indeed, as is presented in Figure 1-4, no single imaging technique can identify the 3 most important vulnerable plaque characteristics at once. However, OCT has a high potential in this regard as it enables easy measurement of the fibrous cap, detection of a lipid pool and early data suggests it may also be able to identify the third key vulnerable plaque feature: inflammation[56,57]. This is of particular importance given the clear correlation between markers of inflammation and disease severity and risk of ACS[58]. Additionally, OCT, in contrast to PET-CT, MRI and NIRS is routinely used during coronary intervention to assess lumen size before stent placement. The precise detection of a high burden of “vulnerable plaques” could perhaps aid in the identification of “vulnerable patients” who would benefit from more expensive anti-inflammatory treatments. Numerous recent clinical studies have shown that targeted anti-inflammatory therapy yields significant reductions in future major cardiovascular events[59–63]. This idea of stratification of ACS patients is a big incentive for better detection of the “vulnerable plaque” profile in vivo, or more importantly, simply detecting high macrophage burden in plaque caps. Another benefit to the real-time visualisation of cap inflammation would be easier and faster identification of culprit plaques during coronary intervention. It is with these aims in mind that OCT is introduced in section 1.2 and discussed in section 1.3 as a technique with high promise for the precise detection, quantification and visualisation of cap macrophages.

1.2 Optical Coherence Tomography (OCT)

1.2.1 Introduction and history

Optical coherence tomography (OCT) is a medical imaging technique analogous to ultrasound imaging, using near-infrared light as opposed to sound to create an image of tissue[64]. Contrarily to OCT, ultrasound directly measures the time taken for an echo to reflect back from tissue structures to obtain depth information[65]. In OCT however, the velocity of light is too high for the electronic measurement of optical echoes. Instead, an interferometer is used to measure the back-scattered light from within the tissue by comparing it to light which has travelled along a known reference path[66] (as will be explained in section 1.2.2). Although ultrasound can image structures deeper within the tissue than OCT can, OCT achieves a much higher resolution, as is demonstrated in Figure 1-5 and confirmed in quantitative measurements[56,67,68]. An additional advantage over ultrasound is that OCT does not require contact with the tissue, a property which has proved particularly advantageous when imaging the eye[65].

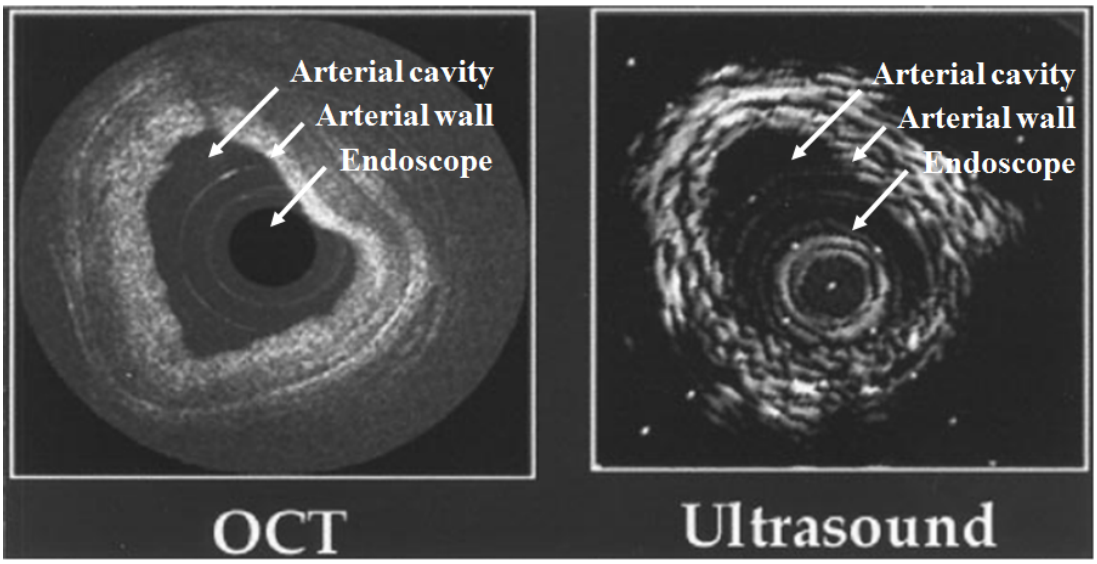

Figure 1-5: Comparison of Ultrasound and OCT imaging of the coronary artery with intravascular endoscope systems. Images reused with permission from ([67]) © [1999] IEEE.

Because OCT functions in a similar way to ultrasound, most of the terminology has been borrowed from it. OCT produces depth profiles of the tissues, named A-scans (after ultrasound A-scans), a technique first developed in interferometry in 1986 to measure eye length[66,69,70]. These A-scans are then put together to form a 2D image of a tissue slice named a B-scan[66,71] examples of which are shown in Figure 1-5 for ultrasound and OCT in a coronary

artery. In 1991 the first in vitro B-scan image of the eye acquired by OCT was published by Huang *et al.*[64] and 2 years later the first in vivo images of the eye were published by Fercher *et al.*[72] and Swanson *et al.*[73]. Although OCT was initially conceived for retinal imaging, the first publication describing the system in 1991[64] already mentions the application of OCT to arterial imaging and this is later addressed more specifically in 1996[67,74,75]. Intracoronary OCT has since made major developments with the shift from time-domain OCT (TD-OCT) to Fourier-domain OCT (FD-OCT) which enabled a great improvement of image resolution as well as acquisition time,[75] to be described in the following section.

1.2.2 Basic Theory

Optical interferometry forms the basis of OCT and it is itself based on the interference between two light beams[65]. Interference refers to the phenomenon which occurs when two waves come together and merge to form a wave of greater amplitude (constructive interference) or lower amplitude (destructive interference). For instance, when two waves with the same frequency (or wavelength) are combined they undergo constructive interference if they are in phase or destructive interference if they are out of phase (Figure 1-6)[65]. Two light beams which are in phase will have an amplified interference signal (constructive interference) only if they are still in phase when they recombine and this will only occur if they have both travelled the same "optical path" i.e., neither of them has encountered an obstacle which changed their distance travelled[65].

However, this only applies to monochromatic light beams (lasers), which are composed only of waves which each have the same wavelength and are in phase, this is named "coherent light"[65] (Figure 1-6). Moreover, there exist many light sources (the sun, a light bulb) which, contrarily, are "incoherent": they are composed of many waves of different frequencies[65] (Figure 1-6). Most light beams are "partially coherent": they are coherent only periodically and the rest of the time they are incoherent. This means that for a given length of time (the coherence length) all the waves in the beam are identical but outside of this length the waves have different frequencies and phases. Additionally, when light is referred to as "low coherence" this infers that it is partially coherent and has a very short coherence length. Therefore, when two identical partially coherent light beams merge, signal amplification due to constructive interference solely occurs if the optical paths that each beam has travelled differ by a length inferior to the coherence length of the beam[65]. This is the principle by which

interferometers function to determine the distance travelled by backscattered light from a sample[65].

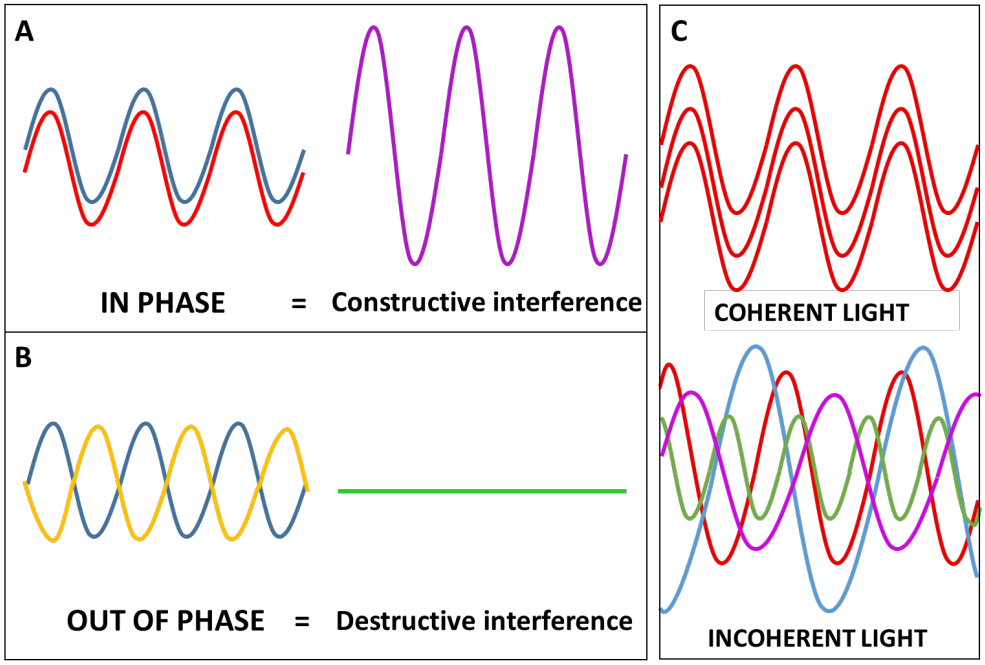

Figure 1-6: (A) Constructive interference: two waves in phase (red and blue) will combine to form a wave of greater amplitude (purple). (B) Destructive interference: two waves out of phase (blue and yellow) will combine to form a wave of lower amplitude (green). (C) Coherent light is composed of multiple waves that are in phase and have the same wavelength whereas incoherent light is made up of waves of different wavelengths and phases.

An interferometer and specifically Michelson's interferometer splits the beam of light which it receives from a source (E_{src}) into two identical beams, the first one, the reference beam (E_{ref}) is directed to a mirror and the other is directed towards the sample[65] (Figure 1-7). The interferometer then receives the reference beam back from the mirror as well as the sample beam which has partially been back-scattered from the sample (E_{sam}), these two are recombined and the interference is measured[65] (Figure 1-7). In OCT, low coherence light is used as the source because interference will only be detected during short periods or "coherence lengths" which correspond to a very small section of tissue while the rest of the tissue above or below this section will be, so to speak, ignored, because the light is incoherent by the time it hits it (so no interference pattern will be detected). In this way, information about the depths of the tissue structures can be gained from the backscattered light. Conversely, if coherent light was used instead, amplified interference signals would be received from all different depths all at the same time and these would not be able to be distinguished.

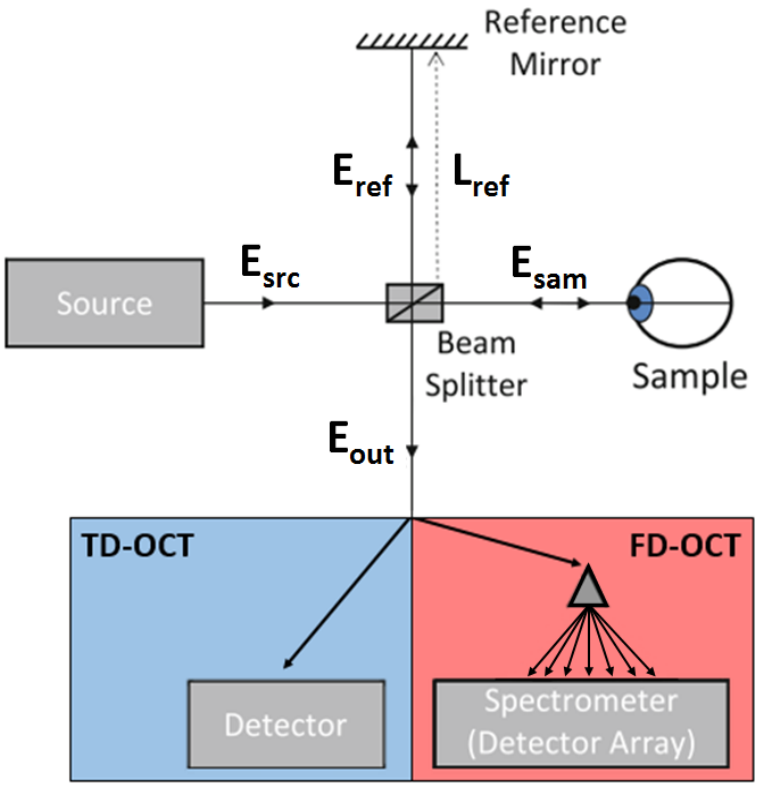

Figure 1-7: Diagram of the Time Domain (TD) and Fourier Domain (FD) OCT systems. In the TD-OCT system a simple detector is used to receive the recombined light beam and in the FD-OCT system everything is the same except a spectrometer is used for detection and the reference mirror is fixed.

There are two main different OCT system, the most simple to understand is time-domain OCT (TD-OCT) which is schematised along with Fourier-domain OCT (FD-OCT) in Figure 1-7. In TD-OCT a standard detector is used to receive the light beam (E_{out}) composed of the combination of the beam back-scattered from the sample (E_{sam}) and the beam back-scattered from the reference mirror (E_{ref})[65]. In this system, the reference mirror itself is mobile and it's distance from the beam splitter (L_{ref}) is adjusted initially to make it equal to the distance to the surface of the sample and then it is increased in the imaging depth range of interest to acquire an A-scan profile of the depth of the sample[65]. However, in FD-OCT systems the reference mirror is kept fixed and the backscattered light from the whole depth range of the sample is processed at the same time. This can be achieved in two ways, the standard FD-OCT has a spectrometer instead of a simple detector as is pictured in Figure 1-7[65]. The second FD-OCT system called Swept Source OCT (SS-OCT) has a simple detector (no spectrometer) but uses a tunable light source which sweeps the frequency range of interest[65]. Both FD-OCT systems

(FD and SS) exploit interference patterns in the spectral (or Fourier) domain rather than the time domain[65]. Since the arrival of FD-OCT systems in 1995 it was clear that the speed of acquisition was much faster than that of the TD-OCT system but in 2003 it was shown that the sensitivity of these systems is also far superior to that of the TD-OCT system[76–78].

1.3 Intracoronary OCT: vulnerable plaques and macrophage detection

Intracoronary OCT systems are composed of a single fibre optic wire (within a guide-wire) which emits light and simultaneously records the light back-scattered from the tissue. The wire also rotates (to get a 360 degree record of the artery wall) and gets pulled back along the artery, within the guide-wire (which itself stays fixed)[68]. This creates a series of circular 2D cross-sectional images of the artery lumen and wall, they can be combined to create a 3D view of the vessel. Intracoronary OCT systems are SS systems (see section 1.2.2)[57] which use a near-infrared light source with central wavelengths ranging from 1250 to 1350nm[68]. This is the case because light absorption by tissue is at its lowest between 700 and 1300nm in what is named the "window of transmission" which allows higher scattering and therefore more information about tissue contents[66,67]. Using light at this wavelength restricts the tissue penetration to 1-3 mm as opposed to 4-8mm with intravascular ultrasound (IVUS)[68]. Nonetheless, the axial resolution of intracoronary OCT (12-18µm for most recent and currently used clinical system by St. Jude) is far superior to that of IVUS (150-200µm)[68]. This is also true of the lateral resolution which is 20-90µm for OCT and 150-300µm for IVUS[68] and these resolution differences are apparent in Figure 1-1. Due to blood being non-transparent and highly light scattering, OCT imaging of the artery wall requires a blood-free view[68,75]. Therefore, an intracoronary injection of x-ray contrast is administered during imaging in order to clear the blood pool[68,75]. The vessel size suitable for OCT imaging ranges from 2 to 3.75mm in diameter, the upper limit being restricted by the actual depth imaging capacity of OCT[68].

1.3.1 Detecting vulnerable atherosclerotic plaques

As was explained previously, the extent of stenosis caused by a plaque provides an incomplete indication of its vulnerability to rupture[57]. Indeed, angiography by itself cannot be used to predict plaque rupture. It is hoped that OCT may improve this ability via the identification of a thin fibrous cap and coupled with increased plaque macrophage infiltration.

Culprit plaque that have ruptured demonstrate several different pathological characteristics. It is suggested that around 80% of ruptures leading to clinical conditions originate from the thin-capped fribroatheroma[68,79] (Figure 1-8 (C)). These are characterised by a large lipid core and a thin fibrous cap which has been infiltrated by inflammatory cells such as macrophages[68]. A further 10% of plaques associated with clinical events are suggested to be ones with calcium nodules (Figure 1-8 (B)) and approximately 20% are ones which cannot be classified as either[68]. OCT does not have the depth penetration necessary to visualise the whole lipid core of a plaque however it has the ability to accurately measure fibrous cap thickness as is demonstrated in Figure 1-8 (C), calcium nodules as demonstrated in Figure 1-8 (A) and also has the potential to detect macrophages (20-30µm) which have infiltrated the fibrous cap (as will be discussed in the next section)[57].

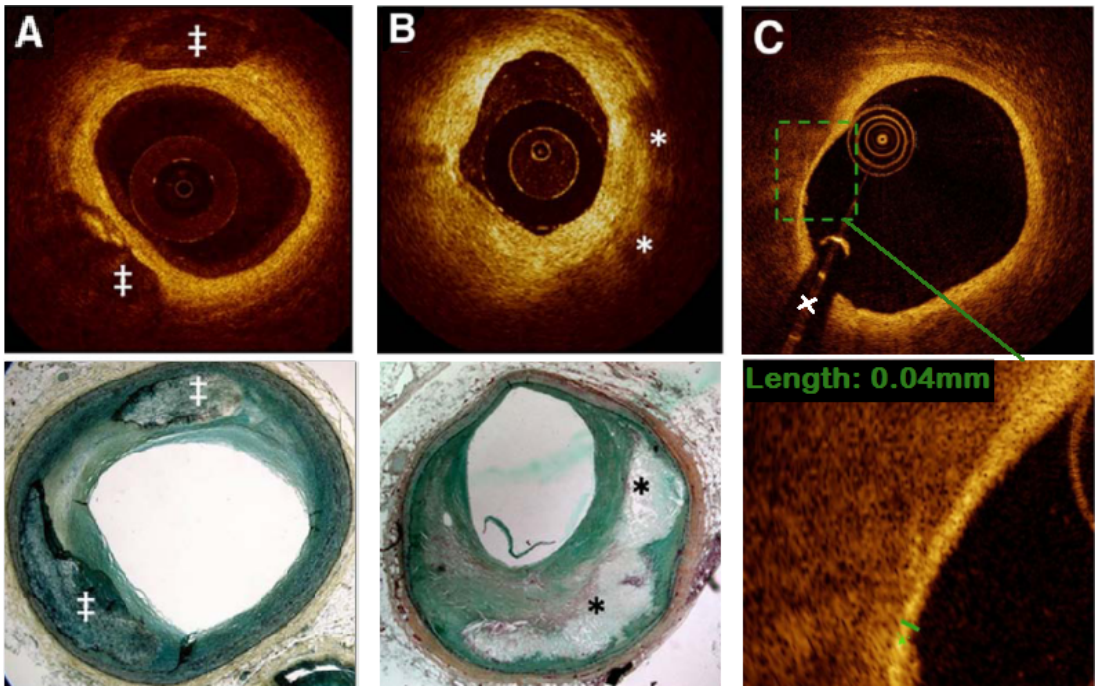

*Figure 1-8: OCT scans (top) of different plaque morphologies and their associated histology image (bottom). **A** is a mostly calcified plaque with the calcified regions marked with +, these have clearly defined borders with low signal and attenuation which permits deeper light penetration. **B** is a lipid-rich plaque with a thick fibrous cap (over 200µm) whereas **C** is a lipid-rich plaque with a much thinner cap (40µm) as is demonstrated on the close up in the bottom panel. The lipid core in these lipid-rich plaque has a diffuse border as compared with calcified regions and high light attenuation which minimizes tissue penetration. * indicates the lipid core, **x** marks a guide wire artefact. Images reused with permission (license num 4961361002169) from ([68]), Copyright Elsevier.*

1.3.2 Detecting macrophages in the fibrous cap

Intra-vascular OCT (IV-OCT) systems have been used extensively in ex-vivo and in-vivo studies of atherosclerotic tissue structure both in animal models[80–83] and humans[56,74,84–88]. This technique provides the gold standard assessment of coronary plaque cap thickness[57]. However, until relatively recently its ability to detect macrophages within the fibrous cap had not been confirmed[57]. The rationale for macrophage detection on OCT is based upon the large size of macrophages/foam cells (20-30µm) and their granularity (due to the presence of many lipid-rich phagolysosomes) which should in principle produce higher variability in OCT signal than the surrounding tissue[57].

A study in 2003 by Tearney *et al.* comparing histology and OCT data from ex-vivo coronary artery samples, showed not only that macrophages could be visualised on OCT images (Figure 1-9) but that they could be quantified using the normalised standard deviation (NSD) of local pixel intensities of the images[89]. The standard deviation basically gives a measure of variation in brightness of pixels on an image; if there are very bright pixels and very dark pixels within a region of interest (ROI), the SD of that ROI will be high whereas if the pixels are relatively uniform in intensity (all a similar brightness) the SD will be much lower. The theory here is that when macrophages are present in plaque tissue, their scattering properties will produce a big variation in pixel intensities within a small area of an OCT image and will result in a high SD value for that ROI. Tearney *et al.* compared the NSD values of OCT images with percentage macrophage cover on histology images of the same plaque cap areas[89]. A cut-off value of CD68 stained macrophage cover was used to define caps with either “high macrophage infiltration” or “low macrophage infiltration” [89]. Then, it was demonstrated that by using an appropriate threshold for NSD and a specific ROI, OCT could distinguish the high and low macrophage infiltration plaques with 100% specificity and sensitivity[89]. The areas of high macrophage burden can be clearly seen to co-localise on OCT and histological images taken (Figure 1-9) [89]. However, a point to note is that this study was performed in atherosclerotic samples taken from randomly selected cadavers[89] and therefore, no association between cap macrophage burden and clinical status could be made. Additionally, the authors used a bench-top OCT system with higher axial (10µm) and lateral (25µm)[89] resolutions than clinical systems, and their analysis was performed on the raw OCT data rather than the images that clinicians routinely interact with.

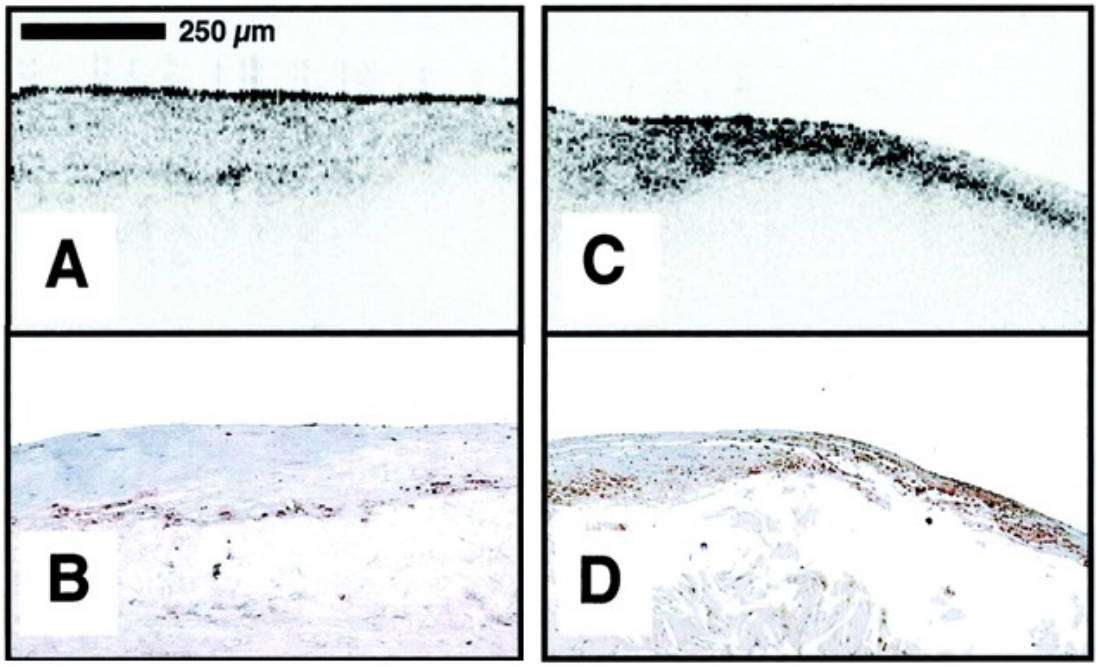

*Figure 1-9: OCT and associated histology images of human atherosclerotic plaques. **A** (OCT image) and **B** (histology image) show the same plaque, which has low macrophage infiltration in the fibrous cap whereas **C** (OCT image) and **D** (histology image) show a plaque with high macrophage infiltration in the cap. In the histology images the macrophages are apparent as dots because they have been stained with a CD68 specific marker. Images reused with permission (rightslink license num 4961361272178) from ([89]), copyright Wolters Kluwer Health, Inc.*

Since then, numerous studies have specifically investigated plaque macrophage detection with IV-OCT in-vivo and in excised tissue[88,90–92]. In particular, MacNeill *et al.*, used the same macrophage quantification method on IV-OCT images to relate cap macrophage burden in patients presenting with different severities of coronary artery syndrome[92]. It was found that patients with unstable disease (MI and unstable angina) had significantly more macrophage cap infiltration (higher NSD) than those with stable angina[92]. Additionally, ruptured plaques had a greater macrophage density (higher NSD) compared to non-ruptured ones and in the case of culprit lesions (plaques responsible for disease) macrophage burden (NSD) in the surface of the fibrous cap was a stronger indicator of disease severity than macrophage presence deeper inside the cap. The same was not true for remote non-culprit lesions[92]. Moreover, an NSD colour map technique (shown in Figure 1-10) was presented in this study as an attractive method for visualising supposed macrophage density [92].

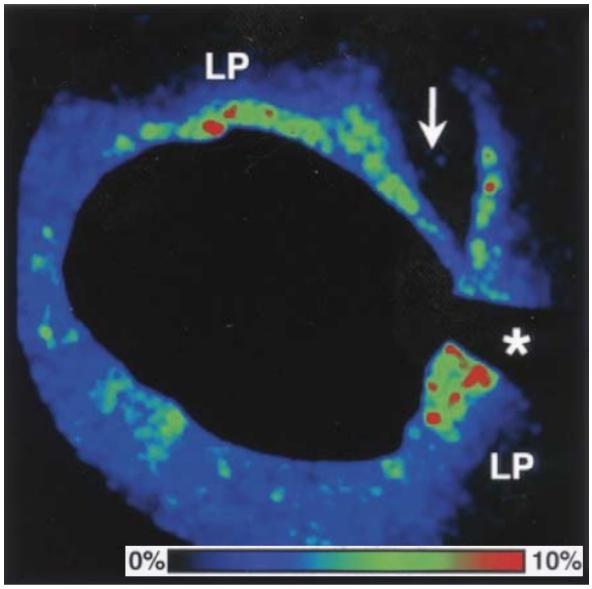

*Figure 1-10: OCT image of a coronary artery with a lipid-rich plaque (LP) and site of rupture (arrow). The colours represent the normalised standard deviation (NSD) of the OCT signal, showing macrophage density from blue (low) to red (high). The * indicates a guide wire artefact and the colour bar shows the NSD scale, with percentage of macrophage cover. Reused with permission (rightslink license num 4961370273831) from ([92]), Copyright Elsevier.*

A limitation to the results of these studies is that although the NSD parameter is easy to understand, it is not the same as macrophage density, indeed in the absence of macrophages the NSD will not be zero, due to base-line scattering[57]. Moreover, different components, other than macrophages may also cause high NSD values such as cholesterol crystals and some calcifications, it cannot therefore be considered a specific marker of plaque inflammation[57]. It is clear from these limitations that a more specific way of detecting macrophages on IV-OCT would provide a major advance, potentially improving the accuracy of this technique and its widespread clinical adoption. Additionally, although comparisons with histology analyses were made in some studies, the association between OCT image SD values and macrophage burden has not been thoroughly interrogated in a controlled in-vitro setting. To date, only de Schellenberger *et al.* [93] attempted to image macrophages in-vitro with an IV-OCT system and although their results were positive, there were several limitations to the study which will be discussed in the following section. A robust proof of concept study would therefore be needed to confirm the validity of the OCT SD as a metric for macrophage burden. These are the incentives behind this thesis project as will be presented in the Aims & Hypotheses section.

Although the studies mentioned here have made big steps towards imaging and quantifying infiltrating macrophages in atherosclerotic plaques with OCT they are based solely on the concept that macrophages inherently have different light scattering properties to the tissue surrounding them. However, there are many variables in this system whereby other particulates could result in a signal similar to macrophage infiltration. To address this, Ultrasmall superparamagnetic iron oxides (USPIOs) are presented in the following section as an agent capable of tagging macrophages and enhancing their detectability on OCT.

1.4 USPIOs FOR MACROPHAGE DETECTION

Ultrasmall superparamagnetic iron oxides (USPIOs) are particles characterised by their iron oxide core (usually less than 10nm), their large magnetic moment in the presence of an external magnetic field and their small overall size of less than 50nm (including the coating)[94]. Due to their small size and hydrophilic coating, USPIOs avoid the initial rapid phagocytosis by macrophages of the reticuloendothelial system and therefore have a longer blood pool circulation time (between 24-36h) compared to the larger SPIOs (>50nm)[94–97]. This makes USPIOs particularly adept at accumulating in inflamed tissues thanks to transendothelial leak and uptake by macrophages[95,97]. They have indeed been found to accumulate in macrophages observed within atherosclerotic plaque of hyperlipidaemic rabbits[98–101], ApoE$^{-/-}$ mice[102–104] and humans[105–107]. USPIO's have now been used extensively in clinical in-vivo MRI studies as markers for inflammation in multiple diseases[107–111]. In-vitro, various USPIOs have been shown to be non-toxic to the murine RAW264.7 macrophage cell line and human monocytes after exposure for 24h[112–114].

Ferumoxytol is the USPIO solution exclusively used in this thesis. It is composed of a 5nm magnetite core (Fe_3O_4) in a thick carboxymethylated low molecular weight dextran coat, giving it a total hydrodynamic size of between 17-31nm[115–117]. This particle solution was FDA approved for clinical use in iron-deficient patients with chronic kidney disease in 2009[117]. Since then, it has been used extensively in the clinic as an MRI contrast agent thanks to its magnetic properties and low toxicity compared to gadolinium[118]. In-vitro, Ferumoxytol is readily taken-up by RAW cells and has not been found to be significantly cytotoxic[93]. Multiple studies have reported that the simple incubation of RAW cells with Ferumoxytol at Fe concentrations of 0.05 to 0.5 mg/ml for 24h led to significant particle uptake by the cells[93,99]. As with all iron oxide nanoparticles (IONPs), Ferumoxytol concentration can be accurately quantified by ICP-MS and ICP-OES, however the colorimetric "Ferrozine" assay developed by

Fish W.[119] is often used as a faster and more cost effective alternative[120]. This assay has indeed become a popular method for in-vitro quantification of IONPs[121–124] and has been used by Müller *et al.* for precise quantification of USPIOs taken up by RAW cells[96].

The mechanism by which Ferumoxytol is taken up by macrophages has not been extensively researched. However, studies of this kind have been conducted using its predecessor, Ferumoxtran-10, which has the same core composition and overall size but differs solely by the coating: dextran rather than carboxymethylated dextran[96,125]. Müller *et al.* found the uptake of Ferumoxtran-10 by human monocyte derived macrophages (HMMs) to be non-saturable (with up to 10mg/ml incubation) and enhanced by incubation with transfection agent PLL but not by that with serum proteinases, suggesting non-specific fluid-phase transport as the mode of uptake[96,97]. This study also showed that incubation at concentrations of up to 1mg/ml for 72h was not toxic to HMMs nor did it cause them to activate, release pro-inflammatory cytokines or affect Fc-mediated phagocytosis[96].

The wealth of evidence showing USPIOs accumulate in atherosclerotic plaque macrophages and are non-toxic make them an excellent imaging target. Given their inherent metallic properties, it can be postulated that USPIOs may influence the backscattered OCT signal when imaged. To date, only one study has investigated the OCT properties of USPIOs; Ariza de Schellenberger et al.[93] imaged pellets of RAW cells loaded with Ferumoxytol and found their OCT signal was significantly changed compared to that of untreated macrophages[93]. There were several limitations to this study: packed cell pellets do not closely reflect the distribution of macrophages in human coronary plaques, the phantom set-up introduced several unnecessary optical boundaries, and no repeats of the experiment were performed. However, the positive results of the study highlight the high potential of USPIO as an OCT contrast agent and the need for further investigation both in-vitro and in-vivo.

1.5 Other OCT contrast agents

The field of IV-OCT contrast agents is very small, so far only a handful of studies have been published presenting new agents capable of being detected at the operating wavelength of IV-OCT systems, 1300nm. In particular, gold nanoparticles in different forms have been shown to be detectable with IV-OCT. These include plasmon-resonant gold nanorods[126], branched gold naonparticles[127], gold nanocages[128] and silica-coated gold nanoshells[129]. The reason there has been a focus on gold nanostructures is that their surface plasmon resonance

can be tuned by modifying their geometry to increase backscattering or absorption at the IV-OCT wavelength: 1300nm[129]. The most successful of these thus far seems to be the silica-coated gold nanoshells presented by Hu *et al.* [129,130]. The only other contrast agents shown to be detectable on IV-OCT are quantum dots: a semiconducting nanoscale crystal [130]. These quantum dots are capable of emitting light when excited which therefore makes them an ideal target for dual modality imaging[130].

Importantly, none of these studies investigated the biocompatibility or uptake of their contrast agents by cells. And although the experimental setups varied between the studies, with some imaging the particles injected into excised tissues, none actually investigated the IV-OCT properties of the contrast agents when loaded into cells. Additionally, the OCT "contrast enhancement" was evaluated either by eye or with image analysis metrics based on signal attenuation, both of which are significantly affected by many components of atherosclerotic plaques. These limitations and the small size of the field demonstrate a clear need for further investigation into the IV-OCT contrast properties of nanoparticles with an emphasis on real-world application.

1.6 Aims & Hypotheses

The introduction to this thesis provides an overview of both coronary artery disease and OCT and how the latter can be used to help research, diagnose and treat the former. OCT is now a routine clinical care instrument for many diseases including coronary artery disease (CAD). Its ability to detect a thin fibrous cap, assess plaque integrity and accurately quantify the severity of luminal stenoses already makes it a useful clinical technique. If OCT could also reliably and accurately detect plaque macrophage infiltration then it might provide the gold standard technique for vulnerable plaque detection and thereby improve patient care and outcomes.

In light of this, the aims of my research have been to establish methods for the enhanced detection and quantification of macrophages with the clinical IV-OCT system in-vitro, ex-vivo and in-vivo. The overarching hypothesis has been that macrophages can be detected and quantified on IV-OCT images using the standard deviation of pixel intensity metric and that this detection can be enhanced and made more specific by labelling with metallic particles, specifically USPIOs and novel lanthanide-based nanoparticles. This thesis aims to investigate

this model in vitro, in animal models and finally in humans presenting with symptomatic coronary artery disease.

Chapter three of this thesis presents an **in-vitro** OCT study whose **aim** is the detection of macrophages labelled with USPIOs in a bespoke phantom artery model (described in Chapter two). The overarching **hypothesis** of Chapter three is that intra-cellular USPIOs will enhance the detection of macrophages on IV-OCT images in-vitro.

In **Chapter four**, the same USPIO particles are used in an $ApoE^{-/-}$ **mouse study** with the **aim** of enhancing the OCT detection of macrophages in excised atherosclerotic tissue. The main **hypothesis** of chapter four is that the plaques of USPIO treated mice will have a higher signal on IV-OCT images compared to untreated mice.

Chapter five presents an in-vivo **human study** with the **aim** of enhancing the OCT detection of inflammation (using USPIO) in the caps of culprit atherosclerotic plaques of patients presenting with acute coronary syndrome. The overarching **hypothesis** of chapter five is that culprit plaques of USPIO treated patients will yield higher OCT signal compared to saline treated patient culprit plaques and compared to non-culprit plaques.

Finally, the main **aims** of **Chapter six** are to introduce a panel of novel lanthanide based nanoparticles designed to enhance OCT contrast. The main **hypothesis** of chapter six is that a novel lanthanide based particle will significantly enhance the OCT detection of macrophages in-vitro.

2 CHAPTER TWO: MATERIALS & METHODS

2.1 CELL CULTURE

The mouse macrophage-like cell line RAW264.7 was cultured in either T-75 or T-162 tissue culture flasks kept in the tissue culture incubator at 37°C. The RAW cell line was initially thawed from a stock kept in the -80°C freezer by Dr Marc Vendrell (originally bought from ATCC) and all the tissue culture was performed under sterile conditions using a laminar flow hood in the tissue culture room in the Centre for Inflammation Research (CIR) at the QMRI.

The cells were cultured in RPMI media 1640 supplemented with 10% FBS (foetal bovine serum), 1% pen/strep (penicillin/streptomycin) and 1% L-glutamine, all supplied from Gibco®. 15 ml of media was used in T75 flasks and 30 ml in T162 flasks. The culture flask was checked every 2 to 3 days under the microscope and when the cells were fully confluent (approximately every 3 days) they were lifted by scraping with a plastic scraper and 10% of the culture was transferred to a new flask containing fresh warm media. Every so often, if many detached cells could be observed in the flask under the microscope, they were washed out with DPBS by Gibco® before the attached cells were lifted.

2.2 OCT IMAGING

All human coronary artery OCT images taken during the clinical trial presented in Chapter 5 were acquired using the Terumo Lunawave™ system with the Fastview™ imaging catheter (Terumo international Systems). This system was on loan at the Royal Infirmary of Edinburgh Catheterisation Lab and unfortunately had to be returned during the course of this thesis project. The Ilumien Optis™ frequency domain OCT system (LightLab/St. Jude Medical, St. Paul, MN) was acquired to replace it and it was used in conjunction with the Dragonfly™ imaging catheter (LightLab/St. Jude Medical, St. Paul, MN) to take the OCT images of phantoms (presented in Chapters 3) and murine aortas (presented in Chapter 4).

Both OCT systems work in the same way: the 1mm catheter is introduced to the area of interest then the OCT controls are handled on the connected computer. First, the OCT image gets automatically calibrated, then a pullback scan is performed, whereby the OCT light source automatically gets pulled backwards through the transparent plastic tube of the catheter by the OCT machine mechanics. This enables the system to create multiple sequential circular cross-sectional OCT images throughout the entire length of the pullback scan. This results in a “stack” of logarithmic scale compressed images which are sequential slices through the tissue or phantom and are exported in .tiff format. The images from the

Terumo Lunawave™ system are 600x600 pixels in dimension and those from the Ilumien Optis™ system are 1024x1024 pixels. Both are grayscale images but the Ilumien Optis™ ones have an orange colour map filter on top which can be removed – it is mostly but not always present in the images shown in this thesis. The specifics of imaging methodology and image analysis for each system (phantom, mouse and human) are covered in the following chapters.

2.3 PHANTOM MOULD DESIGN AND OPTIMISATION

Initially, phantoms were made with agar in petri dishes, using tubing to create a cavity in which the OCT catheter could be placed (Figure 2-1 (A)). However, these were not useful for testing multiple conditions within one phantom, therefore segmented phantoms were developed. At first, they were made with readily available equipment (petri dishes, falcon tubes, blue tack, plastic sheets and plastic tubing) but these proved time consuming to make repeatedly and impractical to use.

Consequently, a 3D printed mould was designed using Autodesk Inventor Professional, the design is shown on Figure 2-1 (B) and the printed mould with tube insert is pictured on Figure 2-1 (C). This model was much more practical to use but nevertheless still had some flaws. Specifically, the differing sizes of the sections rendered gel making more complex, especially when these needed to be loaded with cells. For these reasons, new designs of segmented moulds were subsequently created (pictured in Figure 2-1 (D,E)) and 3D printed (pictured in Figure 2-1 (F,G)). These two models have 5 identical sections partitioned by plastic separations which are pierced by a hole measuring either 3 mm or 1 mm in diameter (panels (D) and (E) respectively) in which metal rods of those diameters can be placed to create an artery like cavity (panels (F) and (G) respectively). The phantom sections were designed to measure 0.5 cm^3 when the rod is in place, and therefore hold exactly 0.5 ml of liquid or agarose gel. These moulds vastly improved ease and efficiency of creating agarose phantoms for IV-OCT imaging.

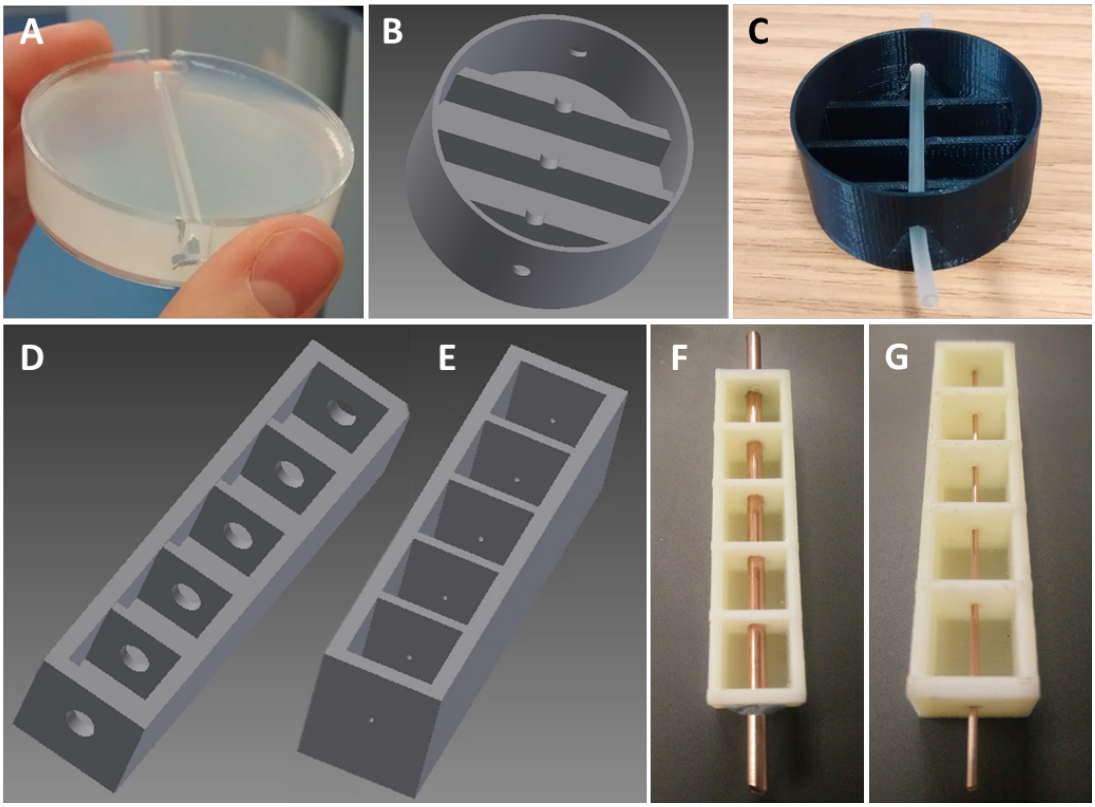

Figure 2-1: Development of a 3D printed phantom artery model. (A) Early prototype of an artery-like cavity moulded using agar in a petri dish with a plastic tube. (B) First 3D segmented phantom mould design on Autodesk Inventor Professional. C) 3D printed mould from design B with plastic tube insert. (D) and (E) two new 3D segmented phantom mould designs on Autodesk Inventor Professional differing by the size of the perforation: 3 mm (D) and 1 mm (E) in diameter. (F) and (G) 3D printed moulds from designs D and E respectively with metal rod inserts.

Multiple phantom moulds were 3D printed at the School of Engineering in order to make several phantoms simultaneously. Optimisation with the previous phantom iterations identified agarose at 1.5 % as the best substrate for OCT imaging over agar. Phantoms in this thesis were therefore made with 50 ml of PBS and 0.75 g of agarose powder (Sigma-Aldrich) heated in the microwave for a few minutes (with regular stirring) until completely melted and no particulate matter could be seen by eye. 0.5 ml of the melted agarose was then pipetted into each phantom mould section and depending on the experiment, initially mixed with either particles or pellets of fixed RAW macrophages (detailed subsequently). Once the agarose gels are set, the metal rod is removed and the phantom is imaged using the commercially available Ilumien Optis™ frequency domain OCT system connected to the Dragonfly™ imaging catheter (LightLab/St. Jude Medical, St. Paul, MN) which is inserted into the artery-like cavity. The OCT catheter is approximately 1 mm in diameter and therefore fits

snugly in the 1 mm diameter cavity phantom (Figure 2-1 (E,G)) enabling direct imaging of the gels without an air interface for the light to travel through. Conversely, the 3 mm cavity phantom (Figure 2-1 (D,F)) does not allow for the catheter to be fixed in place which means it's position often changes along the length of the phantom.

OCT slices of the 3 mm (large) and 1 mm (small) diameter cavity phantoms are shown side by side on Figure 2-2. The plain agarose gel images (A, B) are markedly different, with (B) showing much more homogeneity and better depth penetration of the signal compared to (A). Indeed, the air interface in the large cavity phantom induces a loss of signal at a depth of about 2 mm whereas the small cavity phantom shows no loss of signal, even at the maximal depth of 3.5 mm. Additionally, the position of the catheter in (A) affects which areas of the image are brightest whereas in (B), the catheter is in a fixed position in the phantom so the gel imaging appears much more even. These effects are also apparent when imaging agarose gels mixed with $20x10^6$ fixed RAW cells (E, F). Indeed, the loss of OCT signal occurs at a depth of around 1.5 mm in the large cavity phantom (E) and at 2 mm in the small cavity phantom (F). Therefore in the large cavity phantom, the depth of imaging varies between 1 mm (where the catheter touches the gel) and 0.25 mm (where the catheter is furthest away from the gel). Conversely, the small cavity phantom enables even 1.5 mm depth imaging of the cell gel all the way around the catheter (as can be seen in (F)). Consequently the 1 mm diameter cavity phantom mould (Figure 2-1 (G)) was selected for use in all subsequent phantoms in this thesis to ensure best reproducibility as well as ease of ROI drawing. Panels (C) and (D) of Figure 2-2 show OCT images through the plastic separations in between the chambers of the phantom moulds – these look very different to agarose under OCT and enable clear distinction between sections containing different gel conditions.

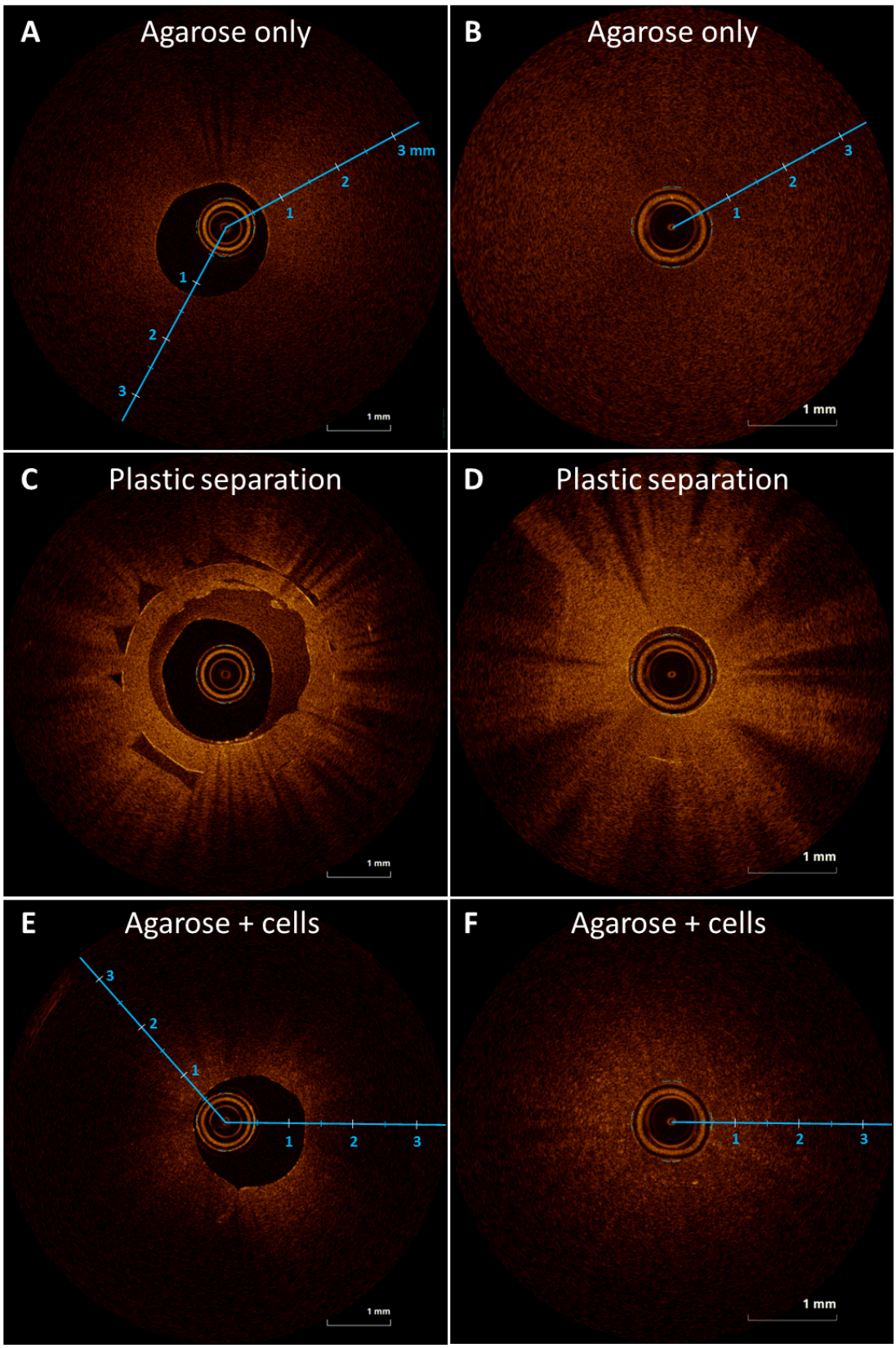

Figure 2-2: Comparison of OCT images from 3 mm (left) and 1 mm (right) diameter cavity phantoms. (A) and (B): 1.5 % agarose gel only. (C) and (D): plastic separation between the gel compartments. (E) and (F): 1.5 % agarose mixed with $20x10^6$ fixed RAW cells.

2.4 OCT IMAGE ANALYSIS AND PROCESSING

2.4.1 Regions of interest

The same method for OCT image analysis was applied across all the in vitro, mouse and clinical studies. Regions of interest (ROIs) were drawn on individual slices from the OCT stacks using a software called Analyze™ in order to avoid common artefacts such as dark bands, bright spots, stitching artefacts, signal drop off areas and guidewire artefacts as exemplified in Figure 2-3.

For the in-vitro phantoms, between 1 and 4 ROIs of an average of 10000px were drawn on most slices of the imaging stacks (with 3 being most common), depending on the number of artefacts present (Figure 2-3 (A)). There are approximately 70 OCT image slices in every section of the phantom and therefore approximately 200 ROIs were drawn in each.

For the mice, between 1 and 4 ROIs of an average of 700 pixels in size were drawn on each slice of the aorta imaging stacks (with 2 being most common), depending on the shape of the plaque and arterial wall as well as the artefacts present. There are approximately 88 OCT image slices in every aorta imaging stack. Approximately 175 ROIs were drawn for each mouse aorta, with an equal split drawn in the plaque containing images and the non-plaque control images. On the OCT slices of the plaque-containing section of aorta (in the aortic arch), the ROIs were drawn on the bright outer edge of the plaque (the cap) as exemplified in red on Figure 2-3 (B). ROIs were also drawn on each OCT slice of the descending aorta which did not contain plaque, to be used as a control – they were drawn on the outer edge of the tissue as exemplified in green on Figure 2-3 (B).

For the patient images, ROI drawing was performed by cardiologist Dr Simon Wilson. For each plaque, 3 ROIs were drawn on 8 different OCT slices (equally distributed through the plaque). As shown in Figure 2-3 (C), one ROI was drawn in the middle of the plaque cap (green) and one ROI on each shoulder of the plaque (red). These ROIs were drawn small (average of 530px) to avoid drawing over non-cap tissue, dark bands and guidewire artefacts.

For both mouse and human images, ROI drawing was done blinded to the treatment information and clinical data. All ROIs were saved as .obj files for use in the Matlab processing described in the following section.

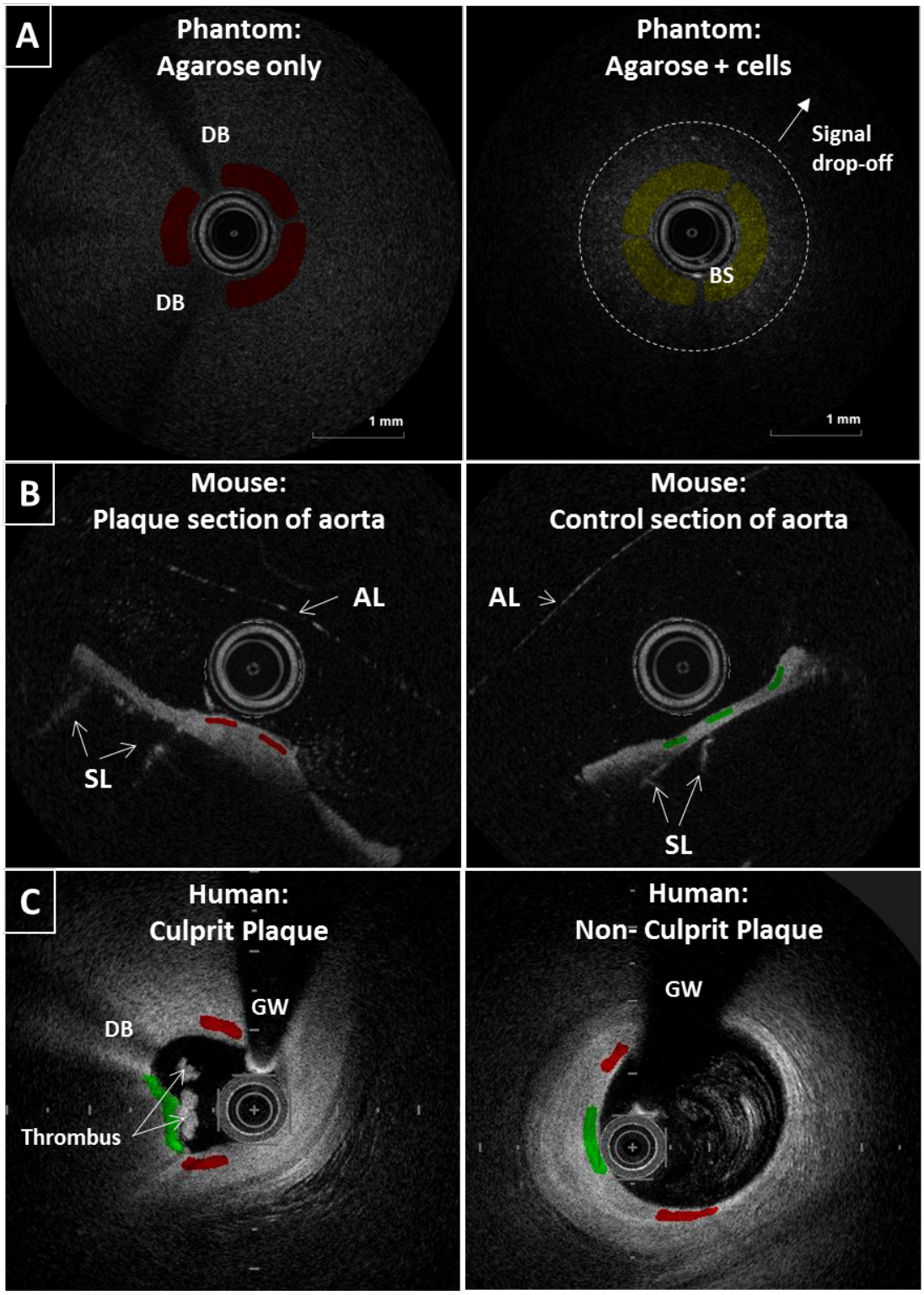

Figure 2-3: OCT image artefacts and ROI drawing method for all three systems, phantoms (A), mice (B) and humans (C). Artefacts visible on these images include dark bands (DB), bright spots (BS), the air-liquid (AL) interface line, bright lines created by imperfections in the Silguard (SL) gel that the mouse aortas are pinned onto and the guidewire (GW) shadow on the human images. ROIs are shown here in green, yellow and red.

2.4.2 Automated quantification of ROI metrics

Custom software was developed using Matlab (Mathworks, Inc) to process the pixel information within ROIs of OCT images. This software was used to calculate a number of different metrics (ROI size, ROI mean pixel intensity, min and max pixel intensity, standard deviation and variance of mean pixel intensity, etc…). The standard deviation of the mean pixel intensity (SD) is the most important of these metrics for the ensuing analysis, it represents the variation in the light scattering properties in the tissue. Indeed, if the tissue is very granular, with many cells, or reflective particles, the SD should be higher. This SD value has been used in other OCT studies, such as that of Tearney *et al.* [89], and formed the basis for our analysis approach to quantifying the burden of macrophages and/or nanoparticles in this thesis. Specifically the SD was calculated using the following formula where N is the number of pixels in the ROI, S(x,y) is the pixel intensity as a function of x and y locations within the ROI and $\bar{S}$ the average pixel intensity within the ROI:

$$\sigma = \sqrt{(\frac{1}{N} - 1) \times \sum_{ROIwidth} \times \sum_{ROI\ heigth} \times (S(x,y) - \bar{S})^2}$$

In the study by Tearney *et al.* [89], they used the raw OCT images for their analysis and therefore performed a normalisation (to the images min and max) step, thus naming their metric the Normalised Standard Deviation (NSD). Subsequent to this, a background removal and median filtering step was also implemented. However, the image analysis for this whole thesis is based on pre-processed images from clinical IV-OCT systems. The images from these systems have already gone through normalisation, background removal and filtering steps in order to achieve clear images for clinicians to interpret. Therefore, in our image analysis software we did not implement normalisation, background removal and filtering steps as this would remove important information from the image and negatively impact the detection of macrophages with the SD metric.

Two versions of the Matlab code for this ROI metric processing were written, one for OCT images from the Terumo Lunawave™ system (human clinical trial data) and the second for those from the Ilumien Optis™ system (in-vitro phantoms and ex-vivo mouse data). This is because the images from each machine have different sizes and different numbers of total pixels. In addition, the Terumo Lunawave™ images are saved with burnt-in tick marks (see Figure 2-4) which required removal from the image analysis for easier ROI drawing on the clinical images. This is implemented in the Terumo Lunawave™ version of the code using a

mask, as presented in Figure 2-4. Both versions of the Matlab code are shown in full in Appendix 1 and Appendix 2, they were written by Dr Calum Gray and edited/adapted by myself.

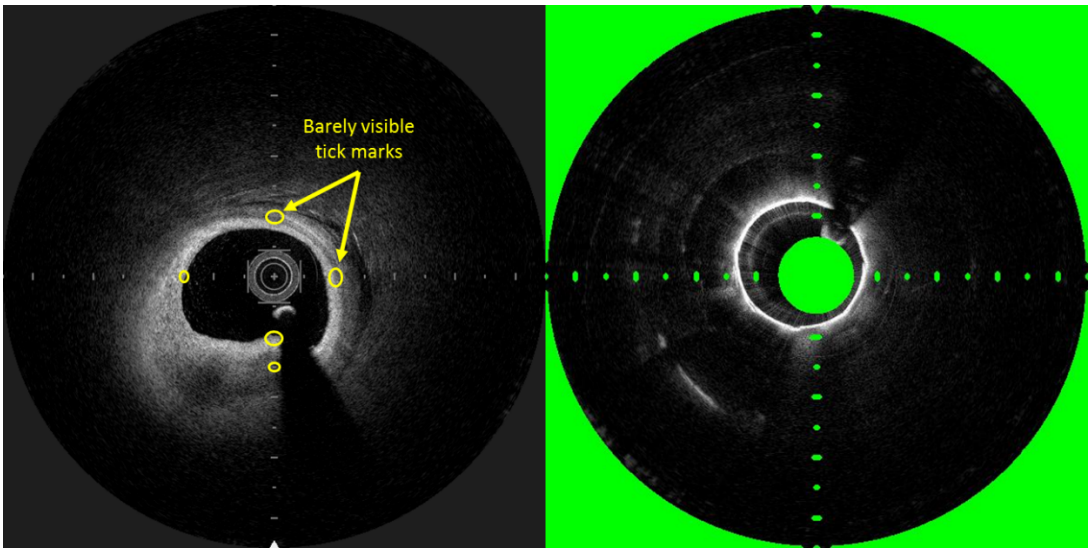

Figure 2-4: Left – OCT image slice in the coronary artery of a patient taken with the Terumo Lunawave™ system. The images have burnt-in tick marks, some of which are barely visible against the tissue, and therefore time consuming to avoid when drawing ROIs. Right – mask created to enable the removal of tick marks and catheter at the image processing step.

2.4.3 Automated production of SD hotspot maps

In order to visualise the local differences in standard deviation of pixel intensity on the OCT images, another piece of Matlab code (Appendix 3) was developed to produce a SD hotspot map overlay. It was written by Dr Calum Gray and subsequently edited with help from Dr Pierre Bagnaninchi. The code processes the image in the following way: each individual pixel is assigned a colour based on the value of the SD of pixel intensity in a square kernel (of a predetermined size) surrounding the pixel. In this way, all pixels are assigned a colour which gives a scale of the SD in the local region – showing the extent of the variation in the OCT signal. The size of the square kernel affects the appearance of the resulting colour map greatly so detailed optimisation was performed to find the optimal kernel size. For the Ilumien Optis™ images (phantoms and mouse aortas) the kernel was selected to be 5x5 pixels in size. The kernel size was scaled to 9x9 pixels for the Terumo Lunawave™ images based on the total pixel numbers in the images from each system (1024x1024 for Optis™ and 600x600 for Lunawave™). This colour mapping was restricted to ROIs drawn on select OCT

images for each condition, an example for a cell phantom and a human culprit plaque are shown at the top of Figure 2-5.

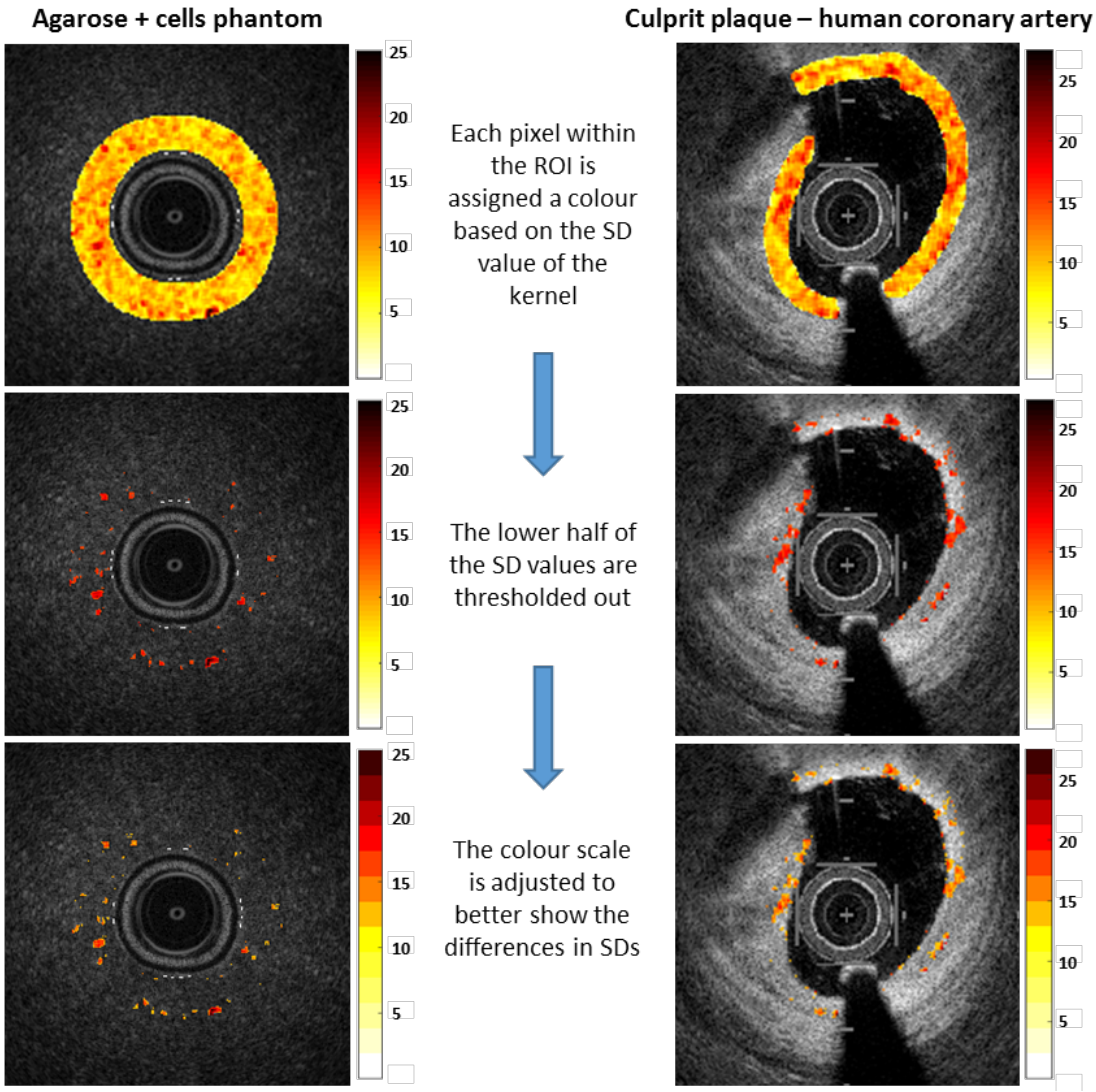

Figure 2-5: Standard deviation (SD) hotspot map optimisation. Top: each individual pixel in the ROI is assigned a colour based on the value of the SD of pixel intensity in a square kernel (of a predetermined size) surrounding the pixel. The colour scale shows white/yellow to be low SD values and dark red high SDs. Middle: the lower half of the SD values are removed in order to leave cleaner, easier to see "hotspots". Bottom: the number of colours on the scale are reduced so that variation in SD value is easier to see.

For better visualisation of the SD "hotspots", a threshold was set to half of the maximal SD value (second step in Figure 2-5). In this way, all pixels whose SD values are below half of the highest SD are not included in the colour map. This makes the image less overwhelming to look at and shows just the highest SD values overlaid on the original image. The colour scheme and scale also had to be optimised and integrated into the code in order to better

distinguish SD values. The third step in Figure 2-5 shows how setting the colour scale to have just 13 colours as opposed to the standard 64 makes the different values much easier to see on the images. A few OCT images from each condition for each of the 3 systems (in-vitro, ex-vivo mouse and in-vivo human) were processed with this code and the resulting SD hotspot images were saved as .tif files. Representative examples of these are presented in Chapters 3, 4 and 5.

2.5 STATISTICAL ANALYSIS

Statistical analysis was performed using the Graphpad Prism software, version 5. For all datasets with more than two columns to compare, significant difference was tested using a one-way ANOVA with the Tukey post-test to compare all pairs of treatments. For all datasets with only two columns to compare, significant difference was tested using a two-tailed unpaired t test.

3 CHAPTER THREE: IN VITRO PHANTOM USPIO-OCT STUDY

3.1 Introduction

Chapter 1 demonstrated the need for a method of tagging vulnerable plaque macrophages on IV-OCT and presented USPIO as an agent which could fill that need. This chapter aims to test this hypothesis in an in-vitro setting. Indeed, in section 1.1.5 it was established that there has been a keen interest over the last 30 years in detecting "the vulnerable plaque" and that OCT has important potential in that respect. Intra-vascular OCT (IV-OCT) is used routinely in the clinic during coronary interventions, has the ability to detect important plaque components (fibrous cap, lipid pool and microcalcifications) with preliminary data suggesting it might also detect areas of increased plaque macrophage density. This last point is of particular interest given the key role played by plaque macrophages in driving atherosclerotic disease progression and plaque rupture but requires improvement to become of clinical utility.

Previous attempts to quantify coronary macrophage density on OCT have used the local standard deviation (SD) of pixel intensity[89,90,92], yielding positive results with some limitations, as is discussed in detail in section 1.1.3. Notably, this metric has not been shown to be unequivocally specific to macrophages and has never yet been tested in-vitro or in animal models. This calls not only for a robust in-vitro proof of concept study but perhaps also for an attempt to enhance the OCT detection of macrophages using a probe or nanoparticle. As introduced in section 1.4, USPIO particles are an ideal candidate for this, given that they are approved for clinical use and have been shown to accumulate in human coronary plaque macrophages[105–107]. Moreover, their scattering properties, should in theory, produce higher OCT contrast as has been demonstrated in one in vitro study[93]. Ariza de Schellenberger et al. showed that when packaged into RAW cells, USPIOs do significantly increase the OCT contrast[93]. However, the N numbers were low, the SD metric was not tested, and the experimental phantom created did not accurately reflect in-vivo conditions.

There are therefore many incentives for further testing the OCT contrast properties of USPIOs and thus for the development of a new robust in vitro phantom model for coronary IV-OCT imaging. The following chapter is the in vitro stage of a 3-part translational study investigating the USPIO-enhanced detection of plaque macrophages on IV-OCT. The five aims and five associated hypotheses of this chapter are outlined below.

AIM 1 (section 3.3.1): To determine how effectively murine macrophage cultures uptake USPIOs.

Hypothesis 1: Murine macrophages will take up USPIOs from the media in a dose dependent manner during overnight incubation in normal cell culture conditions.

AIM 2 (sections 3.3.2 and 3.3.3): To test whether USPIOs alone enhance the OCT signal in our novel phantom model.

Hypothesis 2: USPIOs held homogenously in an agarose gel will yield higher OCT contrast compared to an agarose only gel.

AIM 3 (sections 3.3.2 and 3.3.4): To test whether macrophages alone enhance the OCT signal in the phantom model (using the standard deviation of pixel intensity as a metric).

Hypothesis 3: Macrophages held homogenously in an agarose gel will yield higher OCT contrast compared to agarose only.

AIM 4 (sections 3.3.2 and 3.3.4): To determine if USPIOs loaded into macrophages can further enhance the OCT signal.

Hypothesis 4: Macrophages loaded with USPIOs held homogenously in an agarose gel will yield higher OCT contrast compared to untreated macrophages in agarose.

AIM 5 (section 3.3.5): To test whether the SD hotspot overlay tool accurately visually represents the SD analysis results in the macrophage *phantom images.*

Hypothesis 5: There will be more, high intensity hotspots on the images of gels containing macrophages compared to the control gel. Additionally, there will be even more, high intensity hotspots on the images of gels with USPIO-loaded macrophages.

If successful, this in vitro investigation and image analysis methodology will pave the way for the use of USPIOs as a new OCT contrast agent in atherosclerosis in murine models (Chapter 4) and subsequently in humans (Chapter 5).

3.2 METHODS

3.2.1 Ferrozine assays

The RAW264.7 murine macrophage-like cell line was cultured as described in section 2.1. The USPIO used throughout this thesis was the Ferumoxytol (or Ferahaeme) solution by Rienso® and the concentrations hereafter specified refer to the concentrations of iron present in the compound (30mg/ml in the stock solution). RAW cells were incubated with 0.3, 1.5 and 3 mg/ml (equal to 5.37, 26.86 and 53.72 mM of Fe) of USPIO in media for 24 hours. Following washing in Dulbeco's PBS (Gibco), lifting by scraping and counting with a haemocytometer, $3x10^6$ cells were taken from each treatment condition. These were pelleted and then lysed in 300µl of 1% triton for 10 mins. The cell lysates were diluted 100 times (1µl of lysate + 99µl of distilled water) and repeats were made for each tube. Each was treated with 100µl of iron releasing reagent (equal parts 1.4M HCl solution and 4.5% $KMnO_4$ in H_20 – combined and incubated at 60°C for 2 hours in a fume hood (chlorine gas is produced during the reaction).

Iron standard solutions were made (300µL for each) using FeCl3 concentration between 0-300µM. To each were added 300µl of 50mM NaOH, 300µl of iron releasing agent and 90µl of iron detection reagent (6.5mM ferrozine, 6.5mM neocuproine, 2.5M ammonium acetate, and 1M ascorbic acid in water). These were incubated for 30mins before being transferred to a 96 well plate.

After their 2-hour heated incubation with the iron releasing reagent, the cell lysate samples were cooled to room temperature. 30µl of the iron detection reagent was then added to each and incubated for 30mins before transferring to the 96 well plate with the iron standard solutions. The full plate was run in a plate reader, measuring the absorbance at 550nm with 700nm for the background. The background values were subtracted from the 550nm absorbance values. An iron standard curve was plotted using the measured absorbance values of the iron-standard solutions against their known Fe concentrations. The equation of this curve was then used to convert the cell lysate absorbance values to Fe concentrations and plot these against the initial Fe treatment concentrations (Figure 3-1). This assay was repeated 4 times, on separate days with a different passage of RAW264.7 cells.

3.2.2 Phantoms

A bespoke phantom artery mould was designed and 3D printed, as described in detail in methods section 2.3, in order to easily and reproducibly image multiple agents of interest

(macrophages and/or particles) in one scan, using a clinical IV-OCT system. In brief, this mould has five identical square chambers of a volume of 0.5ml and each plastic partition has a central 1 mm diameter opening through which the IV-OCT catheter is introduced for imaging. Using this 3D printed mould two simple phantoms were made with 1.5% agarose in PBS and different amounts of USPIO solution (Ferumoxytol by Rienso® 30mg/ml) to obtain different concentrations of particles in each of the 5 phantom sections in the following way:

- No USPIO control: 0.5ml melted agarose alone
- 0.05 mg/ml USPIO: 1.7µl USPIO in 1ml melted agarose (0.5ml discarded)
- 0.25 mg/ml USPIO: 4.25µl USPIO in 0.5ml melted agarose
- 2.5 mg/ml USPIO: 42.5µl USPIO in 0.46ml melted agarose
- 5mg/ml USPIO: 85µl USPIO in 0.42ml melted agarose

These were mixed well to ensure homogenous distribution of the particles in the gel and they were each transferred to a section of the phantom mould described in section 2.3 to form the phantoms pictured in section 3.3.2.

Additionally, 7 macrophage laden phantoms were made. For this, the RAW264.7 murine macrophage cell line was cultured as described in section 2.1 in T162 flasks and incubated with 33µl, 167µl and 1.7ml USPIO solution in a total of 20ml of media (corresponding to 0.05, 0.25 and 2.5 mg/ml concentrations respectively) for 24 hours. Following washing in Dulbeco's PBS (Gibco), lifting by scraping and counting with a haemocytometer, $20x10^6$ cells were taken from each treatment condition. These were washed, pelleted and fixed in 1ml of 4% PFA for 15 minutes (to ensure the cell membrane remains intact and retains the intra-cellular particles) then pelleted again and the supernatant removed. These pellets were warmed up in a water bath then thoroughly mixed with 0.5ml of warm 1.5% agarose using a warmed pipette tip (to avoid setting prematurely) before transferring to the phantom mould.

All these phantoms were made with the 1mm rod insert in place to create a "lumen" through the agarose gel phantom. This rod was removed in order to insert the Dragonfly™ OPTIS™ OCT catheter and image the phantom using the St. Jude Medical OTPIS integrated system. Image analysis was performed using the custom methods and software described in section 2.4. Finally, the bespoke OCT SD hotspot tool described in section 2.4.3 was tested on sample images to render a visual representation of these OCT contrast differences.

3.3 RESULTS

3.3.1 Iron uptake quantification

To be certain that any OCT signal changes between untreated cells and USPIO treated cells are due to the presence of USPIOs inside the cells, a number of experiments were performed. Loading of mouse macrophage cultures with USPIOs was done by 24h incubation with varying concentrations of particles. These cultures retained iron colourations post-washing as can be seen in Figure 3-1 (A) suggesting the particles were effectively taken up by the cells during incubations. Microscopy observations of these cultures further confirmed this with very dark endosomes being visible in the cytoplasm of cells incubated with USPIOs at concentrations above 0.3mg/ml. The highest concentration tested (3mg/ml) yielded very clear differences with the untreated control as shown in Figure 3-1 (B).

To further confirm USPIO uptake by the murine macrophages and test its efficacy, Ferrozine assays were performed in order to quantify intra-cellular iron as described in methods section 3.2. In this assay, the acidic $KMnO_4$ solution is used on cell lysates to separate iron complexed with cellular proteins. Following this, a Ferrozine ($C_{20}H_{13}N_4NaO_6S_2$) solution is used to bind ferrous iron into a complex which absorbs light in the 550nm wavelength, enabling colorimetric quantitation of intracellular iron. These assays were completed following a 24h incubation of murine macrophages with 3 different concentrations of USPIOs (0.03, 0.3 and 3mg/ml), a media only control and using iron standard solutions as a reference. The results are presented as a plot of incubated iron concentrations against measured intra-cellular iron concentrations in Figure 3-1 (C). As expected, increasing the incubation concentrations of USPIOs leads to higher intra-cellular concentrations measured with the Ferrozine assay and these results were reproducible over 4 repeats (tight error bars). This increase however is not proportional - the curve's slope becomes less acute as the incubated concentrations increase and shows signs that it might plateau past the highest concentration tested (3mg/ml USPIO = 53.72 mM of Fe). This is again to be expected given that macrophages cannot keep taking up particles indefinitely and will eventually reach a maximal amount.

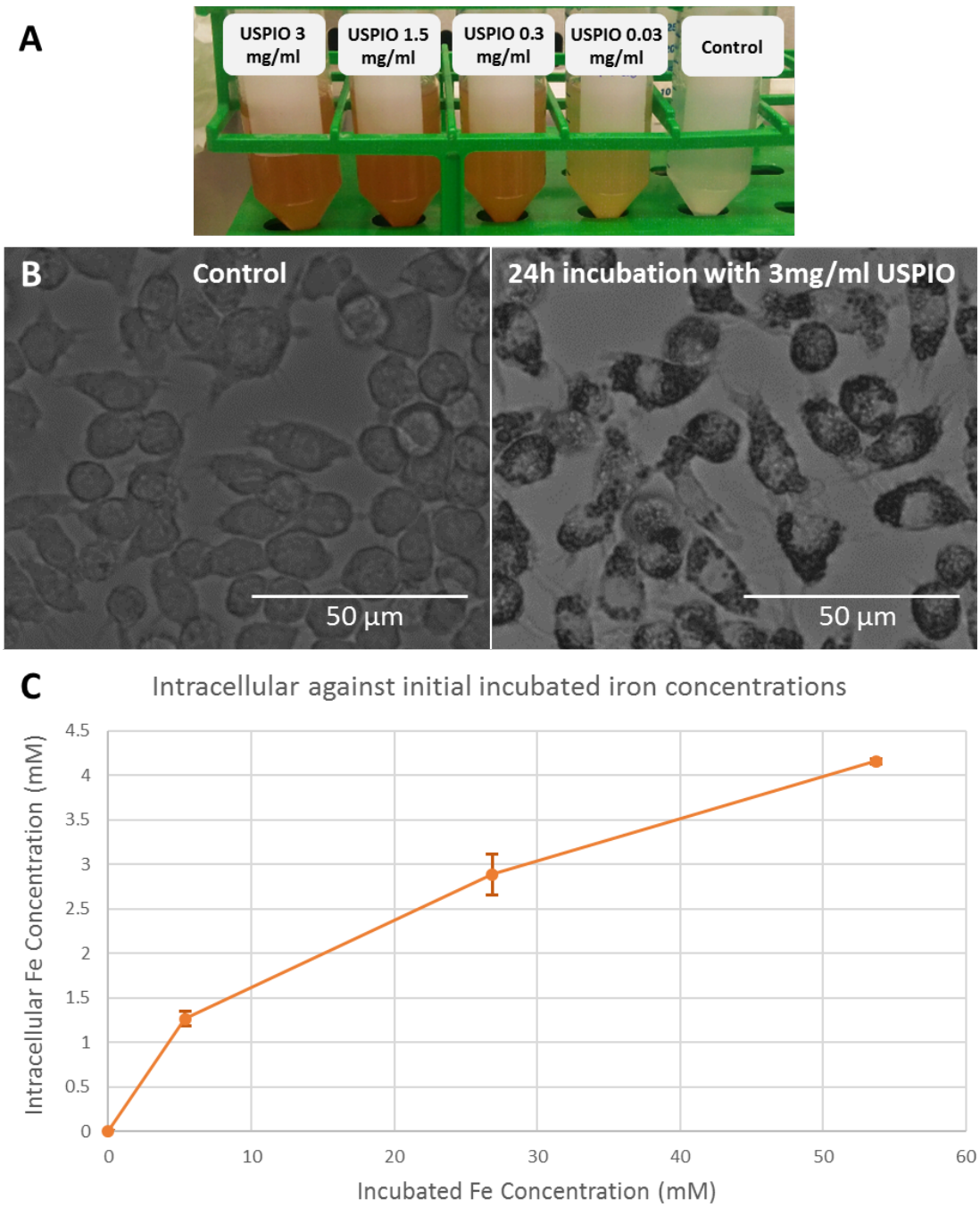

Figure 3-1: Iron uptake quantification assays. (A) Mouse macrophage suspensions after 24h incubation with varying concentrations of USPIOs and multiple washes – the iron colour is retained, indicating the remaining USPIOs are inside the cells. (B) Microscopy photos of these cells, the USPIOs are clearly visible in cellular endosomes when comparing to the control. (C) Ferrozine assay results plot showing the measured iron concentrations within the cells after incubation with USPIOs against the initial concentrations those cells were incubated with (n=4, error bars=SD).

3.3.2 Phantom OCT imaging

The 3D-printed phantom artery moulds described in methods section 2.3 were used to make two 1.5% agarose phantoms for IV-OCT imaging. 5 different agarose gels were made, one for each section of the segmented phantom mould. These are pictured in Figure 3-2 (A) and the sections contain the following: 1- agarose only control, 2- USPIO 0.05 mg/ml, 3- USPIO 0.25 mg/ml, 4- USPIO 2.5 mg/ml and 5- USPIO 5 mg/ml. The dilution of USPIOs in each gel is easily inferable by the intensity of the iron colouration visible in the photo. The phantoms were subsequently imaged by IV-OCT with the catheter placed through the lumen in the middle of the phantom (where the needle is visible in the Figure 3-2 (A)). The numbered panels in Figure 3-2 show a representative cross-sectional OCT slice from each phantom section (from approximately 70 slices per section), the circle in the centre of each image is the imaging catheter and the rest of the image is the agarose gel. The 4 dark bands radiating from the catheter are imaging artefacts that were avoided when drawing ROIs for the image analysis steps. There does not seem to be any strong differences visible between the images of the 5 different sections suggesting USPIO alone doesn't affect the OCT signal.

The same bespoke phantom moulds were used to create a different set of 1.5% agarose gels for IV-OCT imaging. The 5 sections contained the following: 1) agarose only control, 2) 20 million untreated murine macrophages, 3, 4 and 5) 20 million murine macrophages loaded with 3 different concentrations of USPIOs - incubations at 0.05, 0.25 and 2.5 mg/ml respectively. 7 repeats of these phantoms were made, one of which is pictured in Figure 3-3 (A). Despite the particles being contained inside the cells, themselves embedded in agarose, the iron colouring of the different dilutions is visible. Figure 3-3 (B) is a transversal OCT image through the middle of the phantom and along the whole length, showing the 5 square gels each separated by the plastic walls (bright bands) and the catheter running through the centre of each. The numbered panels show a representative cross-sectional OCT slice from each phantom section (from approximately 70 slices per section). Contrarily to those in Figure 3-3, the OCT images from the different sections do have visual differences. In particular sections 2 to 5, which all contain cells, look distinct from the agarose only control: the depth penetration of the OCT signal is much reduced and there are many more, brighter spots. Although 2 and 3 look quite similar, image 4 shows a slight decrease in the signal depth penetration: the bright section has a smaller diameter around the catheter and the area past this is darker. The same again can be said for image 5 compared to image 4 – the OCT signal seems to drop off as it goes through the gel. These observations show that the presence of

macrophages has a big effect on the OCT signal and suggests that the presence of USPIOs inside the cells at a high enough concentration increases this effect.

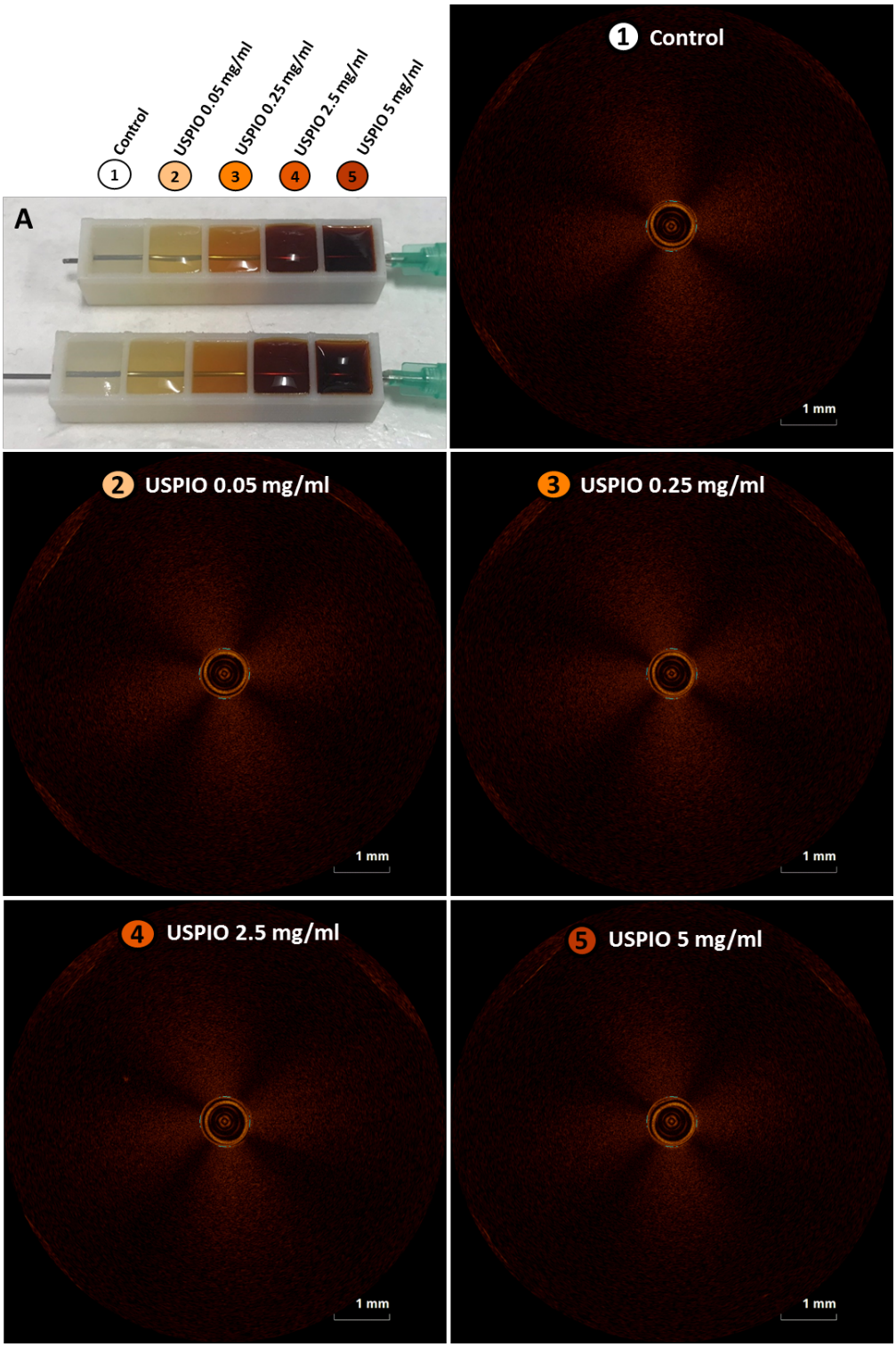

Figure 3-2: OCT imaging of a phantom model with different dilutions of USPIOs. (A) Photo of the two phantoms made with 1.5% agarose and varying dilutions of USPIOs in each section. (1-5) representative OCT slices through each section of phantom 1.

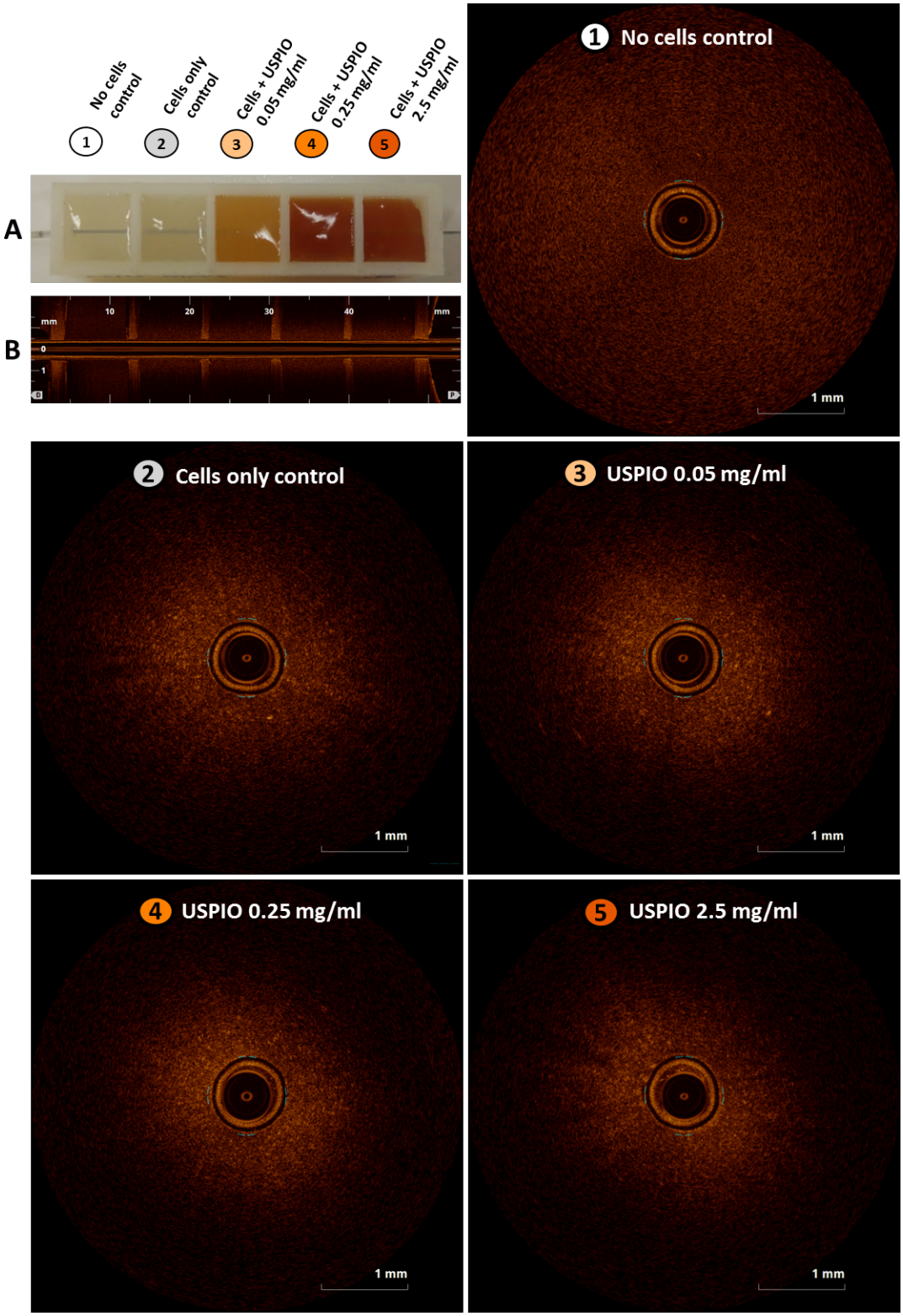

Figure 3-3: OCT imaging of a phantom artery model. (A) Photo of one of the 7 phantoms made with 1.5% agarose and 20x10^6 macrophages having been incubated with varying concentrations of USPIOs. (B) OCT image through the middle of this phantom showing each section, the plastic separations between them (bright vertical bands) and the OCT catheter (horizontal tube through the middle). (1-5) representative OCT slices through each section of the phantom.

3.3.3 Image analysis – USPIO alone

As explained in section 2.4, the standard deviation (SD) of the mean pixel intensity within certain regions of the OCT images was used as a metric of the "granularity" to measure the effects of the different phantom compositions. In order to avoid imaging artefacts, ROIs were drawn on each of the OCT slices and the SD values for each ROI were processed in Matlab as described in section 2.4. Figure 3-4 presents the mean of these SD values for each section of the two "USPIO alone" phantoms introduced in Figure 3-2. Figure 3-5 shows the image analysis results processed in the same way but using the mean pixel intensity within the ROIs rather than the SDs.

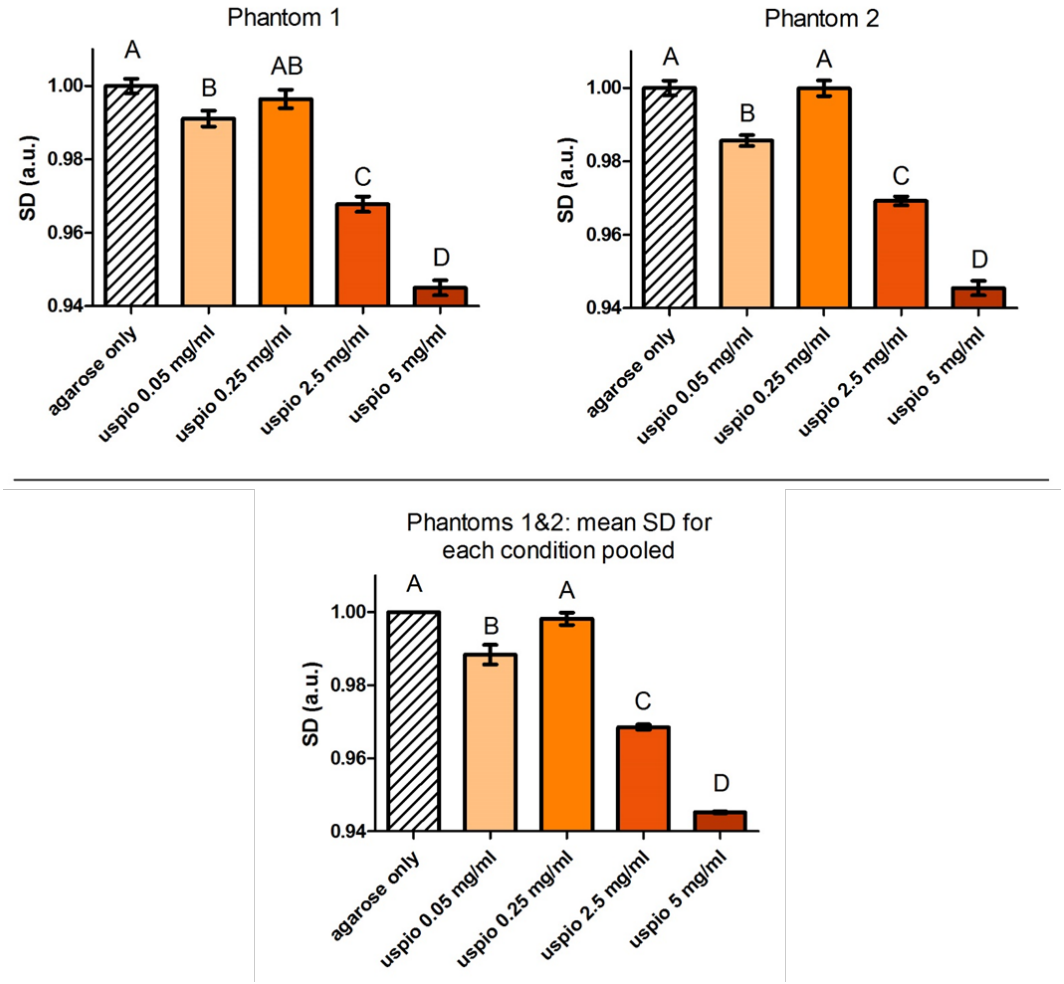

Figure 3-4: Top: standard deviation of pixel intensity analysis of OCT images from 2 phantoms made with 1.5% agarose and varying dilutions of USPIOs. Bottom: the mean intensities for each condition from both phantoms pooled. All values normalised to the agarose only control. Letters show results of statistical test, when two bars share the same letter they are not significantly different whereas different letters indicate significant difference ($p<0.05$).

For each phantom and for the pooled results, the mean SD (MSD) of the USPIO 0.25mg/ml gel shows no significant difference with the control. Aside from this, the presence of USPIOs in the other gels significantly lowered the MSD in a concentration dependant manner: with each increase in concentration the MSD becomes significantly lower. This shows that USPIOs alone reduce the "granularity" of the OCT image, contrary to what had been hypothesised. This is potentially due to the homogeneous nature of the USPIO spread within the gels – the particles are making the gels more opaque (visible in Figure 3-2 (A)), letting less light through and therefore dampening the overall OCT signal. This is corroborated by the fact that the mean intensity analysis (Figure 3-5) shows very similar results to the MSD ones: not only are the USPIO images less granular, they are also less bright as a whole.

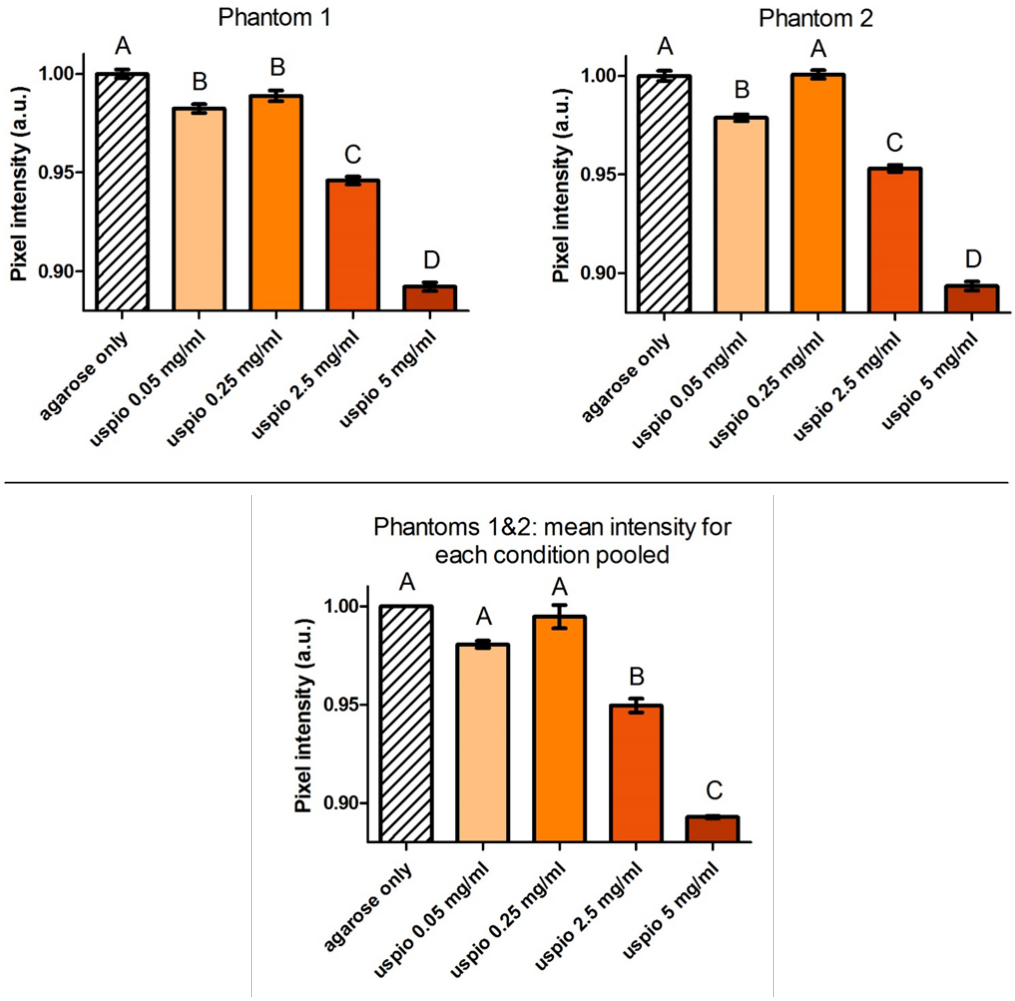

Figure 3-5: Top: mean pixel intensity analysis of OCT images from 2 phantoms made with 1.5% agarose and varying dilutions of USPIOs. Bottom: the mean intensities for each condition from both phantoms pooled. Values normalised to the agarose only control. Letters show results of statistical test, when two bars share the same letter they are not significantly different whereas different letters indicate significant difference ($p<0.05$).

3.3.4 Image analysis – USPIO laden macrophages

The macrophage loaded phantoms introduced in Figure 3-3 were analysed in the same way as the USPIO only ones presented above. The results of the MSD analysis of the 7 individual macrophage phantoms are presented in Figure 3-6 (phantoms 1 to 3) and Figure 3-7 (phantoms 4 to 7). The agarose only control gel made in each phantom had a significantly lower MSD compared to all other gels in each phantom ($p<0.001$) but the results are only shown for phantom 1 as a representative example (Figure 3-6, (1) Controls). This signifies that untreated macrophages reproducibly increase the OCT signal. In addition, the gel containing USPIO 0.25mg/ml treated macrophages showed a significant increase in MSD compared to untreated macrophages in every phantom made (see Figure 3-6 and Figure 3-7). This finding shows that USPIOs loaded into macrophages at this concentration do increase their contrast on OCT. Furthermore, 5 of the 7 phantoms also show the USPIO 0.05mg/ml gel having a significantly higher MSD compared to untreated, showing promise for this concentration also having an enhancement effect on the OCT images. However, the remaining two phantoms (2 and 7) show no significant difference between the USPIO 0.05mg/ml treated and untreated, suggesting this concentration does not produce consistent OCT contrast enhancement. Moreover, the macrophage gels treated with the highest USPIO dose (2.5mg/ml) showed much more variable MSD values between phantoms:

- Phantoms 1, 3 and 5 show USPIO 2.5mg/ml treatment significantly increases the MSD compared to untreated
- Phantoms 4 and 6 show USPIO 2.5mg/ml treatment to have no significant effect on the MSD compared to untreated
- Phantoms 2 and 7 show USPIO 2.5mg/ml treatment significantly decreases the MSD compared to untreated

When packaged into cells, USPIOs increase the MSD on OCT images but only at certain concentrations. When used at 2.5mg/ml they create a much more variable signal which could be traced back to behaviour when they are placed alone in agarose gels (not inside cells). In this case the presence of USPIOs renders the gels more opaque and less penetrable for the OCT light, reducing the overall intensity (Figure 3-5) of OCT images and also the MSD (Figure 3-4). At 2.5mg/ml, even when loaded into cells, USPIOs seem to cause the gels to be too opaque and reduce the overall OCT signal instead of increasing the variances in the pixel intensities as it does at lower concentrations.

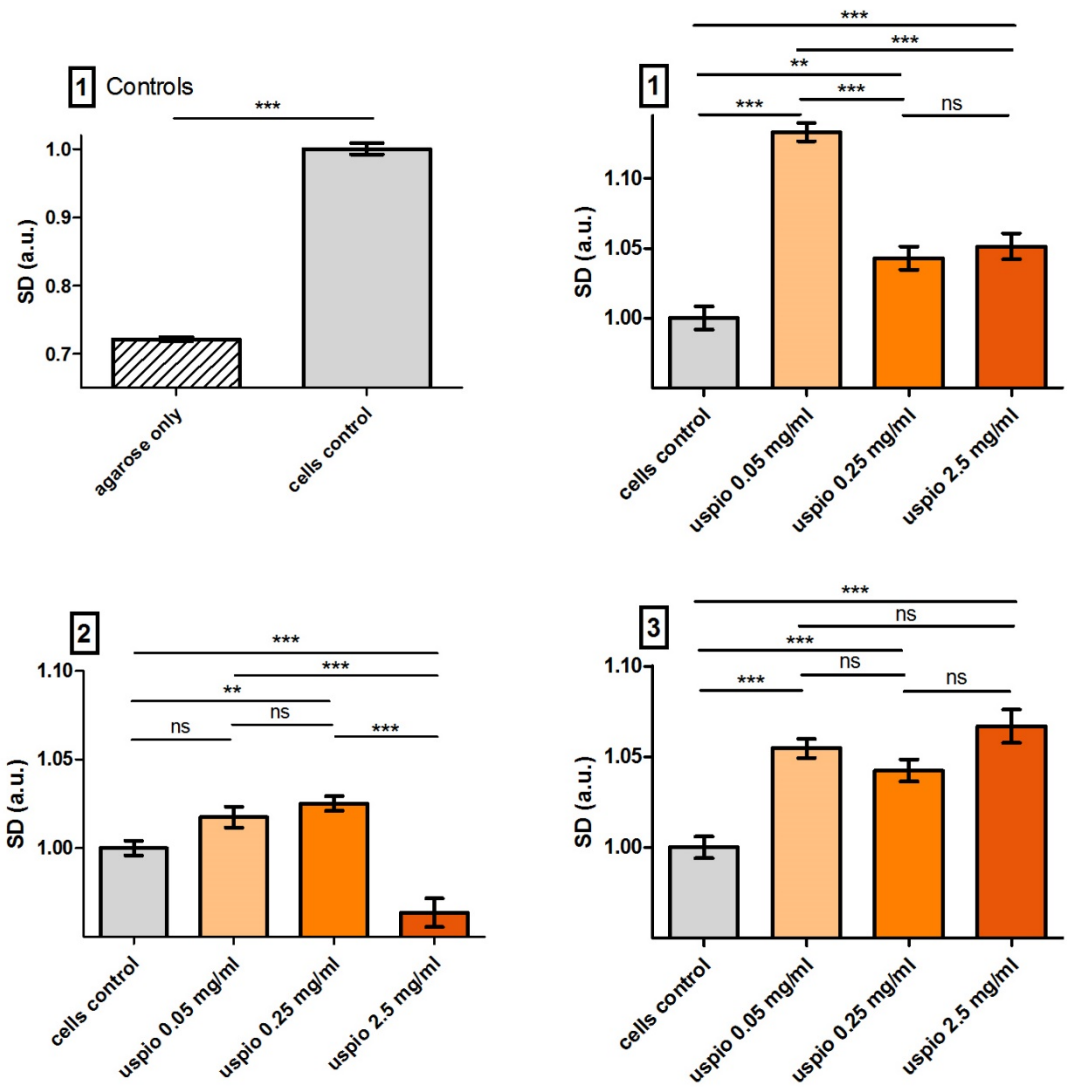

*Figure 3-6: Standard deviation of pixel intensity analysis of OCT images from 3 phantom artery models made with 1.5% agarose and mouse macrophages loaded with varying concentrations of USPIOs. Top left: the agarose only control of phantom 1 shows significantly lower SD compared to the cell control group as well as all other groups. All values normalised to cells control, ns= not significant, * p<0.05, ** p<0.01, *** p<0.001. Error bars = SEM.*

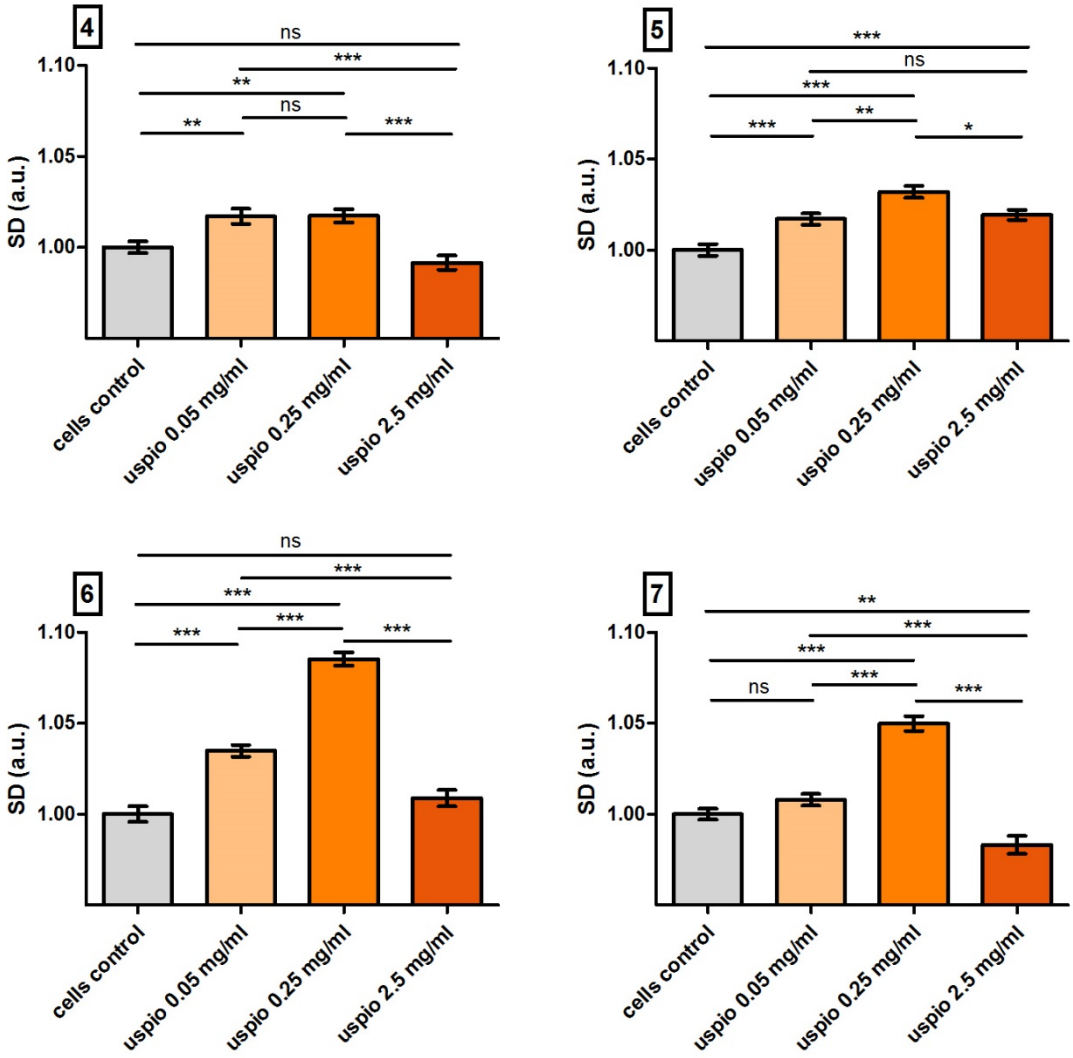

*Figure 3-7: Standard deviation of pixel intensity analysis of OCT images from 4 phantom artery models made with 1.5% agarose and RAW cells loaded with varying concentrations of USPIOs. Agarose only gels were also included in each of these phantoms and showed significantly lower mean SDs compared to all other gels. All values normalised to cells control, ns= not significant, * p<0.05, ** p<0.01, *** p<0.001. Error bars = SEM.*

Figure 3-8 shows the results of all 7 macrophage phantoms pooled together (≈1400 values per bar). From this figure, it is apparent that OCT images from USPIO treated macrophages (at all 3 concentrations) have significantly higher SD values than the untreated control. There is no significant difference between the USPIO 0.05 and 0.25 concentrations. However, the 2.5mg/ml concentration shows significantly lower mean SD compared to the other two, which is concurrent with the variability of the findings for this concentration in the individual phantoms.

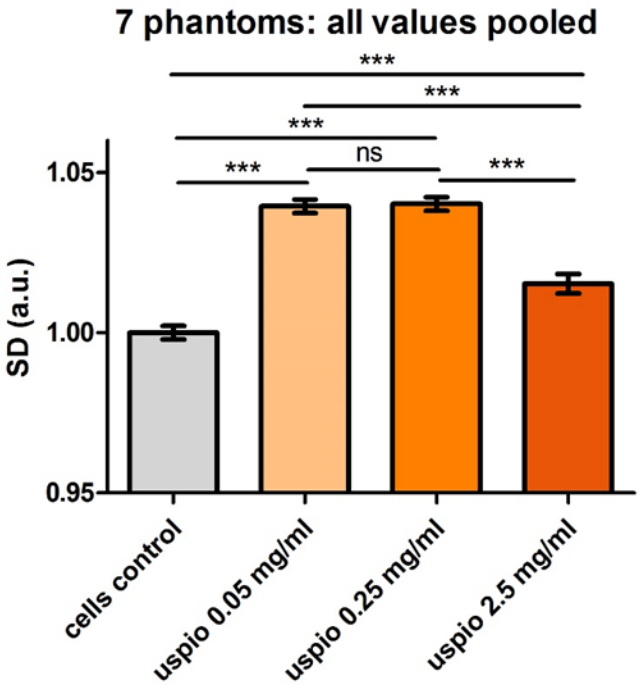

*Figure 3-8: Standard deviation of pixel intensity analysis of OCT images of all 7 macrophage phantom models pooled. Agarose only gels were also included in each of the phantoms and was found to have a significantly lower MSD than all other conditions. Values normalised to cells control, ns= not significant, * p<0.05, ** p<0.01, *** p<0.001. Error bars = SEM.*

3.3.5 SD hotspot visualisation tool

The MSD results presented above showed that USPIO can at certain concentrations significantly increase the local SD of OCT images when loaded into macrophages compared to untreated macrophages. It would however be useful to be able to visualise these increased SD regions in order to detect where specifically the macrophages are located. An SD hotspot visualisation tool was therefore developed in Matlab as described in section 2.4.3. OCT images from each treatment section of macrophage phantom 5 were selected for processing through this SD hotspot code to produce the colour map images presented in Figure 3-9 and Figure 3-10.

These hotspots seem to effectively convey the MSD results shown previously, with "cells only control" showing more spots than "no cells control" and "USPIO 0.05mg/ml" showing more spots still. The "USPIO 0.05mg/ml" and "USPIO 0.25mg/ml" images look relatively similar but the latter does show more darker spots indicating higher SD values which is concurrent with the findings in Figure 3-7 (5) when comparing the MSDs of the two treatments. Additionally,

the “USPIO 2.5mg/ml” image shows fewer spots than the previous dilution which corroborates the fact that it’s MSD is significantly lower. These images show an effective way of visualising areas of higher SD produced by the presence of macrophages. They also demonstrate the advantage USPIO loading can bring to this visualisation.

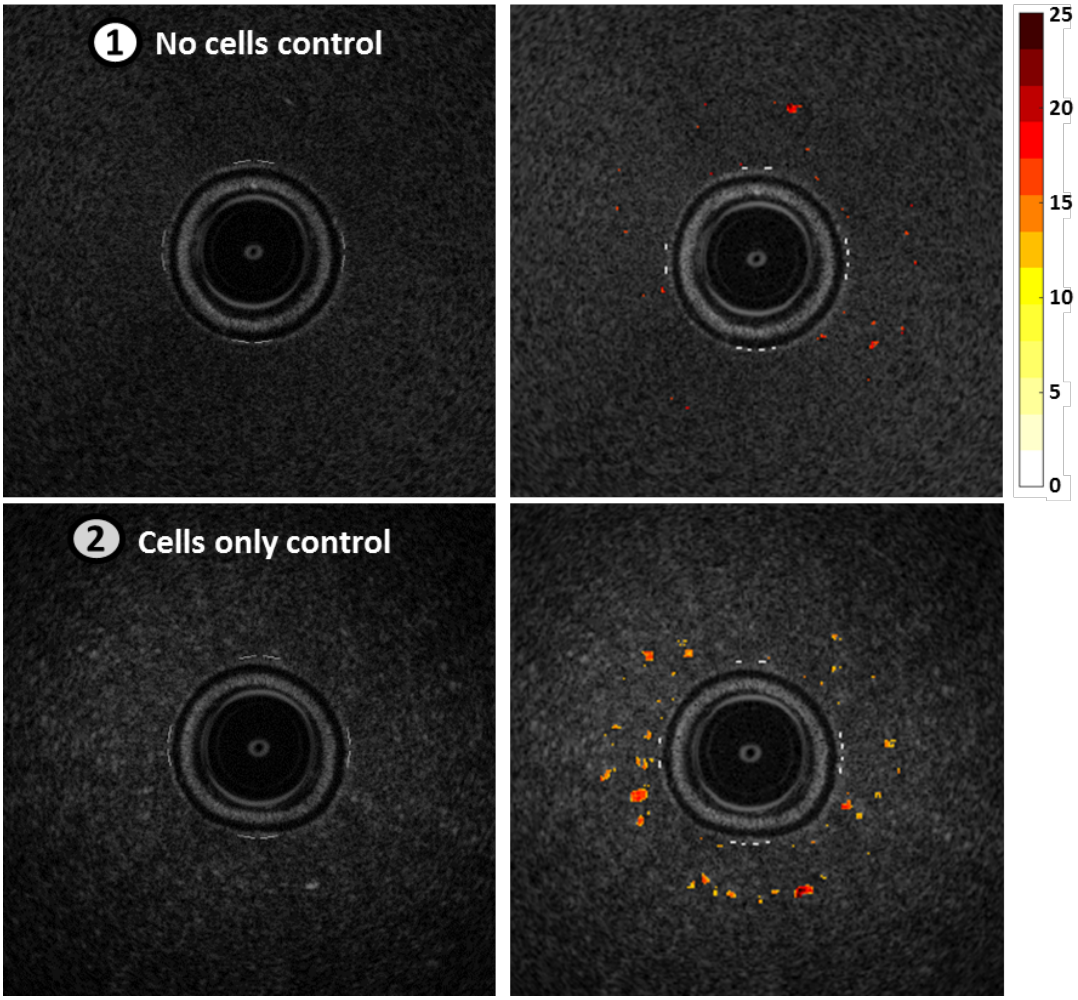

Figure 3-9: Standard deviation hotspots visualisation tool. Left shows OCT slices through the two control sections of phantom 5. Right are the same slices with a colour map overlay of areas of high standard deviation in pixel intensity (the colour scale is the same for all images).

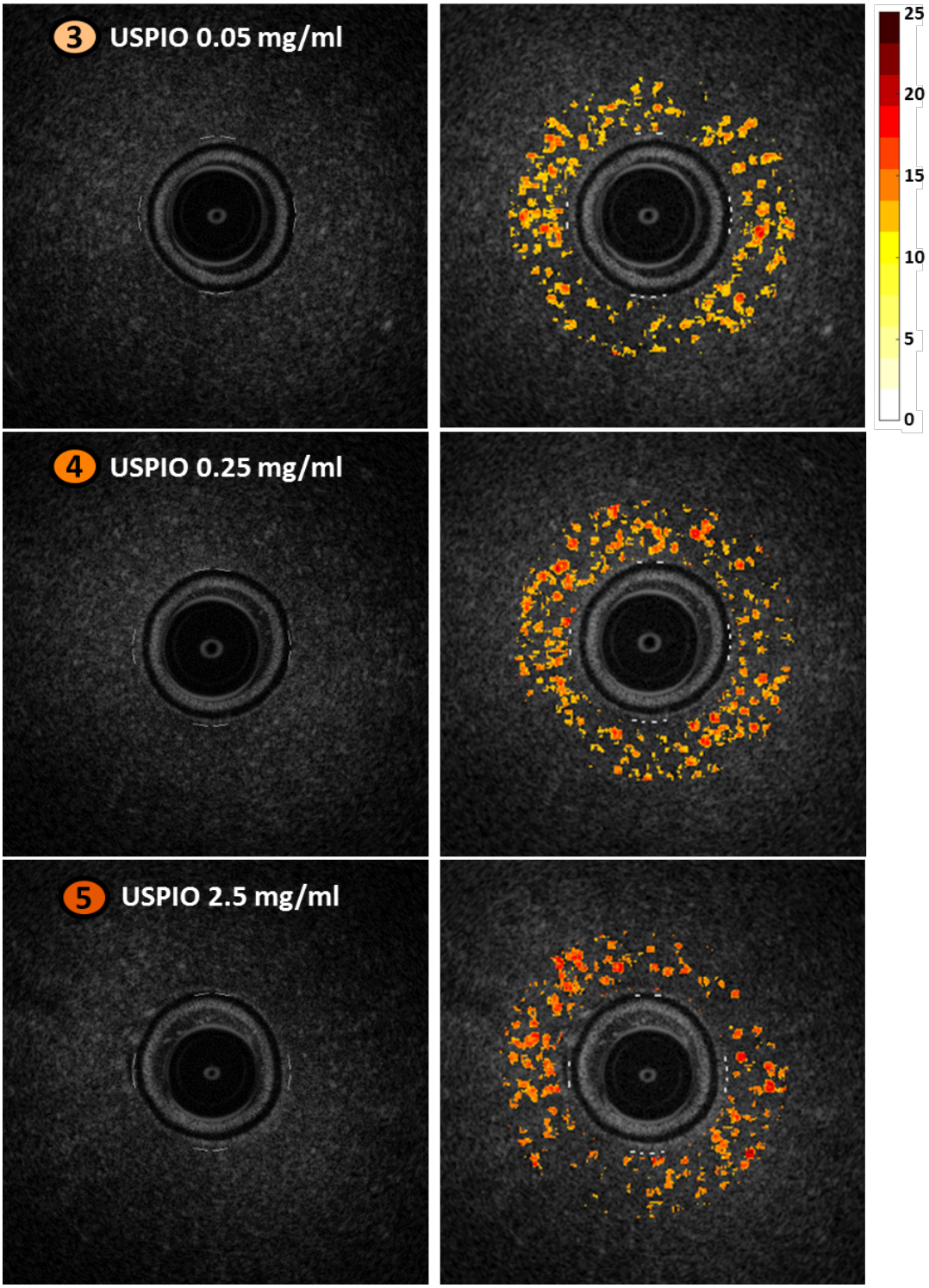

Figure 3-10: Standard deviation hotspots visualisation tool. Left shows OCT slices through the 3 USPIO-laden cells sections of phantom 5. Right are the same slices with a colour map overlay of areas of high standard deviation in pixel intensity (the colour scale is the same for all images).

3.4 DISCUSSION

To summarize, in this chapter the IV-OCT imaging properties of USPIO particles were investigated in vitro and there were four main outcomes. The first is that USPIOs were confirmed to be readily taken up by RAW cells in a dose dependent manner. Secondly, a robust phantom model and image analysis methodology was developed and lead to the successful IV-OCT imaging and quantification of cells and particles in vitro. Using this model, it was established that USPIO particles homogenously distributed in the gels by themselves do not increase the OCT signal in the way we expected: they dampen it instead. However, it was subsequently established that when loaded into cells, USPIOs actually enhance their OCT detectability. Each of these four outcomes will be discussed in more detail subsequently.

Firstly, section 3.3.1 investigated the uptake of USPIO particles by RAW cells to ensure appropriate loading of the cells before performing OCT experiments. It was determined, both visually (on microscopy imaging) and quantitatively that RAW cells reproducibly internalised USPIOs in a dose dependent manner after incubation with them for 24 hours, confirming **hypothesis 1**. Indeed, the Ferrozine iron quantification assays showed an incremental increase in intra-cellular iron when USPIO incubation concentration was increased between 0.03 and 3mg/ml. Particle uptake experiments with this particular USPIO (Ferumoxytol) have only been published in two papers which encouragingly found similar results, albeit by different means[7]. In fact, there have been very few in vitro studies involving the use of Ferumoxytol, perhaps because it is so similar to its predecessor, Ferumoxtran-10, differing only by its carboxymethylated dextran coat compared to plain dextran for Ferumoxtran-10. Although Ferumoxtran-10 has been found to be non-toxic to HMMs nor cause them to activate, release pro-inflammatory cytokines or affect Fc-mediated phagocytosis[96], these are important factors worth re-investigating specifically with Ferumoxytol. Similarly, only one study has investigated the uptake mechanism of Fermoxtran-10 by HMMs and suggested it to be fluid-filled transport[96] but this bears repeating with Ferumoxytol.

Section 3.3.2 presented IV-OCT images of our bespoke phantom model. The creation of this model involved designing and 3D-printing a mould and developing and optimising a brand new methodology for casting cell-laden agarose gels for IV-OCT imaging (section 2.3). This novel phantom model was very successful: it enabled easy and reproducible IV-OCT imaging of different experimental cell and particle combinations in one scan. On these IV-OCT images, cell presence was easy to visually discern compared to control agarose gel and the presence

of USPIO particles within the cells was also detectable by eye. Ariza de Schellenberger et al.[93] found similar results imaging RAW cells loaded with Ferumoxytol with the same OCT system but their phantom setup was not optimal; they held two Eppendorf tubes each with a cell pellet (with and without USPIO loading) next to the catheter for imaging. The first issue with this method, which they themselves mention, is that cell pellets are very dense and so will most likely produce much higher OCT contrast than macrophages normally distributed in plaque tissue. Our model, although not nearly a perfect recreation of plaque structure, at least holds macrophages more sparsely with approximately 40 000 cells in $1mm^3$. The second limitation of the Ariza de Schellenberger phantom setup is that the OCT light has to penetrate 3 optical boundaries (catheter/air/plastic tube) before hitting the cell pellet[93] whereas our system only has one optical boundary (catheter) before hitting the gel/cell sample. Additionally, they did not do any repeat experiments and had a different, more manual, image analysis method based on the backscatter coefficient. Although the image analysis methodology and software we created had a manual ROI drawing step, it enabled the rapid processing of hundreds of images for a more robust OCT signal analysis.

Section 3.3.3 presents the image analysis results of phantoms gels containing different concentrations of USPIO particles. We found that when USPIOs are alone and homogeneously distributed in the phantoms (not loaded into cells) they do not enhance the signal and instead actually dampened it. This effect was more severe with increased USPIO concentrations and this was reproducible over two phantom repeats. This means that **hypothesis 2** of this chapter "USPIOs held homogenously in an agarose gel will yield higher OCT contrast compared to an agarose only gel" is rejected. We theorize that this OCT signal dampening effect of USPIOs is due to the fact that when light travels through a homogenous medium the penetration depth decreases exponentially with the scattering and absorption properties. Meaning that when they are distributed homogenously in a gel USPIOs actually serve to make it more opaque – less light can travel through so the OCT image is less bright and less detailed. This theory makes sense given that the more USPIOs are present in solution, the more opaque the gel is to the naked eye and the lower the OCT image intensity is. Encouragingly, Ariza de Schellenberger et al. also encountered a similar effect when imaging USPIOs alone in suspension and made similar assumptions as us about the light scattering properties of USPIOs in homogeneous suspension[93].

Section 3.3.4 presented the image analysis results of phantom gels containing RAW cells and showed that they yield significantly higher OCT contrast compared to agarose only, confirming **hypothesis 3** of this chapter. This is the first time that the SD metric, first suggested to reflect macrophage presence by Tearney et al. in 2003[89], has been tested on macrophages in a controlled in vitro setting. Although the SD is understandably not zero on plain agarose images, it is significantly higher when cells are present in the gel, confirming their detectability on IV-OCT. Additionally, when USPIOs are loaded into these cells, the SD of OCT images is significantly increased compared to untreated cells, confirming **hypothesis 4** of this chapter. Again, similar results were found by Ariza de Schellenberger et al.[93] using a different image analysis method. Like us they theorise that this effect is due to the increased size of USPIOs when they are aggregated into the phagolysosomes of cells which makes them better at scattering light and therefore increasing the SD on OCT images. We found that this increase in OCT contrast of macrophages loaded with USPIOs was mostly reproducible for two of the USPIO concentrations tested (0.05 and 0.25 mg/ml). However, the third and highest incubation concentration (2.5mg/ml) tested produced much more variable results across the individual phantoms made, with a couple showing that this concentration significantly decreased the OCT signal compared to untreated cells. This shows that USPIOs at too high a concentration in cells can revert back to an OCT signal dampening effect, perhaps due to rendering the whole gel more opaque as they do when imaged alone in suspension. We were therefore able to establish 0.05mg/ml as an appropriate concentration for USPIO use in OCT imaging that we used as the basis for designing our subsequent mouse and human studies.

Finally, section 3.3.5 presented a bespoke OCT SD hotspot visualisation tool which accurately represented the quantitative results obtained previously. This is the first time that a tool such as this has been shown to pick out and visually represent macrophages on OCT images in a controlled in vitro setting (where only macrophages are present). Indeed, we observed many more hotspots on OCT images from gels containing cells compared to agarose alone and many more still when the cells were pre-loaded with USPIOs, confirming **hypothesis 5** of this chapter.

There are however a few limitations to the work of this chapter. Firstly, due to the presence of artefacts on the OCT images it was necessary to manually draw ROIs on all images. It would of course be better to develop an automated whole image analysis method but this is difficult

to do without forfeiting a lot of image information and altering results (due to background removal and filtering steps for example). Looking forward to in vivo plaque OCT imaging, whole image analysis is not currently possible due to the complexity and variability of plaque structure and appearance. So our method of ROI drawing stays closely translatable to what is possible in clinical image analysis. Another limitation of this study is the lack of co-registration of macrophages in the gel (on histology) to the SD hotspots uncovered in the image analysis. This would have been a nice addition to further confirm the association of high SD with individual macrophage accumulations but was beyond the scope of this translational study. Finally, although the SD hotspot tool mostly produced very convincing images, there was some variability to these results when processing different images from the same gel. Although these are not presented here (due to length constraints), it bears mentioning that this method was the first iteration with improvement possible with further research.

In conclusion, this novel in vitro study has served as a robust proof of concept for the use of USPIOs (Ferumoxytol) to enhance the IV-OCT detectability of macrophages. USPIOs were shown to be readily taken up by macrophages. A bespoke phantom model and image analysis method were developed and used to show that USPIOs enhance the detectability of macrophages with IV-OCT. And this OCT signal enhancement was effectively visualised using a novel standard deviation of pixel intensity hotspot tool. Chapter 4 will follow on from this with the next step in the translational USPIO-OCT study: investigating USPIO uptake by macrophages in atherosclerotic plaques of ApoE -/- mice and their detection by IV-OCT imaging ex-vivo.

4 CHAPTER FOUR: EX VIVO MOUSE USPIO-OCT STUDY

4.1 INTRODUCTION

In Chapter 3 it was established that in an in-vitro phantom setting USPIOs are readily taken up by mouse macrophages (RAW cells) and that this enhances macrophage detectability with IV-OCT. This chapter aims to validate these in-vitro results in an animal model of atherosclerosis and is therefore the second stage of our 3-part translational study investigating the USPIO-enhanced detection of plaque macrophages on IV-OCT.

As established in section 1.1.3 the ApoE knockout ($ApoE^{-/-}$) mouse is a widely used animal model which spontaneously develops atherosclerotic plaques sharing many of the features of human coronary plaque progression including plaque rupture[27,131–135]. The atherosclerotic process can be accelerated to produce larger plaque when $ApoE^{-/-}$ mice are fed a high fat diet[27,131–135]. As described previously (sections 1.1.5 and 3.1) there are many incentives for refining the detection of macrophages on IV-OCT, yet to date only two studies have attempted OCT imaging of atherosclerosis in mice[80,83]. The first aimed to identify the key components of vulnerable plaques in $ApoE^{-/-}$ mouse, investigating their brachiocephalic arteries both in vivo and ex-vivo[80]. Although this study found excellent correlation between the OCT and histology measurements for lipid core size and fibrous cap thickness they used a bench top OCT system with an operating light source of 830nm wavelength[80]. This is therefore not closely comparable to the IV-OCT currently used in the clinic which operates at 1300nm. Additionally, with this OCT system, plaques could only be imaged from outside the vessel and they did not investigate the presence of macrophages in the plaques and whether these created a detectable change in the OCT images.

The second study on OCT imaging of $ApoE^{-/-}$ mouse plaques used a clinical IV-OCT system and attempted to detect and quantify the presence of macrophages within the imaged aortic plaques[8]. Excitingly, the IV-OCT system they used had a small enough imaging catheter (0.48mm) for in-situ intra-aortic imaging, albeit after euthanizing the mice[8]. In this study, Tahara et al. were able to successfully correlate macrophage presence on histological and OCT images with their bespoke semi-automated macrophage quantification tool[8]. However this software required a training procedure in which someone manually marked out “macrophages” on OCT images based on their location in the corresponding histology slide[8] – a process which is obviously not feasible to implement in humans. Additionally, this study used an older generation Time-Domain OCT (TD-OCT) system which produces lower quality images and is no longer clinically relevant compared to its replacement, the Frequency

Domain (FD-OCT) system[136–138] which has a catheter that is almost double the diameter (0.9mm).

Other studies have used MRI to demonstrate USPIO enhanced detectability of plaque macrophages in ApoE$^{-/-}$ mice[102–104]. Indeed these studies showed accumulation of USPIO particles within the macrophages of mouse atherosclerotic plaques on histology slides which were easily detectable with MRI[102–104]. However, until now, no one has attempted to image the plaques of USPIO treated ApoE$^{-/-}$ mice with IV-OCT. This was the intention of this chapter, with the help of the image analysis tools developed and optimised in the previous chapter. We raised ApoE$^{-/-}$ mice, treated them with or without USPIOs (at the concentration optimised in the previous chapter) and imaged their aortic plaques with IV-OCT. Initially, one of our main aims was to perform a histological analysis of the aorta tissues after OCT imaging to confirm the presence of USPIO-laden macrophages in the plaques and co-localise areas of high macrophage burden on histology with areas of high OCT signal. However, this histology study, performed by external collaborators at the University of British Columbia was severely delayed by the advent of the COVID-19 pandemic and could not be finalised in time for inclusion in this thesis. The remaining four aims and four associated hypotheses of this chapter are outlined below:

AIM 1 (section 4.3.1): To successfully induce the formation of atherosclerotic plaques in the aortas of ApoE$^{-/-}$ mice and to successfully identify their morphology on OCT images.

Hypothesis 1: Aortic plaques of ApoE$^{-/-}$ mice will be visible and identifiable in the excised and dissected tissue and their morphology on OCT will closely resemble that of lipid-rich human atherosclerotic plaques: with a bright outer cap and a dark blurry lipid core.

AIM 2 (section 4.3.2): To determine whether ApoE$^{-/-}$ mouse plaque caps produce a higher OCT signal compared to healthy aortic wall tissue within the same vessel.

Hypothesis 2: The caps of the aortic plaques will yield higher OCT signal (using the standard deviation of pixel intensity metric) than healthy aortic wall tissue regardless of treatment.

AIM 3 (section 4.3.2): To determine whether USPIO treatment of ApoE$^{-/-}$ mice enhances the OCT signal in the plaque caps compared to saline placebo treatment.

Hypothesis 3: **The caps of the aortic plaques of USPIO treated mice will yield higher OCT signal (using the standard deviation of pixel intensity metric) than those of saline treated mice.**

AIM 4 (section 4.3.3): To test whether the SD hotspot overlay tool accurately visually represents the SD analysis results in the mouse aorta images.

Hypothesis 4: **There will be more, high intensity hotspots on the caps of the plaques compared to healthy aortic wall tissue and this difference will be more marked in USPIO treated mice compared to saline control.**

If successful, this ex vivo murine investigation and image analysis methodology will develop our in-vitro work and pave the way for the use of USPIOs as a new OCT contrast agent to image atherosclerosis in man (Chapter 5).

4.2 METHODS

The ApoE$^{-/-}$ mouse was selected as the best model for the needs of this project due to the similarity of its atherosclerotic plaque structure to those of humans[131–135]. The mouse facilities and expertise in ApoE$^{-/-}$ mouse models in our research centre were also contributing factors to this decision. All experiments were performed according to the Animals (Scientific Procedures) Act 1986 (UK Home Office). Adult male ApoE$^{-/-}$ mice (N = 10) were purchased from Charles River (Margate, UK) aged 8-9 weeks (20-25g) and received a high fat 'Western Diet' (21% fat; Research Diets, New Brunswick, USA) to induce lipid-rich plaque formation in the aortic arch. Three mice were sacrificed due to injuries from in-fighting in the first few weeks and an additional mouse had to be culled due to disease after 24 weeks. On week 25, 1.9µl of USPIO (Ferumoxytol by Rienso®) or saline placebo per ml of blood was administered by tail-vain injection (by Dr Rodger Duffin) 12 hours prior to cull by CO_2 overdose. This USPIO dose (1.9µl per ml) equates to the 0.05mg/ml of Fe demonstrated to give optimal OCT contrast in the in vitro Chapter 3. Three mice received a USPIO injection and three a saline placebo in order to compare the OCT signal in the plaques with and without USPIO.

Pre-study optimisation involved testing whether mouse aortas can be imaged intact using the Dragonfly™ OPTIS™ OCT catheter. As can be seen on Figure 4-1 (C) an intact mouse aorta has approximately the same outer diameter as the catheter (1mm). This made introduction of the catheter into the vessel very technical and resulted in a compressed view of the arterial wall on the OCT images (shown in Figure 4-1(A)). It was therefore determined that mouse aortas are too narrow to be imaged by intra-coronary OCT systems without damaging the plaque or impairing the OCT image detail. To overcome this issue, the aortas were harvested and carefully cut open from the descending aorta up to the aortic root along the outside of the aortic arch (so as not to disrupt the plaque on the inner curve of the arch) as is demonstrated in Figure 4-1 (D). For OCT imaging, the aortas were then pinned onto Sylguard® (The Dow Chemical Company) coated petri dishes, plaque side up, immersed in saline and the catheter was laid and held in place on top as is demonstrated in Figure 4-1 (E). This dissection and imaging method results in clearer OCT images of mouse aortas as exemplified in Figure 4-1 (B) and in the figures of section 4.3.1. Following OCT imaging, the murine aortic tissues were fixed in 4% PFA for 18h and embedded in paraffin wax for tissue sectioning and histological validation of the USPIO signal. The histological study performed by external collaborators (Dr Stephanie Sellers' group at the University of British Columbia) was delayed by the COVID-19 pandemic and was still not available at the time of submission.

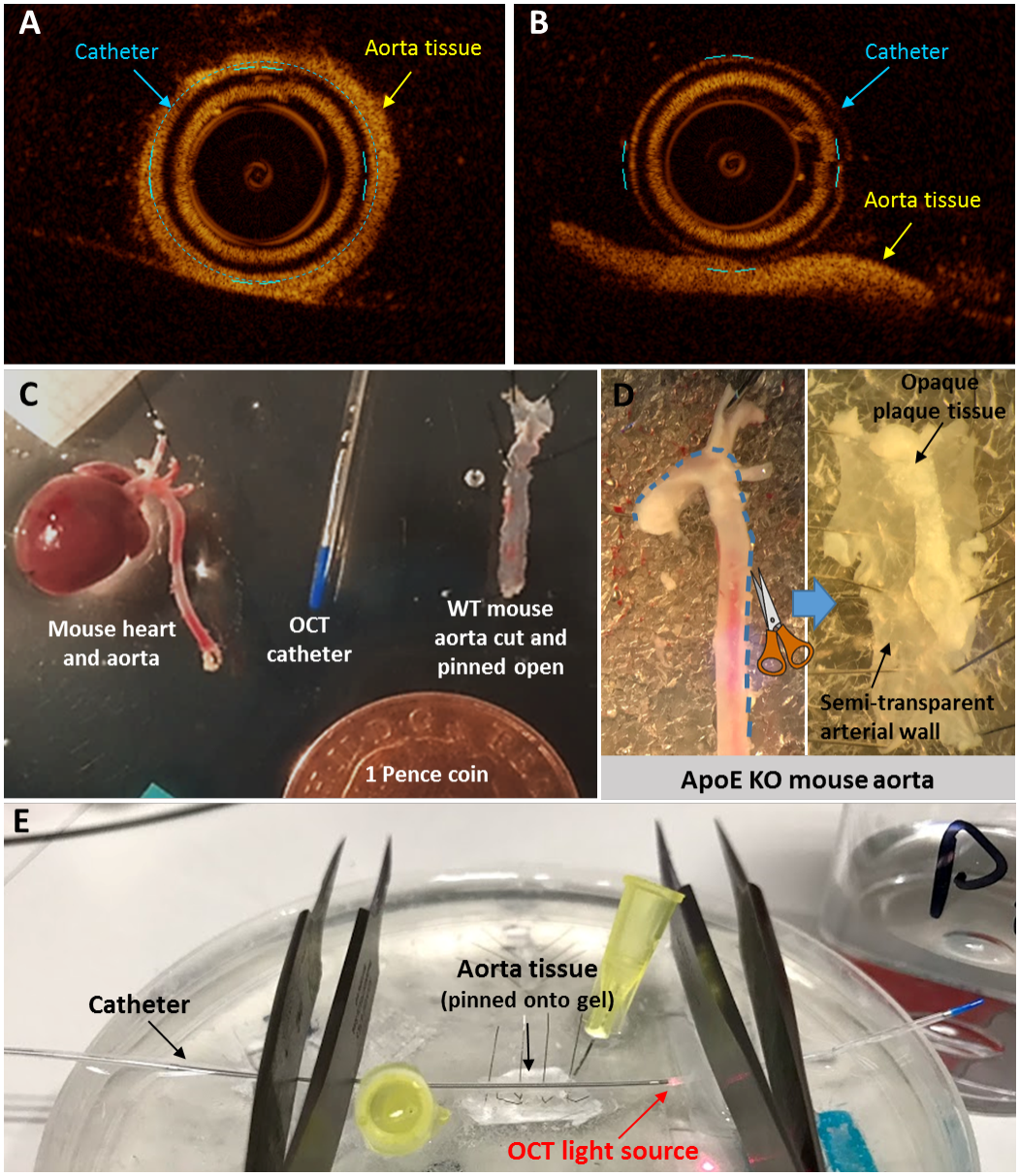

Figure 4-1: Imaging and dissection protocol. (A) OCT image through an intact WT mouse aorta. (B) OCT image of the same aorta after cutting and pinning it open. (C) Photo showing the size of an intact WT mouse heart and aorta, the OCT catheter and another WT mouse aorta after being cut and pinned open. (D) Images showing how the aorta incisions are made to avoid disturbing the aortic plaque. (E) Photo of the mouse vessel OCT imaging setup.

Similarly to the in-vitro work in the previous chapter, the aortas were imaged using the St Jude system and image analysis was performed using the custom methods and software described in section 2.4. The standard deviation of the mean pixel intensity within specific regions of the OCT images was used in this analysis to determine differences in OCT contrast enhancement between the two treatments: USPIO and saline. And the bespoke OCT SD hotspot tool was tested on sample images to render a visual representation of these OCT contrast differences.

4.3 RESULTS

4.3.1 Mouse vessels OCT imaging

The six ApoE$^{-/-}$ mouse aortas are pictured down the dissecting microscope on the numbered panels of Figure 4-2 (saline treated mice) and Figure 4-3 (USPIO treated mice) after being cut open along the outside of the aortic arch and pinned onto a Sylgard® gel. On these photos the normal aortic wall tissue appears slightly transparent and is easily distinguishable from the opaque white mass that is plaque tissue. Each of the six aortas have a large plaque in the centre of the tissue, starting from the top (the aortic root) and ending three quarters of the way down the tissue. In the intact aorta this location corresponds to the curve of the ascending aorta in which atherosclerotic plaques commonly form in western diet fed ApoE$^{-/-}$ mice[131]. Aside from aorta 4 (which unfortunately is not clearly visible due to the white background) each vessel also has small plaque portions on the left and right edges of the tissue, which correspond to the openings of the brachiocephalic, left carotid and left subclavian arteries. These artery branching points are also common areas for plaque formation in ApoE$^{-/-}$ mice[131].

As outlined in the methods, each mouse vessel was imaged by OCT pullback scan to produce a stack of approximately 40 cross sectional images along the whole length of the pinned aorta tissue. One representational OCT image of the aortic plaque as well a non-plaque section of aorta from each mouse are shown in the lettered panels of Figure 4-2 (saline treated mice) and Figure 4-3 (USPIO treated mice). The plaques on images A, C and E of both figures are easily distinguishable as protrusion with a bright outer edge and a blurry darkened interior. This is similar to human plaques on OCT, the bright outer edge corresponds to the cap of the plaque, below which there is a blurry region and the OCT signal drops off. This dark signal drop off area corresponds to the lipid pool of the plaque, below which nothing more can be observed. Conversely, the non-plaque control sections (B, D and F) show a much more homogenous, mostly flat tissue with no signal drop off. Below the aortic wall tissue in these images, imperfections in the Sylgard® gel (SL) can be seen as diagonal lines. These SL imperfections can be seen in some of the “plaque section” images (Figure 4-2 C and E) below the normal aorta tissue (left of the plaque on both C and E) but never below the plaque tissue itself, confirming that the plaques absorb more OCT light and are therefore lipid rich.

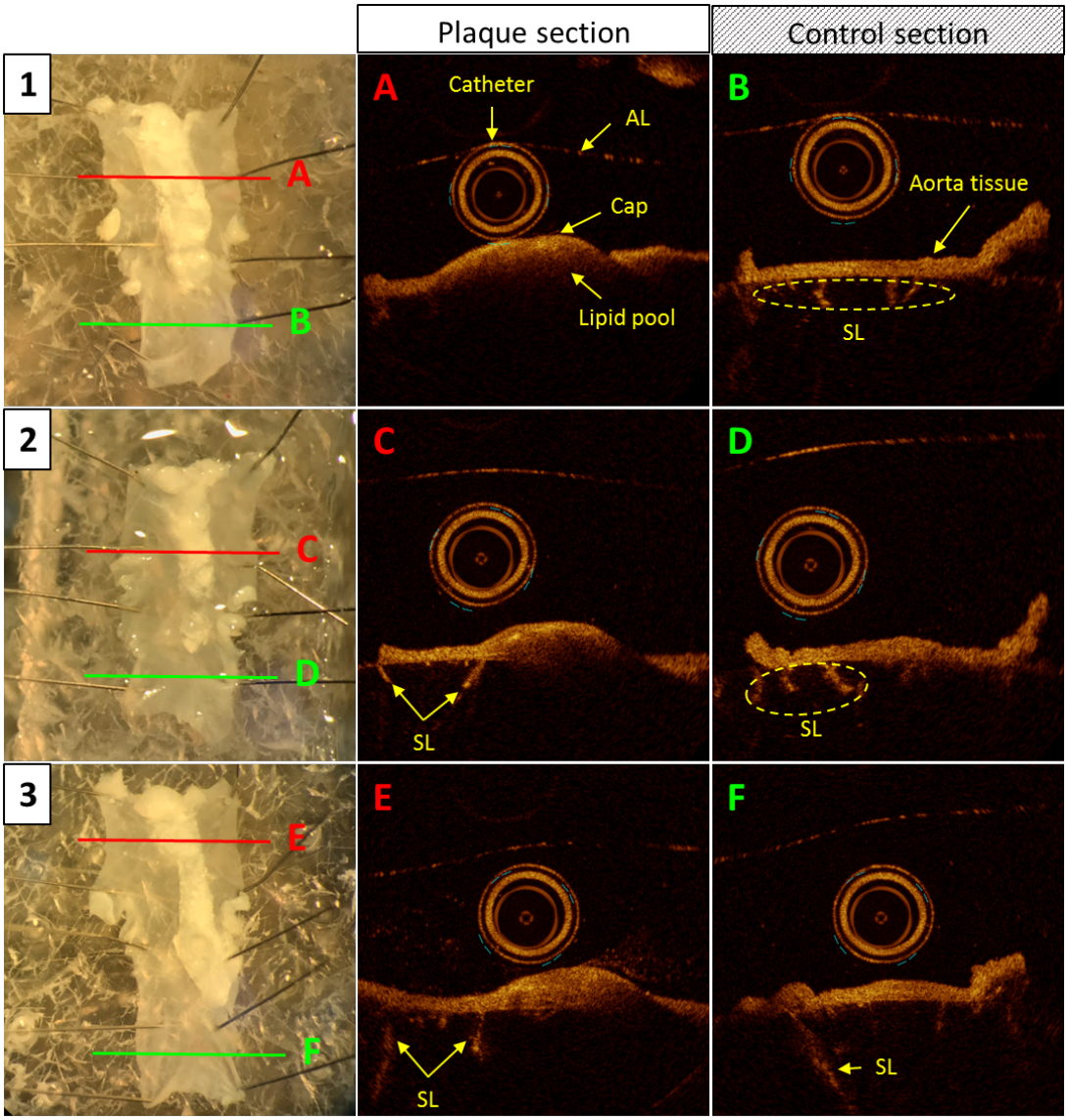

Figure 4-2: Aorta images of three ApoE$^{-/-}$ mice treated with saline placebo. Panels 1-3 are photos through the dissecting microscope of each aorta (from mice 1-3), cut open and pinned out onto a Sylgard® gel. The lettered panels show representative OCT slices through the corresponding aortas. A, C and E are OCT images of the plaque containing sections of aortas 1, 2 and 3 respectively. B, D and F are representative OCT images of the normal "control" tissue of aortas 1, 2 and 3 respectively. AL: air-liquid interface artefact. SL: Sylgard® gel artefacts.

When qualitatively comparing the OCT images of control mice aortas (Figure 4-2) and USPIO treated mice aortas (Figure 4-3) not many conclusions can be drawn. Visually, the control sections of aortas from mice 1-6 are near identical, with none standing out as brighter or more punctuate than the rest. When it comes to the plaque section images, there is more variation, for instance, the images from mice 1, 4, 5 and 6 show a much more extensive

plaque (width-wise) than the images from mice 2 and 3. Additionally, the images from mice 2, 5 and 6 show a few spots in the cap of the plaque that are significantly brighter than the rest of the tissue whereas the caps of mice 1, 3 and 4 appear to have much less variation in pixel intensity. However, these differences are most likely due simply to natural variation in plaque structure and size between mice. In order to discern any real differences in OCT signal between the two different treatments, a quantitative investigation was performed and the results are presented in the following section.

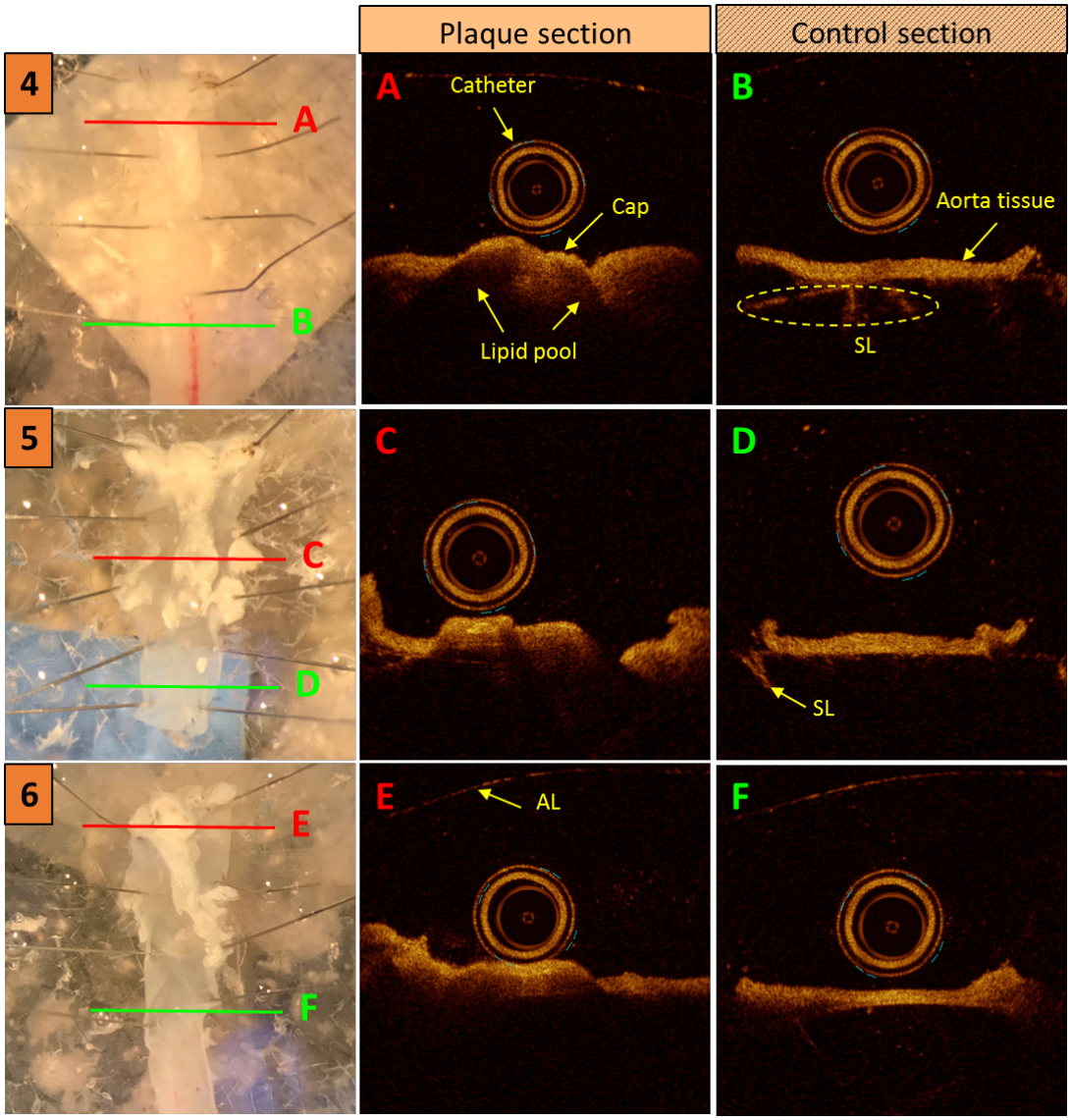

Figure 4-3: Aorta images of three ApoE$^{-/-}$ mice treated with USPIO. Panels 4-6 are photos through the dissecting microscope of each aorta (from mice 4-6), cut open and pinned out onto a Sylgard® gel. The lettered panels show representative OCT slices through the corresponding aortas. A, C and E are OCT images of the plaque containing sections of aortas 4, 5 and 6 respectively. B, D and F are representative OCT images of the normal "control" tissue of aortas 4, 5 and 6 respectively.

4.3.2 Mouse vessels OCT image analysis

For each mouse aorta, regions of interest (ROIs) were drawn on every OCT image of the pullback scan (88 images per aorta), amounting to approximately 175 ROIs per mouse. The final number of ROIs drawn depends on the length of each plaque, the size and position of the tissue and the number of artefacts present on the areas of interest. One set of these ROIs were drawn in the cap of the plaques and another in the healthy aortic wall of the non-plaque control section described previously. See section 2.4.1 for detail on ROI drawing methodology. The pixel information within these ROIs was then processed using a custom Matlab code (see section 2.4.2). As with the phantom OCT data, the metric of interest is the standard deviation (SD) of the mean pixel intensity within the ROIs. For each of the 6 mouse aortas, the SDs of the ROIs drawn in the plaque caps were averaged, and are presented as non-patterned plain white and plain orange bars in Figure 4-4. The SDs of ROIs drawn in the healthy "control" aortic wall tissue were also averaged and are presented as the striped white and striped orange bars in Figure 4-4. The colours of the bar charts represent the treatment, with white charts 1, 2 and 3 showing results from each of the 3 saline treated mice. And orange charts 4, 5 and 6 showing results from each of the 3 USPIO treated mice. The datasets for each mouse are normalised to the control so each control value is 1 and the plaque SD values range from 1.107 to 1.182. The standard error of the mean (error bars) are small due to the high N numbers (ranging from 26 to 136 for individual bars) which correspond to the number of ROIs drawn over many images. For each individual mouse, the plaque mean SD is significantly higher than the control mean SD ($p<0.001$). This confirms the hypothesis that $ApoE^{-/-}$ mouse plaque cap components (most likely macrophages) significantly change the OCT signal compared to normal artery wall tissue.

When looking at the plaque mean SD values of saline versus USPIO treated mice in Figure 4-4, not many conclusions can be drawn. Saline treated mouse 2 has the highest plaque mean SD value at 1.182 ± 0.01404 (N=75), followed by USPIO treated mice 6 and 4 with 1.172 ± 0.01703 (N=87) and 1.168 ± 0.01216 (N=136) respectively. Then comes saline treated mouse 1 with 1.135 ± 0.01220 (N=127) and lastly USPIO treated mouse 5 at 1.107 ± 0.01193 (N=116). From these results, neither of the treatments stand out as superior for OCT plaque contrast enhancement. In order to properly compare the two treatments, the data from mice 1,2 and 3 (saline treated) need to be pooled together and analysed against that of mice 4, 5 and 6 (USPIO treated), as is presented in Figure 4-5.

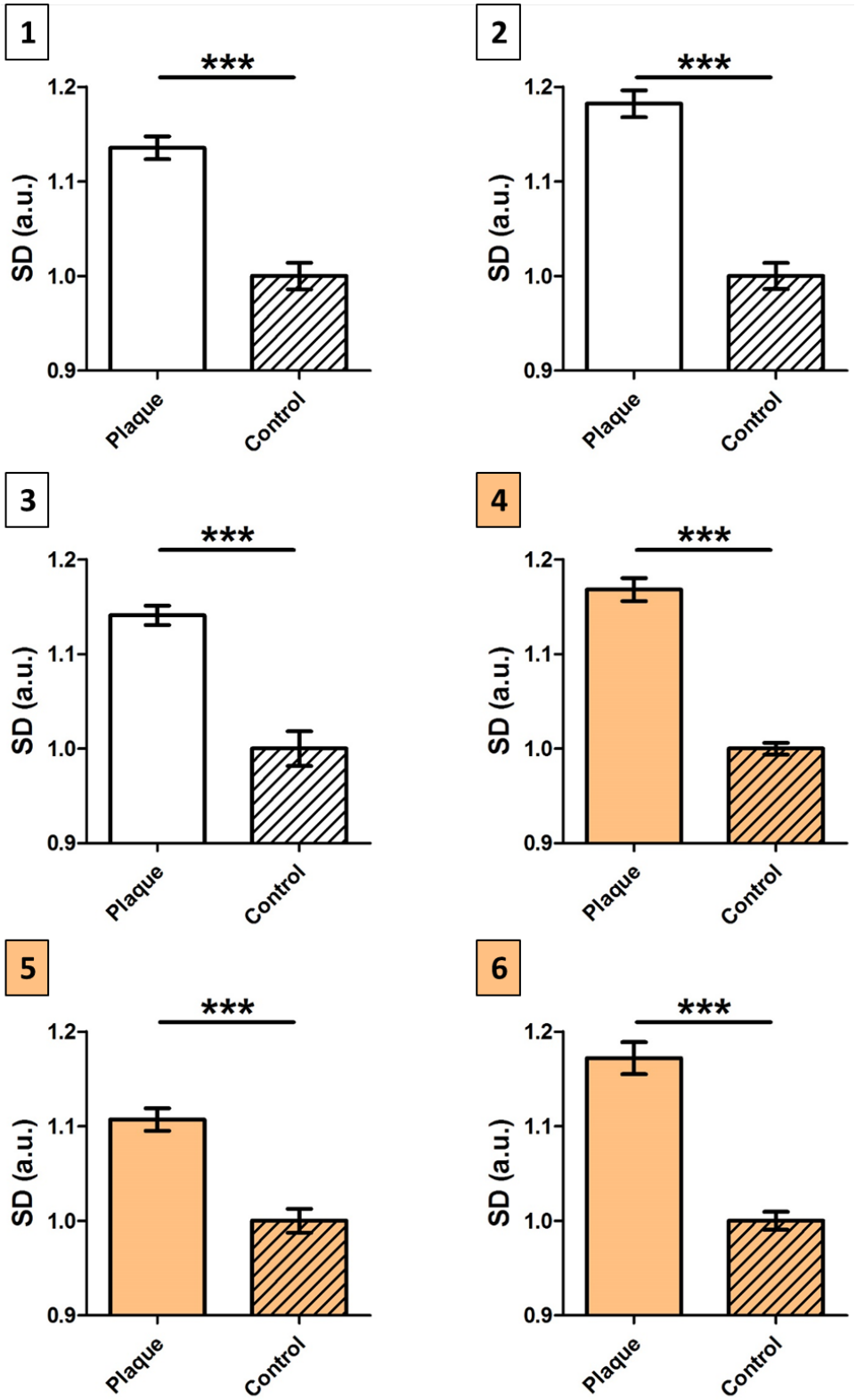

*Figure 4-4: Standard deviation of pixel intensity analysis of OCT images from 6 excised aortas of ApoE $^{-/-}$ mice. Mice 1-3 were injected with a saline placebo and mice 4-6 were injected with USPIO. Mean SD values from the plaque section and non-plaque control section are shown for each mouse. All values normalised to control, ns= not significant, * p<0.05, ** p<0.01, *** p<0.001. For each bar N>26. Error bars = SEM.*

When the data is pooled together in this way and normalised to the saline control (Figure 4-5), there is no significant difference between the control sections in the two treatment groups but there is a significant difference between the plaque sections in the two treatment groups. As expected from the previous results, both treatment groups showed that plaque tissue had a significantly higher mean SD than control healthy tissue with $p<0.001$. Although the mean SD of the control tissue from the USPIO treated mice (1.016 ± 0.005296 N=299) is higher than the control tissue from the saline treated mice (1 ± 0.009583 N=115), this difference is not significant, with $p=0.1225$. However, the mean SD of the plaque cap tissue from USPIO treated mice (1.166 ± 0.007977 N=339) is significantly higher than that of saline treated mice (1.144 ± 0.007110 N=301) with $p<0.05$. This means overall, USPIO treatment increases the OCT signal in ApoE$^{-/-}$ mouse aortic plaques but does not affect the OCT signal in their healthy aortic tissue. This last point is of particular importance because it shows that USPIO treatment does not raise the OCT signal non-specifically. Instead, it enhances the high signal associated with plaque inflammation without affecting that of aortic wall tissue with little inflammation.

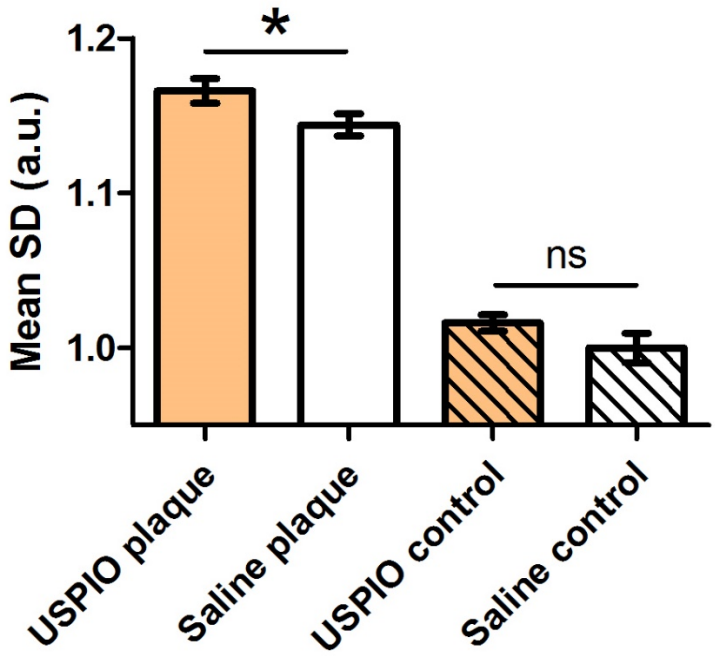

*Figure 4-5: Standard deviation of pixel intensity analysis of OCT images from 3 USPIO treated ApoE $^{-/-}$ mice pooled and 3 saline treated control ApoE $^{-/-}$ mice pooled. Mean SD values from the plaque section and non-plaque control section are shown for USPIO and saline mouse groups. All values normalised to "saline non-plaque", ns= not significant, * p<0.05, ** p<0.01, *** p<0.001. For each bar N>115. Error bars = SEM.*

4.3.3 SD hotspot visualisation

The SD results presented above showed that USPIO treatment of ApoE$^{-/-}$ mice can significantly increase the local SD of plaque OCT images compared to placebo treated ApoE$^{-/-}$ mice. It would however be useful to be able to visualise these increased SD regions in order to detect their specific locations within the plaque tissue and whether these co-localise with macrophage accumulations in the histological analysis. An SD hotspot visualisation tool was therefore developed in Matlab as described in section 2.4 and a selection of mouse aorta OCT images were processed. Figure 4-6 shows two OCT images from a plaque section (A and B) and one image from a control non-plaque section (C) of saline treated mouse 1's aorta with (right) and without (left) the SD hotspot overlay. Similarly, Figure 4-7 shows two OCT images from a plaque section (A and B) and one image from a control non-plaque section (C) of USPIO treated mouse 4's aorta with (right) and without (left) the SD hotspot overlay.

The raw OCT images (left of Figure 4-6 and Figure 4-7) are difficult to distinguish from each other, however after application of the SD hotspot tool (right panels) it is clear that the plaques from the USPIO treated mouse (Figure 4-7 A and B) have more hotspots than the saline plaques (Figure 4-6 A and B). These visual differences between USPIO and saline plaques are concurrent with the quantitative results obtained in the previous section. In particular Figure 4-6 (B) (saline plaque image) shows a few barely visible, small hotspots whereas all the other images have much larger hotspots. On Figure 4-7, in the USPIO mouse, it is clear that the control section (C) has fewer hotspots than the plaque sections (A) and (B), which again is concurrent with the quantitative results. However, in the saline mouse (Figure 4-6), the control section (C) actually appears to have more hotspots, although lower in value (yellow rather than red), than plaque sections (A) and (B). The results of this hotspot map image processing are mixed. Some individual OCT cross-sections reflect the overall quantitative results observed in the previous section while others do not. In these mouse aorta images, the hotspot processing is very variable between sections of the same plaque and there is often not a clear distinction in hotspot cover between plaque and non-plaque areas. This signifies more work is needed to optimise this visual tool specifically for the mouse aorta system to more closely reflect the positive quantitative analysis results.

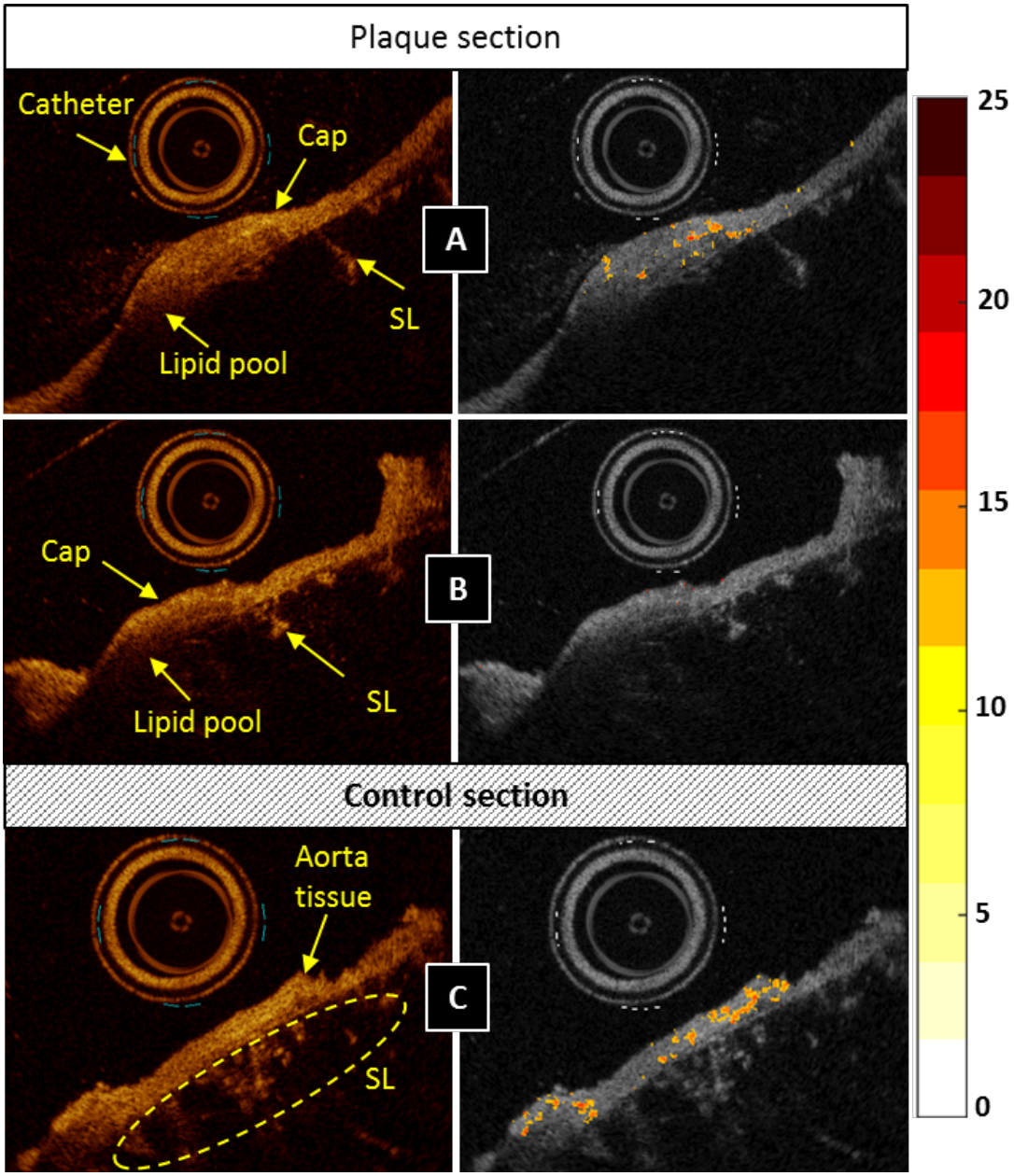

Figure 4-6: Standard deviation hotspots visualisation tool on saline treated mouse images. Left shows raw OCT slices through the aortic tissue with plaque (A, B) and without (C). Right are the same slices with a colour map overlay of areas of high standard deviation in pixel intensity (the colour scale is the same for all images).

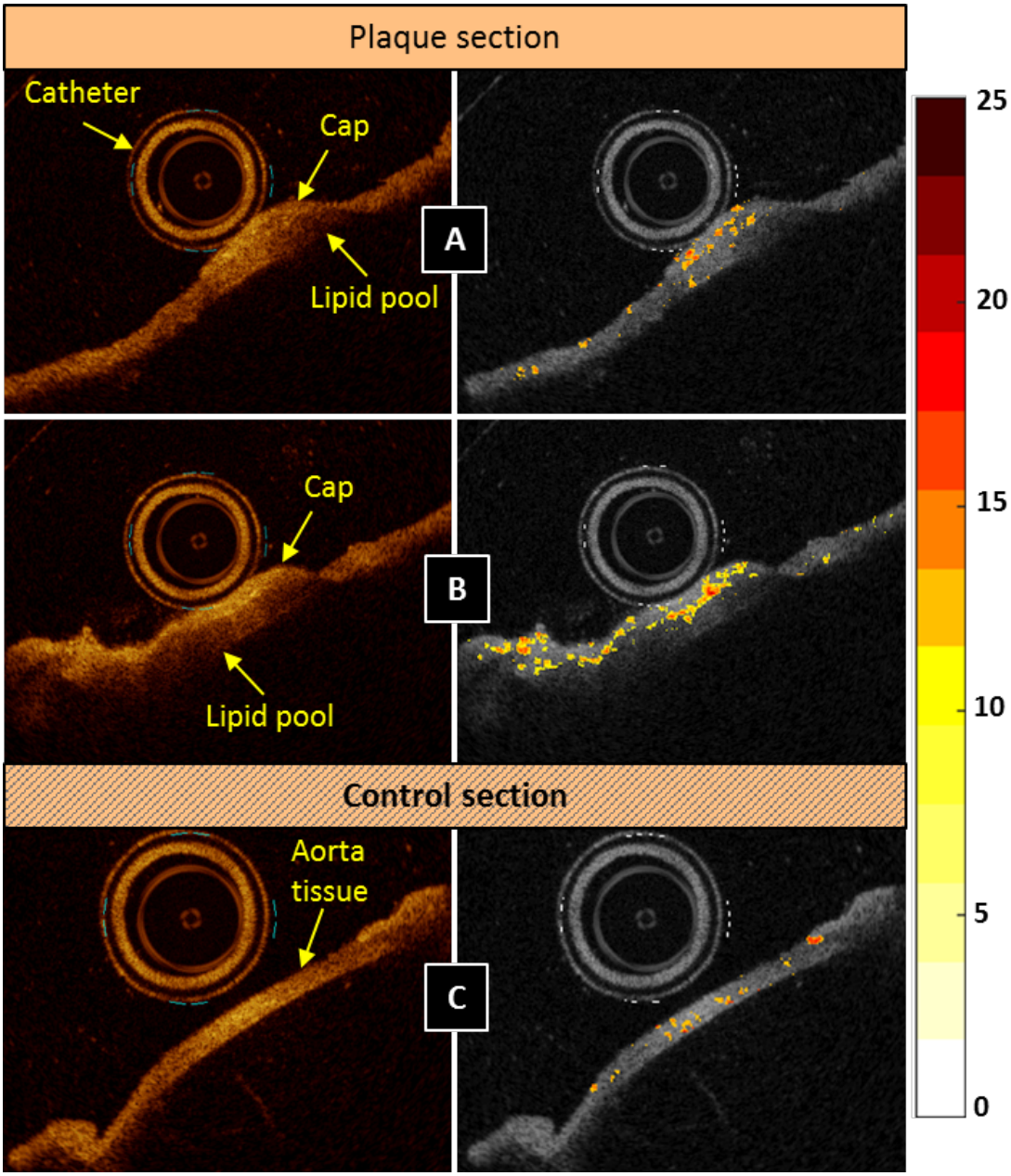

Figure 4-7: Standard deviation hotspots visualisation tool on USPIO treated mouse images. Left shows raw OCT slices through the aortic tissue with plaque (A, B) and without (C). Right are the same slices with a colour map overlay of areas of high standard deviation in pixel intensity (the colour scale is the same for all images).

4.4 DISCUSSION

To summarize, in this chapter the IV-OCT imaging properties of USPIO particles were investigated in ApoE$^{-/-}$ mouse aortic plaques and there were four main outcomes. The first is that we successfully imaged ApoE$^{-/-}$ mouse aortic plaques with the St Jude IV-OCT system and their morphologies were clearly distinguishable on the OCT images. Secondly, using the novel image analysis method developed in section 2.4 and first presented in Chapter 3, we determined that the caps of murine plaques significantly enhanced the OCT signal compared to healthy aortic wall regardless of treatment. Using the same image analysis methods it was found that treatment with USPIO significantly increases the OCT contrast in plaque caps but does not affect that of healthy tissue. And finally, the SD hotspot tool presented in the last Chapter was implemented in the mouse images and found to support most of the quantitative results obtained. Each of these four outcomes will be discussed in more detail subsequently.

Firstly, section 4.3.1 presented, for the first time, IV-OCT images of ApoE$^{-/-}$ mouse aortic plaques taken with the current, routinely used Ilumien Optis™ (St. Jude) OCT system. In order to achieve this, we developed a protocol whereby the aortas were cut open and the catheter was placed on top of the open aorta (on the inside). This had to be done because the clinical catheter (made for human coronary arteries) is approximately the same diameter (0.9mm) if not larger than mouse aortas. The six mice we raised on a high fat diet all successfully developed large aortic plaques whose lipid pool and fibrous cap were clearly visible on the OCT images, confirming **hypothesis 1** of this chapter. Indeed, in the OCT imaging of each of the 6 mice, the plaques appeared as protrusions from the aortic wall which had a bright outer edge (the fibrous cap) below which the OCT signal dropped off, indicating the presence of a lipid rich pool. Encouragingly, the aortic plaque OCT images obtained by Tahara et al. in their study showed very similar morphology and theirs correlated well with the plaque structure observed on histology slides[8].

Section 4.3.2 presented the image analysis results of the murine vessels and showed that plaque caps produced significantly higher OCT signal compared to the healthy aortic wall control tissue regardless of treatment, confirming **hypothesis 2** of this chapter. This is the first time that the SD metric, first suggested to reflect macrophage presence by Tearney et al. in 2003[89], has been tested on murine atherosclerotic plaque images. Although the SD is understandably not zero in the healthy aortic wall tissue, it was significantly lower than the

plaque tissue SD in every individual mouse (Figure 4-4). Ideally we would have been able to correlate the increased MSD in plaque caps with macrophage presence on histology slides but unfortunately this was not ready in time. It would also have been interesting to see whether this OCT SD metric was able to accurately grade the density of macrophages present.

The third main outcome of this chapter is that USPIO treatment significantly increased the OCT signal of murine plaque caps compared to saline control treatment, confirming **hypothesis 3**. As is presented in Figure 4-5, when the data from all mice are pooled together in order to compare the treatment groups with each other, it was found that the overall MSD of the plaque caps of USPIO treated mice were significantly higher than that of saline treated mice. Importantly, USPIO treatment did not significantly enhance the OCT signal of the control healthy aortic wall tissue, confirming that the particles do not end up non-specifically in the vessel walls. However, an important point to note is that not every USPIO treated mouse had higher plaque cap SD values than every saline mouse – it is only when the data from the different mice are pooled together that we can observe a difference between the treatments. This is likely simply due to the natural variation in plaque macrophage burden between mice; it could be the case that the saline treated mouse with the highest SD value (mouse 2) happened to have developed more severe disease with a much higher macrophage burden in its plaques. It could also be the case that the USPIO treated mouse with the lowest SD value (mouse 5) had less severe disease and lower plaque macrophage burden. Again, variability in plaque macrophage burden between mice is something that could have been confirmed with the histology analysis which was intended to be included here.

Finally, section 4.3.3 presented a bespoke OCT SD hotspot visualisation tool which appears to accurately represent most of the quantitative results obtained previously. This is the first time that a tool such as this has been shown to pick out and visually represent macrophages on OCT images in mouse atherosclerosis. Indeed, we observed many more hotspots on the plaques of USPIO treated mice compared to the healthy aortic wall, partly confirming **hypothesis 4**. However, in saline treated mice the difference in number of hotspots between plaque and control tissue was not as clear cut, which was not expected based on the quantitative results presented previously (all mice had higher SDs in the plaques compared to control). This limitation will be discussed subsequently.

There are a few limitations to the work of this chapter. Firstly, the study population was quite small due to the loss of 4 mice and therefore it could be worthwhile re-investigating with a higher power study. Secondly, we unfortunately could not include the histological analysis of the mouse aortas in this chapter due to COVID-related delays. This means we could not directly confirm that USPIO particles have made it into plaque macrophages. This has however been demonstrated in detail in multiple previous studies using USPIOs at comparable concentrations as an MRI contrast agent in ApoE$^{-/-}$ mice[102–104]. Because of the lack of histology data we also cannot confirm that the raised SD values in plaque caps compared to healthy aortic wall is specifically due to macrophage presence. However, the fact that USPIO treatment does not raise the MSD in healthy control tissue (Figure 4-5) is a good indicator that USPIOs are actually transported by macrophages to the inflammation site (plaque caps) and cause a significant raise in SD. The final limitation is with regards to the SD hotspot map tool: although promising in vitro, it seems a little less accurate in this mouse system. Indeed, non-plaque areas look like they have a lot of hotspots, almost as many as some of the plaque areas and this was also the case for other images analysed and not shown here. This effect could be due to the micro-structure in the mouse healthy arterial wall causing a lot of variation and therefore more optimisation could be done to improve the technique in mice specifically.

In conclusion, following on from the previous chapter, this novel mouse imaging study has served as a second robust proof of concept for the use of USPIOs to enhance the IV-OCT detectability of macrophages in vivo. In this chapter, protocols were established for the successful ex-vivo imaging of ApoE$^{-/-}$ mouse plaques with a clinical IV-OCT system. The OCT scans revealed clear lipid-rich plaques with fibrous caps resembling those of humans in each of the six mice. The bespoke image analysis software and methods presented in the previous chapter were used here to find that USPIO treatment (informed by optimal concentration determined in Chapter 3) significantly enhances plaque OCT signal compared to saline treatment but does not affect the signal of control tissue. And this OCT signal enhancement was effectively visualised using a novel standard deviation of pixel intensity hotspot tool. Chapter 5 will follow on from this with the final step in the translational USPIO-OCT study: enhanced detection of inflammation in acute coronary syndrome patient plaques using USPIO.

5 CHAPTER FIVE: IN VIVO HUMAN USPIO-OCT CLINICAL TRIAL

5.1 INTRODUCTION

In the previous two chapters, it was established that USPIOs enhance the detection of macrophages with IV-OCT in vitro and in a mouse model. Building on this, as the last stage of these translational studies, in this chapter we investigate whether USPIOs can enhance IV-OCT detection of macrophages *in vivo* in human atheroma.

As presented in section 1.3.2, Tearney et al. first demonstrated a linear correlation between macrophage accumulations in the caps of lipid rich atherosclerotic plaques (on histology) and the local normalised standard deviation (NSD) on OCT images[89]. By taking the standard deviation of pixel intensity within a specific region of an OCT image, the variability of the OCT signal in that ROI can be quantified with the presence of macrophages in theory increasing this value. This pioneering study involved ex-vivo, enface imaging of arterial segments (aortas and carotid bulbs) from randomly selected cadavers with a bench-top OCT system[89]. Therefore no association between cap macrophage burden and clinical status could be made, although this was later addressed in a study by MacNeill et al.[92]. This study related NSD values in the caps of coronary plaques to disease severity in patients presenting with coronary artery syndrome imaged with IV-OCT[92]. It was found that patients with acute coronary syndromes (MI and unstable angina) had significantly higher NSD than those with stable angina[92]. Additionally, culprit plaques had higher NSD compared to non-culprit ones within the same patient but this difference was not significant[92]. One limitation of this study was that the authors only analysed 3 OCT images per plaque. A few years later, another study by Raffel et al. successfully determined that thin-capped fibroatheromas (TCFA) had significantly higher NSD than non TCFA in patients suffering from ACS[139].

One key limitation of all three of the mentioned studies is that the NSD parameter by its nature, cannot be specific to macrophages only. Indeed different components such as cholesterol crystals and some calcifications have been found to cause high NSD values[57]. Whilst ROIs can be restricted to the caps of plaques (as these studies have done) to reduce the risk of false positives, this ignores macrophages and inflammation deeper within the plaque and brings considerable challenges in the accurate and reproducible delineation of drawing ROIs over such small structures. One interesting recent study tried to overcome these issues by developing a new IV-OCT macrophage detection method which automatically identified plaque areas with high NSD which had areas of signal attenuation (with low NSD values) directly below them[140]. This technique was based on a previous report that

macrophages produce signal-rich regions with punctuate bright spots and cause signal attenuation below, presenting as a shadow in the underlying tissue[141]. Although this study reports their new technique to identify macrophages with 88% sensitivity and specificity when correlated with histology sections, this was done using only one OCT image for each human coronary artery plaque collected post-mortem[140]. This was therefore quite a small preliminary analysis which did not attempt to make any connections between in vivo macrophage burden and clinical status.

Although a few studies have tried variations on the NSD analysis method in an attempt to more sensitively detect macrophages, as of yet no one has attempted to enhance the OCT detectability of macrophages in vivo using a tagging agent. In this thesis we propose that nanoparticles loaded into macrophages can increase the local SD on IV-OCT images and thus enhance their detectability in fibrous caps of vulnerable plaques. This would hopefully address the issue of non-specificity of the SD metric as well as increasing sensitivity. As demonstrated previously, USPIOs look to be the perfect nanoparticle to fill this need because their accumulation in plaque macrophages has been extensively demonstrated[105–107]. Our preliminary investigations of the IV-OCT contrast potential of USPIOs in vitro (Chapter 3) and in $ApoE^{-/-}$ mice (Chapter 4) have yielded very positive results. We have brought the optimised image analysis methods and USPIO concentrations forward into this chapter investigating the USPIO enhanced detection of macrophages in vivo in patients presenting with ACS. The three aims and three associated hypotheses of this chapter are outlined below:

AIM 1 (section 5.3.1): To determine whether the caps of ruptured plaques produce a higher OCT signal compared to those of stable atherosclerotic lesions from the same patients.

Hypothesis 1: The caps of the culprit plaques will yield higher OCT signal (using the standard deviation of pixel intensity metric) than those of non culprit plaques regardless of treatment.

AIM 2 (section 5.3.1): To determine whether USPIO treatment of ACS patients enhances the OCT signal in the culprit plaque caps compared to saline placebo treatment.

Hypothesis 2: The caps of the culprit plaques of USPIO treated patients will yield higher OCT signal (using the standard deviation of pixel intensity metric) than those of saline treated patients.

<u>AIM 3 (section 5.3.2):</u> To test whether the SD hotspot overlay tool accurately visually represents the SD analysis results in the patient plaque images.

<u>Hypothesis 3:</u> There will be more, high intensity hotspots in the caps of the culprit plaques compared to those of non-culprit plaques and this difference will be more marked in USPIO treated patients compared to saline control.

If successful, this technique would permit a detailed examination of the role of macrophages in the pathophysiology of atherosclerosis in vivo in man and may lead to early identification of vulnerable patients with a high vulnerable coronary plaque burden at high risk of suffering a heart attack.

5.2 METHODS

This clinical trial was conducted by Dr Nick Cruden with the aim to enhance plaque macrophage detection with OCT. This trial was approved by the South East Scotland Research Ethics Committee 01 on 22/07/2014. Twenty patients presenting to the Royal Infirmary of Edinburgh with acute Type 1 myocardial infarction and scheduled to undergo diagnostic coronary angiography were recruited prospectively. Myocardial infarction was defined as a rise in cardiac troponin associated with new ischaemic electrocardiographic changes and / or a history of cardiac chest pain according to the third Universal definition[6]. Patients were randomised to receive 4 mg/kg UPSIO (Ferumoxytol by Rienso®) or saline injection 12-24h prior to invasive coronary angiography. This USPIO dose equates to 0.05mg/ml which was the concentration demonstrated to give optimal OCT contrast in the in vitro Chapter 3 and in the mouse Chapter 4. Culprit and non-culprit plaque were identified by the interventional cardiologist (Dr Nick Cruden, Dr Simon Wilson or Dr Andrew Mitchell) based on the clinical presentation, electrocardiographic changes, echocardiography and angiographic findings.

OCT imaging was performed using the commercially available Lunawave OFDI system (Terumo, Tokyo, Japan). Briefly, a 2.6F imaging Fastview OFDI catheter (Terumo, Tokyo, Japan) was advanced into the coronary artery over a standard 0.014" coronary guide wire and an automated pullback performed at 20 mm/s across the lesions of interest: both culprit and non-culprit coronary plaques. A simultaneous intracoronary injection of undiluted X ray contrast (omnipaque 300) at 4 ml/s was used to achieve a blood-free field of view. In patients presenting with a recent myocardial infarction both the culprit lesion and a remote epicardial vessel (control) was assessed using OCT. Following OCT imaging, percutaneous coronary intervention was performed according to routine clinical practice. Due to randomisation issues and one exclusion based on image quality, the final study population consists of 8 USPIO treated patients and 11 saline treated patients. Additionally, one of the USPIO treated patients did not undergo imaging of a remote non-culprit plaque, however the data from their culprit plaque imaging was still included in the pooled analysis. Image analysis was performed blinded to the treatment information using the custom methods and software described in section 2.4. The standard deviation of the mean pixel intensity within specific regions of the OCT images was used in this analysis to determine differences in OCT contrast enhancement between different plaques (culprit and non-culprit) and between different patient treatment groups (USPIO and saline). In addition, the bespoke OCT SD hotspot tool

(developed in section 2.4.3) was tested on sample images to render a visual representation of these OCT contrast differences.

For each patient plaque, regions of interest (ROIs) were drawn in the caps of the plaques (shoulders and centre of the cap) on each of 8 OCT images equally distributed along the length of the plaque, amounting to approximately 20 ROIs per plaque. The final number of ROIs drawn depends on the size and position of the tissue and the number of artefacts present on the areas of interest. See section 2.4.1 for detail on ROI drawing methodology. The pixel information within these ROIs was then processed using a custom Matlab code (see section 2.4.2). As with the previous two chapters, the metric of interest is the standard deviation (SD) of the mean pixel intensity within the ROIs. For each patient plaque, the SDs of the ROIs drawn in the caps were averaged and are presented in Figure 5-1 and Figure 5-2. Culprit plaques are represented by non-patterned plain bars and non-culprit plaques are represented by striped bars. The colours of the bar charts represent the treatment, with white charts on Figure 5-1 showing results from each of the 11 saline treated patients. And orange charts on Figure 5-2 showing results from each of the 8 USPIO treated patients. The datasets for each patient are normalised to the mean of all non-culprit plaques from saline treated patients.

5.3 Results

5.3.1 Patient plaques OCT image analysis

For each individual patient (both saline and USPIO treated), the culprit plaque mean SD is higher than the control non-culprit plaque mean SD but this difference is not always significant. Saline treated patients 1, 2, 3, 6, 7, 9, 10 and 11 (Figure 5-1) all have a significantly higher ($p<0.05$) OCT signal in their culprit plaques compared to their non-culprits whereas patients 4, 5 and 8 (Figure 5-1) do not have a significant difference. USPIO treated patients 1, 2 and 3 (Figure 5-2) all have a significantly higher ($p<0.05$) OCT signal in their culprit plaques compared to their non-culprits whereas patients 4, 5, 6 and 7 (Figure 5-2) do not have a significant difference. USPIO treated patient 8 unfortunately could not have a non-culprit plaque imaged for comparison. Therefore, 61% of patients in this study (11 out of 18) had a significant increase in OCT signal in the caps of ruptured culprit plaques compared to stable non-culprit plaques. This indicates that the standard deviation metric, although not perfect, is somewhat predictive of plaque severity. A number of factors could be affecting these

results, namely, small N numbers, systemic inflammation and variability in non-culprit plaque types. These factors will be explored further in the discussion section.

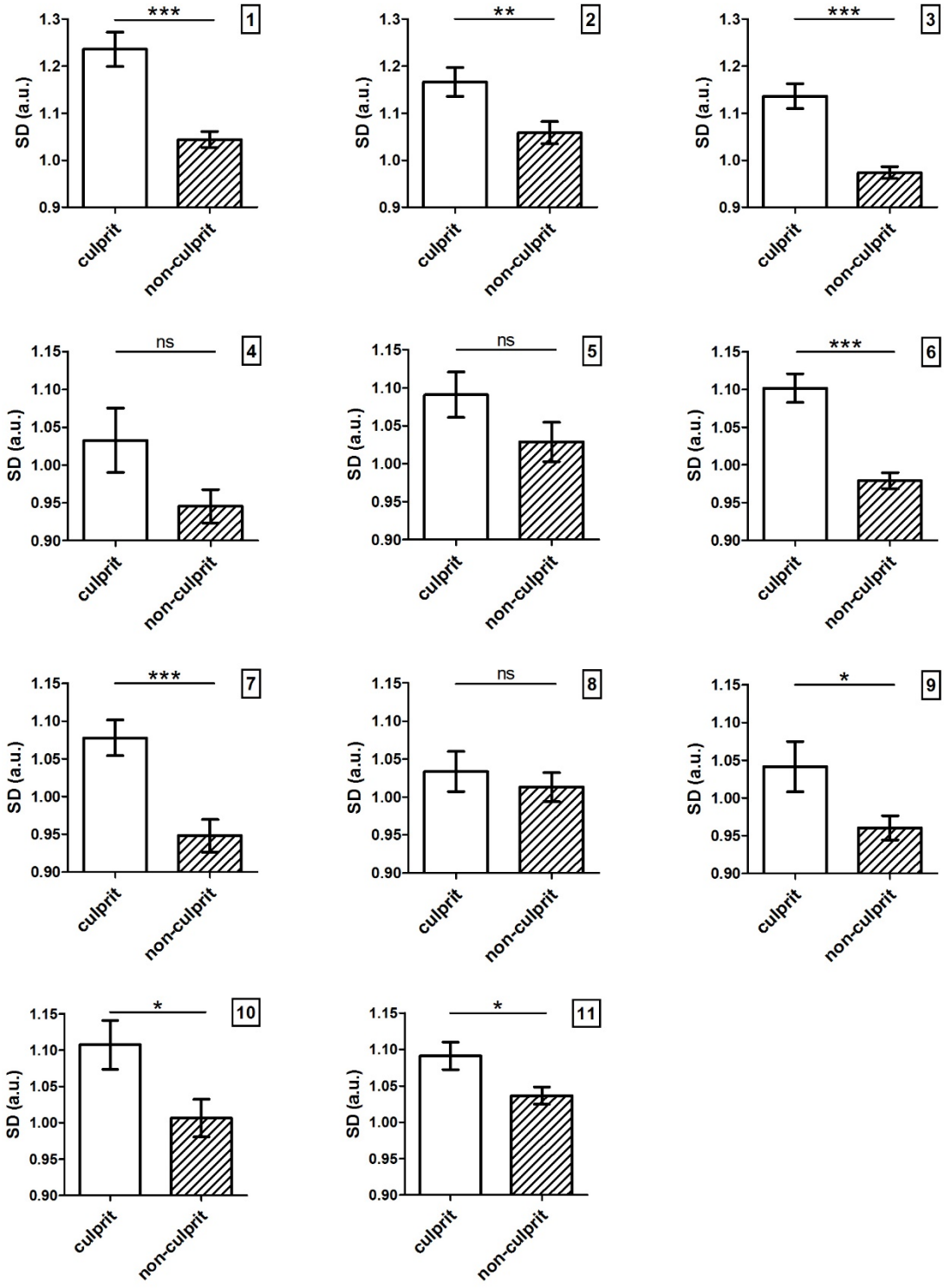

*Figure 5-1: Standard deviation of pixel intensity analysis of OCT images from saline treated control patients. Each plot shows the mean SD from ROIs of culprit versus non-culprit plaques of each patient. All values are normalised to mean of non-culprit plaques, ns= not significant, * p<0.05, ** p<0.01, *** p<0.001. Error bars = SEM.*

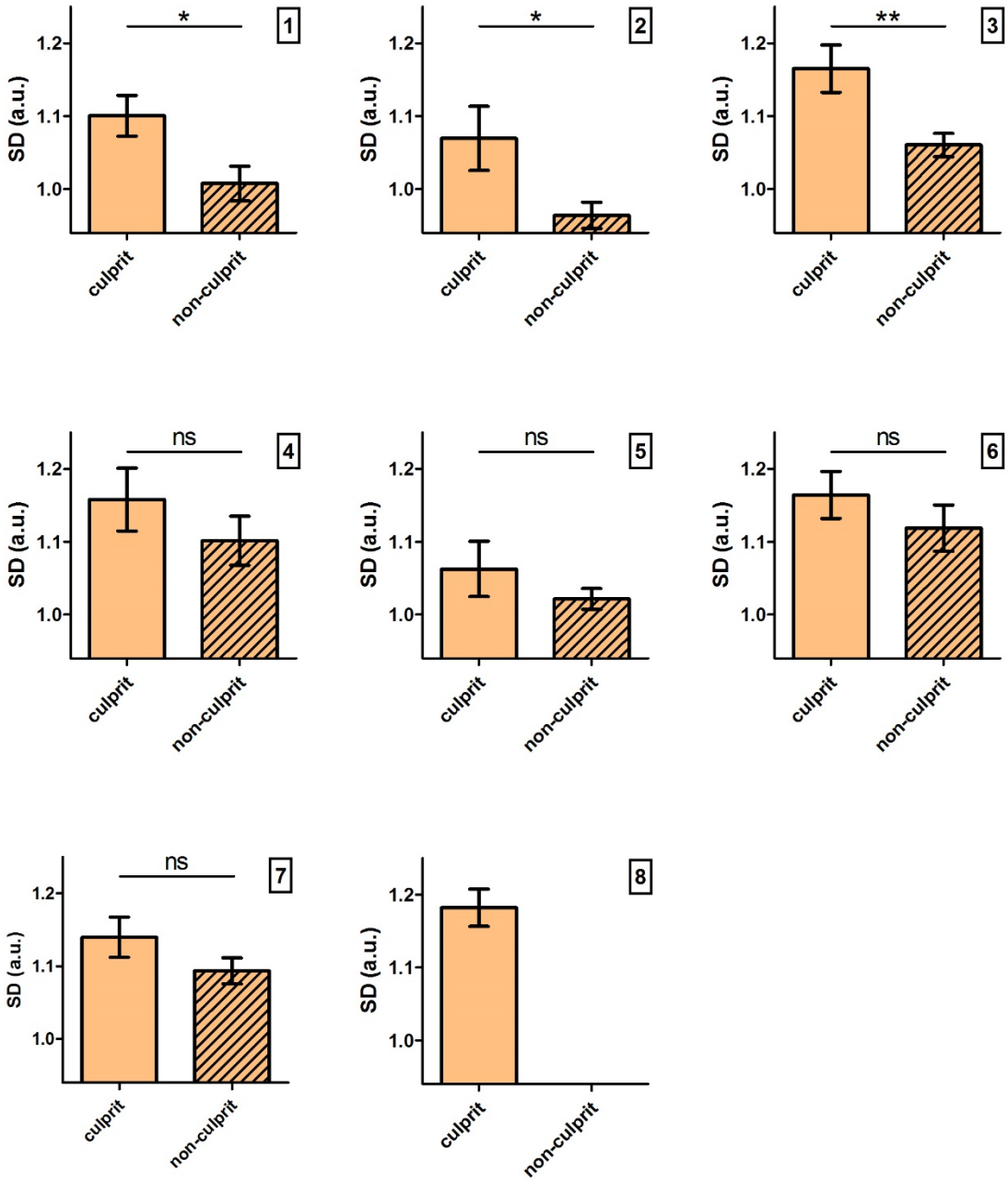

*Figure 5-2: Standard deviation of pixel intensity analysis of OCT images from USPIO treated patients. Each plot shows the mean SD from ROIs of culprit versus non-culprit plaques of each patient. All values are normalised to the mean of saline non-culprit plaques, ns= not significant, * p<0.05, ** p<0.01, *** p<0.001. Error bars = SEM.*

In order to compare the OCT signal enhancement efficacy of the two treatments (saline and USPIO) the data from the saline treated patients need to be pooled together and analysed against that of the USPIO treated patients, as is presented in Figure 5-3. This figure shows that the SD of the OCT images is greater in the culprit plaques of patients treated with USPIO compared to culprit plaques in patients treated with saline (1.132 vs 1.102 respectively,

p<0.05). Similarly, the SD was higher in non-culprit plaques of patients treated with USPIO compared to those administered saline (1.053 vs 1, p<0.001). In patients treated with USPIO, the SD was higher in the culprit plaque when compared to their non-culprit plaques (1.132 vs 1.053 respectively, p<0.001). Although lower than UPSIO patients, a difference in the SD signal in the culprit versus non-culprit plaques was observed for patients treated with saline (1.102 vs 1 respectively, p<0.001). These results indicate that when pooled together in this way, culprit plaques overall have significantly higher OCT signal in their caps compared to non-culprit plaques, regardless of treatment. Additionally, USPIO treatment significantly enhances the OCT signal in both culprit and non-culprit plaque caps.

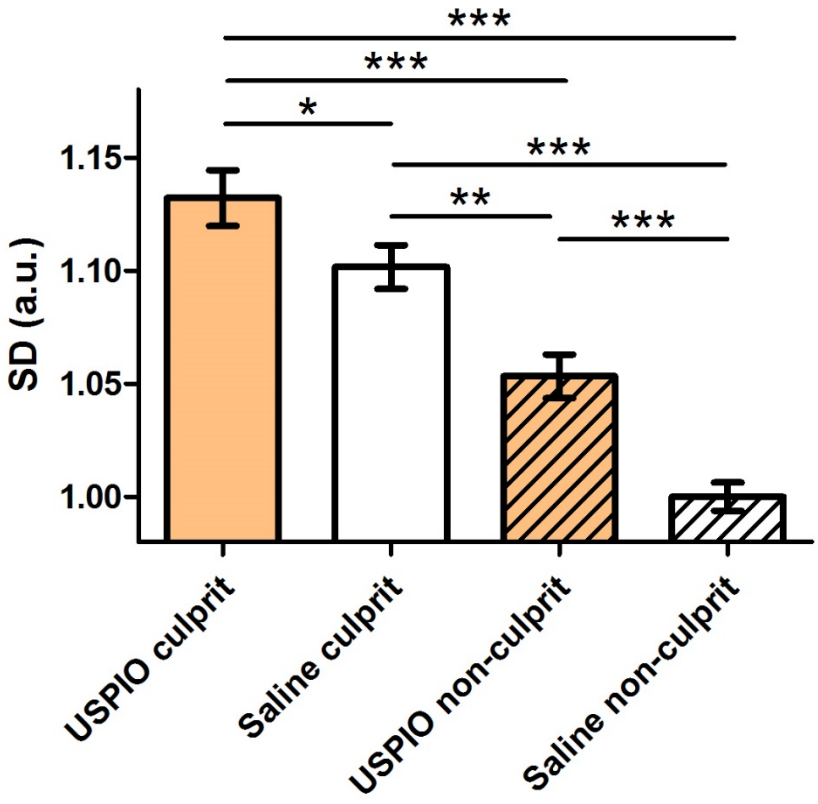

*Figure 5-3: Standard deviation of pixel intensity analysis of OCT images from all patients pooled together. All values are normalised to saline non-culprit mean, ns= not significant, * p<0.05, ** p<0.01, *** p<0.001. Error bars = SEM.*

5.3.2 SD hotspot visualisation tool

The SD results presented above showed that USPIO treatment of ACS patients can significantly increase the local SD of plaque OCT images compared to placebo treated patients. It would however be useful to be able to visualise these increased SD regions in

order to detect differences in plaque inflammation in real time in vivo. An SD hotspot visualisation tool was therefore developed in Matlab as described in section 2.4.3 and a selection of OCT images from the two treatment groups were processed.

Figure 5-4 shows an OCT image from each of the non-culprit plaques of saline treated patients 8, 9 and 11 with (right) and without (left) the SD hotspot overlay. Figure 5-5 shows an OCT image from each of the culprit plaques of saline treated patients 8, 9 and 11 with (right) and without (left) the SD hotspot overlay. Similarly, OCT images from non-culprit and culprit plaques of USPIO treated patients 1, 3 and 6 are presented in Figure 5-6 and Figure 5-7 respectively with (right) and without (left) the SD hotspot overlay. As with the murine study from the previous chapter, the raw OCT images of coronary plaques from ACS patients treated with USPIO or saline were not visually distinguishable from each other (left panels). Application of the SD hotspot mapping technique (right panels) yielded clear visual distinctions between the treatment groups and culprit versus non-culprit plaques. In particular, there were visually more high-intensity hotspots in the culprit plaques of patients treated with USPIOs (Figure 5-7) compared to their non-culprit plaques (Figure 5-6) and to both the culprit (Figure 5-5) and non-culprit plaques (Figure 5-4) of patients pre-treated with saline.

When looking at saline patients alone, both patients 9 and 11 have more hotspots in their culprit plaque (Figure 5-5) compared to their non-culprit (Figure 5-4) with patient 9 having a much starker difference. In contrast, saline patient 8 counter-intuitively has more hotspots in the non-culprit (Figure 5-4) compared to the culprit (Figure 5-5). However, in USPIO treated patients, the difference between culprit and non-culprit plaques is much clearer; each individual patient (1,3 and 6) has a much higher density of higher intensity (more orange/red) hotspots in the culprit plaques (Figure 5-7) than the non-culprit plaques (Figure 5-6). These visual differences are concurrent with the quantitative results obtained in the previous section; USPIO markedly increases the OCT contrast of the caps of inflamed plaques having recently ruptured.

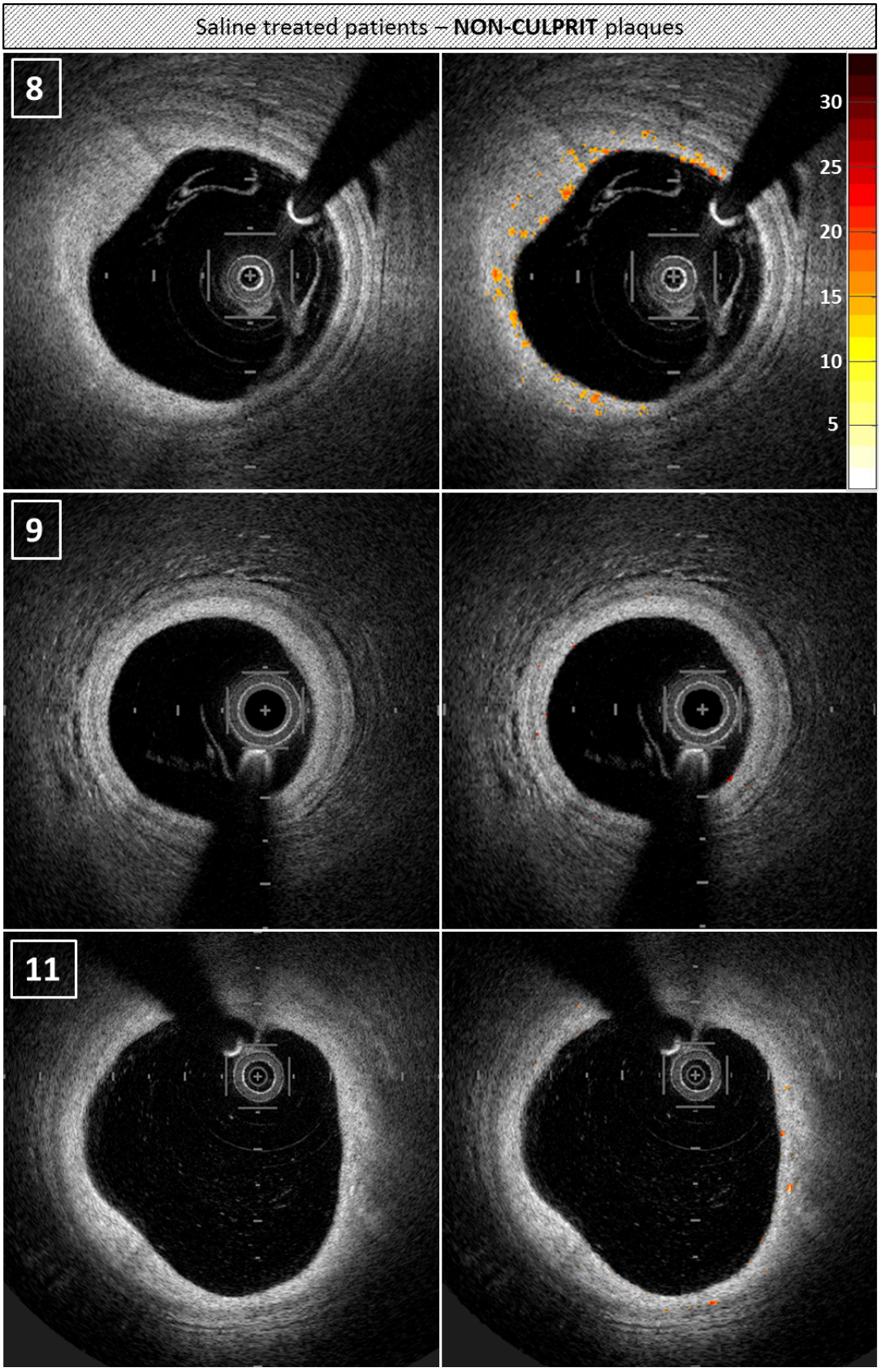

Figure 5-4: OCT slices through non-culprit plaques of saline treated patients 8, 9 and 11 with a colour map overlay of areas of high SD on the right (colour scale applies to all images).

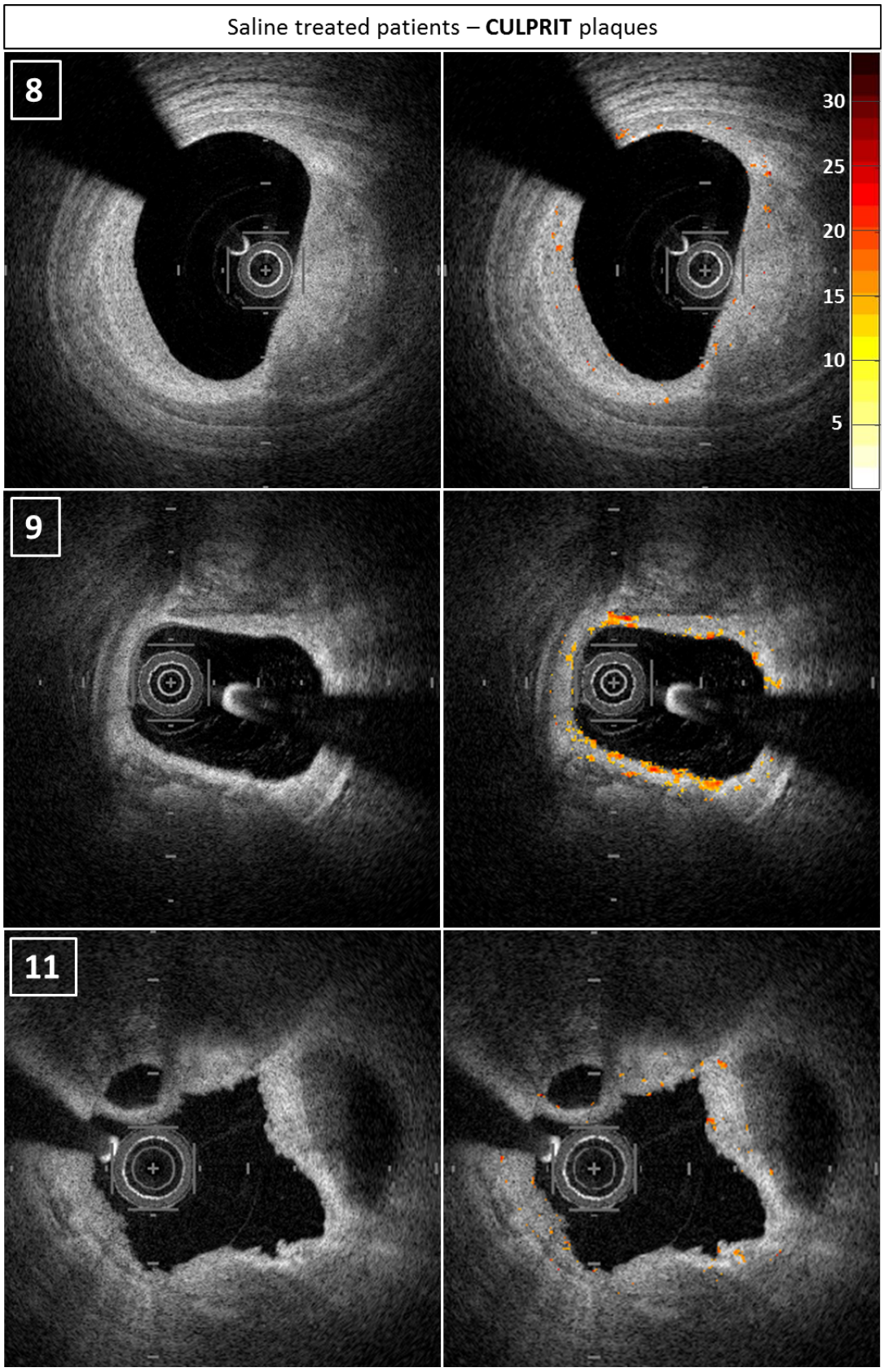

Figure 5-5: OCT slices through culprit plaques of saline treated patients 8, 9 and 11 with a colour map overlay of areas of high SD on the right (colour scale applies to all images).

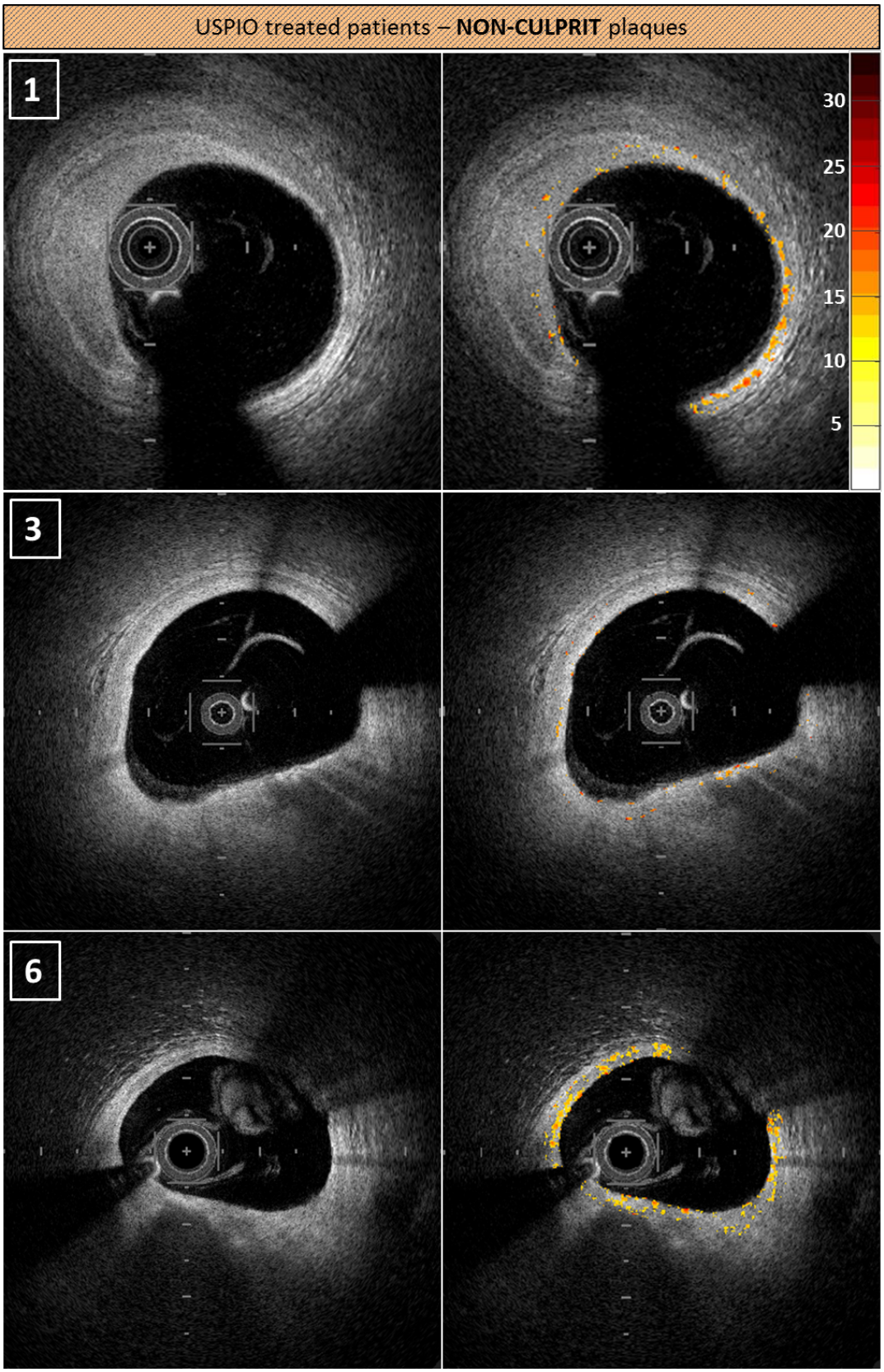

Figure 5-6: OCT slices through non-culprit plaques of USPIO treated patients 1, 3 and 6 with a colour map overlay of areas of high SD on the right (colour scale applies to all images).

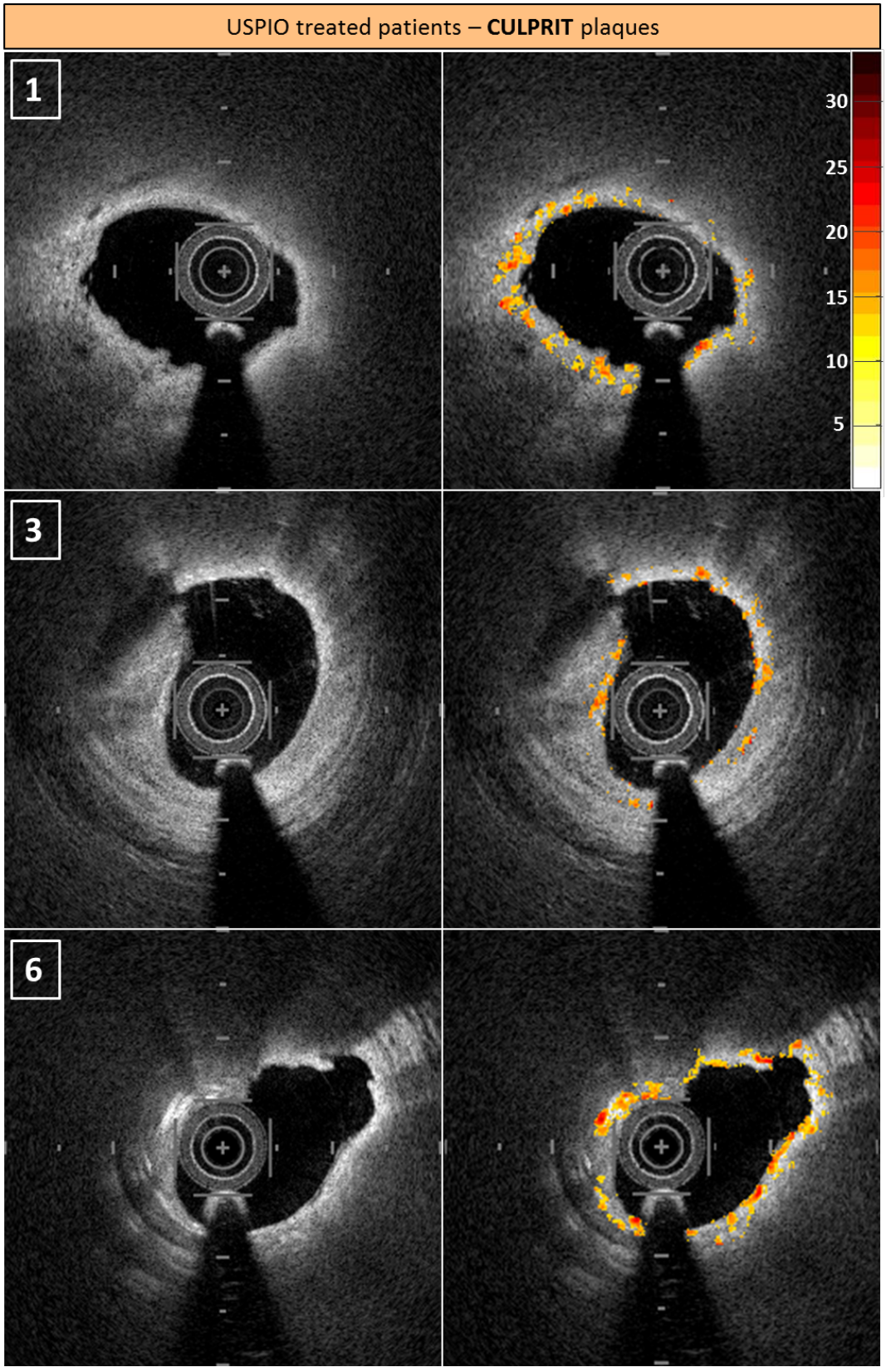

Figure 5-7: OCT slices through culprit plaques of USPIO treated patients 1, 3 and 6 with a colour map overlay of areas of high SD on the right (colour scale applies to all images).

5.4 DISCUSSION

To summarize, in this chapter IV-OCT imaging of ACS patient culprit and non-culprit plaques was performed with and without pre-treatment with USPIO particles. Image analysis methodologies presented in the previous chapters were employed here and there were three main outcomes. The first is that the caps of culprit plaques yielded significantly higher OCT contrast compared to non-culprit plaques regardless of treatment. Secondly, USPIO treatment was found to significantly increase the OCT signal in plaque caps compared to the plaque caps of saline treated patients. And finally, the SD hotspot tool presented in the previous chapters was implemented in the images of human plaques and found to support the quantitative results obtained. These three outcomes will be discussed in more detail subsequently.

Firstly, section 5.3.1 presented the SD image analysis results from the IV-OCT imaging of 19 ACS patients. When the data from all patients was pooled together (Figure 5-3) culprit plaques were found to have significantly higher OCT signal compared to non-culprits in both treatment groups, confirming **hypothesis 1** of this chapter. Some overlap in these values in individual patients were observed, in part this is because non-culprit plaques in ACS patients are an imperfect control. Indeed, atherosclerosis is a systemic disease process so the inflammation that can trigger an event is frequently observed in numerous plaques across the coronary and systemic vasculature. Additionally, although the non-culprit plaques were in a remote vessel and were selected for their relatively stable appearance, there could be any number of plaque subtypes in this "non-culprit" cohort. This variability in plaque type/structure/composition will affect the macrophage burden and therefore the SD value in the caps. Indeed, MacNeill et al. found no significant difference between the NSDs of culprit and non-culprit plaques of ACS patients[92]. It would be interesting to clinically grade the non-culprit plaques based on their OCT appearance and then investigate plaque type correlation with SD values but this was beyond the scope of this translational study.

The second main message emerging from the image analysis results (section 5.3.1) relates to the effect of USPIO treatment on OCT signal. From the results of Figure 5-3 it was shown that the caps of the culprit plaques of USPIO treated patients had significantly higher OCT signal than those of saline treated patients, confirming **hypothesis 2** of this chapter. The non-culprit plaques of USPIO patients also showed significantly higher OCT signal compared to the non-culprits of saline patients, again showing that USPIO serves to enhance the detection of

systemic inflammation and macrophage infiltration observed throughout the coronary vasculature at the time of ACS. This is the first time that any OCT contrast agent has been tested in humans, making this a truly novel translational study. Although histological validation in human coronary atheroma is not feasible, thanks to the proof-of-concept studies in the previous chapters showing that USPIOs enhance the SD associated with macrophages in vitro and in $ApoE^{-/-}$ mouse plaques we can be reasonably confident that these increased SD values in the USPIO treated patients are due to their accumulation in plaque macrophages. This is the very first time that USPIOs have been used in vivo as an OCT contrast agent to enhance the detection of plaque inflammation.

Finally, section 5.3.2 presented a bespoke OCT SD hotspot visualisation tool which accurately represented the quantitative results obtained previously. Indeed, there were more high intensity hotspots in the caps of the culprit plaques compared to those of non-culprit plaques and this difference was more marked in USPIO treated patients compared to saline control, confirming **hypothesis 3** of this chapter. Although the appearance of these hotspot maps varied a lot between different OCT slices, the technique is an appealing intuitive tool which could be implemented in real-time IV-OCT imaging to aid cardiologist in assessing plaque inflammation and using this information to guide their intervention.

There are several limitations to the work of this chapter. Firstly, due to errors in blinded treatment assignment the study ended up with two more patients in the saline treated group (11) than the USPIO treated group (8). Additionally, for one of the 8 USPIO treated patients the non-culprit plaque imaged had to be removed from analysis due to poor image quality. These factors make for a relatively small group of experimental treatment patients which does reduce the power of the study and shows that larger confirmatory studies are required. Additionally, the required manual ROI drawing step involved in the image analysis is a significant limitation. Because of the time-consuming nature of drawing ROIs in the fibrous caps of plaques, this was only done on 8 images for each plaque (equally distributed along the full length of the plaque). It would of course be better to include all the images of the plaques in the analysis (as was done for the in vitro phantoms and the mouse plaques in previous chapters) but this would involve too high of a time commitment for a cardiology expert to commit to. All of the OCT macrophage quantification studies to date also involved an ROI drawing step in order to restrict the image analysis to the fibrous cap and all in fact analysed fewer images per plaque (maximum 3)[89,92,139,140] than we did here. ROI drawing was

also a necessary step in the SD hotspot tool implementation, demonstrating that this tool is not quite ready for real-time assessment of plaque inflammation.

In conclusion, this novel in vivo human study has further confirmed previous findings that the local OCT standard deviation of pixel intensity in plaque caps accurately detects macrophage burden. For the first time, using this metric, it was shown that the caps of culprit plaques of ACS patients have significantly higher OCT signal than non-culprit plaques of the same patients. Additionally for the first time, USPIO particles were used as an IV-OCT contrast agent to enhance the detectability of plaque macrophages in vivo. This OCT signal enhancement was effectively visualised using a novel standard deviation of pixel intensity hotspot tool which presented an attractive view to the future of real-time inflammation visualisation with OCT in vivo. This was the final chapter of the 3 part translational USPIO-OCT study demonstrating USPIO as an effective OCT contrast agent for macrophage detection. The following chapter is a perspective study looking even further into the future, making first steps towards developing brand new OCT and macrophage specific imaging agents: lanthanide-doped nanoparticles.

6 CHAPTER SIX: NOVEL OCT CONTRAST AGENTS FOR MACROPHAGE DETECTION

6.1 INTRODUCTION

The previous three chapters investigated USPIO (an already clinically approved particle) as a new IV-OCT contrast agent in vitro, in a murine model and in man. In so doing we have established a robust framework for the screening of potential new IV-OCT contrast agents. In this chapter we utilise this framework to test and optimise a panel of novel lanthanide-doped upconversion nanoparticles for their ability to enhance macrophage detectability with IV-OCT in vitro.

As presented in section 1.5 there have been very few studies investigating the IV-OCT signal enhancement properties of new agents, with most of the focus being on different forms of gold nanoparticles[126–129] and just one study investigating quantum dots[130]. Although most of these studies have shown the particles to significantly enhance IV-OCT contrast, there is a lot of room for discovery of new, more specific particles. Importantly, none of the studies mentioned investigated the toxicity of their particles or their IV-OCT properties when actually loaded into cells. Additionally, their assessments of OCT contrast enhancement were varied but none used techniques that can be implemented on human atherosclerotic plaque imaging in vivo. The work in chapter 3 showed that we have developed a robust phantom model and image analysis methodology which is highly translatable and allows easy, standardised and reproducible screening of imaging agents with IV-OCT. This makes us perfectly placed to test new contrast agents.

Although USPIOs are very attractive potential OCT contrast agent, given their clinical approval and their proven accumulation in atherosclerotic plaques, there were some limitations to this choice of nanoparticle. Firstly, they are not entirely specific to macrophages, it is possible that they could be taken up by other cells in atheromatous plaques. Additionally, although their scattering properties were shown to be high enough for detection by IV-OCT (when packaged into cells), this is not what they were designed and optimised for, it should be possible to design bespoke contrast agents with even higher, more specific IV-OCT signal enhancement. In this chapter we propose to start anew, with particles that are tuneable in all aspects: OCT detectability, macrophage specificity and dual modality imaging potential.

With this in mind, we partnered with the world leaders in the field of upconversion nanoparticles: Prof Xiaogang Liu's lab group at the National University of Singapore. They design and produce lanthanide doped nanocrystals for many applications, as described in the

review by Lui et al.[142]. This process involves incorporating lanthanide ions into host lattices in order to fine tune many of their defining characteristics: electric properties, magnetism and light absorption and emission properties[142–144]. In this way, nanoparticles can be designed which absorb light at one wavelength and emit it at a different wavelength; an extremely attractive quality for fluorescence imaging[142–144]. The magnetism of the particles can also be modulated for use with MRI and their optical scattering properties can be tuned by changing the nanocrystal structure[142–144], making them interesting potential OCT contrast agents.

For the purposes of this IV-OCT study, Zhigao Yi from Prof Xiaogang Liu's group, designed and produced a panel of different lanthanide doped upconversion nanoparticles which can absorb a small percentage of the light emitted by the IV-OCT laser and re-emit it at different wavelengths. This makes them ideal candidates for dual OCT and fluorescence imaging studies, similar to that published with quantum dots[130]. This upconversion property would also be an extremely useful tool when it comes to functionalising the particles for use in actually tagging specific sub-types of macrophages such as highly pro-inflammatory plaque macrophage profiles. Indeed, the fluorescent properties would be essential to in-vitro flow cytometry and confocal microscopy assays necessary for investigating macrophage tagging. The purposes of this chapter however were to perform preliminary IV-OCT screens to start to assess and fine tune the OCT contrast enhancement properties of the particles before moving onto functionalising them at a later date.

Initially, 9 lanthanide particles of either fluoride or carbonate structure were screened (section 6.3.1) in order to select the one with the highest OCT contrast: Gd-carbonate. This particle was subsequently coated in 3 different ways and these new coated particles were further tested for biocompatibility as well as their OCT and MRI contrast properties (section 6.3.2). The three aims and three associated hypotheses of this chapter are outlined below.

AIM 1 (section 6.3.1): To successfully screen a panel of new IV-OCT contrast agents with the previously established phantom methods in order to identify particles with high OCT detectability.

Hypothesis 1: The phantom mould and methodologies developed previously will enable us to quickly screen many nanoparticles and identify ones with highest OCT contrast potential.

AIM 2 (section 6.3.2.1 and 6.3.2.2): To determine the OCT contrast capabilities and the cytotoxicity of the selected particle (Gd) after it has been coated for biocompatibility.

Hypothesis 2: The particle selected (Gd) to take into cell experiments will still produce high OCT contrast when coated for biocompatibility and will not be significantly cytotoxic to the cell line used here.

AIM 3 (sections 6.3.2.3 and 6.3.2.4): To determine if the coated Gd particles loaded into macrophages can enhance their OCT signal and retain MRI contrast capabilities.

Hypothesis 3: When loaded into cells, the coated Gd based particles significantly increased the OCT signal of the cells and they retain their MRI capabilities

6.2 METHODS

6.2.1 Particle design and production

All the nano-particles used in this chapter were designed and produced by Zhigao Yi from Prof Xiaogang Liu's group at the National University of Singapore. These upconversion lanthanide doped nanoparticles were designed with an absorption band in the excitation range of the clinical OCT system (1300 nm). This means that they can absorb a percentage of the light emitted by the OCT system and they can then re-emit this light at a different wavelength (e.g. visible), making them agents capable of dual modality imaging. They were made with either a carbonate or fluoride structure doped with different lanthanide ions: Ytterbium (Yb), Erbium (Er), Neodymium (Nd), Dysprosium (Dy) and Gadolinium (Gd). Initially, the 9 nanoparticles received were the following: $Yb(OH)CO_3$, $Er(OH)CO_3$, $Nd(OH)CO_3$, $Dy(OH)CO_3$, $Gd(OH)CO_3$, $NaYbF_4$, $NaErF_4$, $NaNdF_4$, $NaDyF_4$. The average sizes of the carbonate particles, based on TEM imaging, were respectively: 67 nm, 80 nm, 640 nm (rod-shaped), 313 nm, 188 nm. The fluoride particles were all an average of 15-25nm in size. Following preliminary testing, solely the $Gd(OH)CO_3$ particle was selected and coated by Yi Zhigao to improve bio-compatibility, this is referred to subsequently as the Gd particle. Three new batches of this particle were produced, each coated with either polyacrylic acid (PAA), polyethylene glycol (PEG) or polyethyleneimine (PEI).

6.2.2 Cell viability assays

To measure the biocompatibility of the differently coated Gd particles described above, MTT assays were performed using the TACS® MTT cell proliferation kit from Trevigen. This colorimetric assay is NADPH dependent and is widely used for the measurement of cell metabolic activity. The RAW264.7 murine macrophage cell line was cultured as described in section 2.1. In a 96-well plate, approximately 20 million RAW cells per well were incubated with each of the 3 differently coated particles (Gd-PAA, Gd-PEG and Gd-PEI) at 1mM concentration in media. 4 well repeats were plated for each condition, including positive controls with media only and negative controls with 30% dimethyl sulfoxide (DMSO) in media. The incubations were performed for 2 and 20 hours in a 37˚C incubator. Following incubation, the wells were washed twice with DPBS and then incubated with 110 µl of a 10% solution of MTT reagent 1 in media. This incubation was performed for 4 hours in a 37˚C incubator, after which a dark purple precipitate could be observed inside the cells under a compound microscope. 100 µl of MTT reagent 2 was subsequently added to each well and

incubated in the dark at room temperature overnight. Finally the absorbances were read on a Bioteck Synergy spectrophotometer at 570 nm and 650 nm (for background absorbance) after shaking for 2mins. The background absorbance readings (at 650 nm) were subtracted from the sample readings (at 570 nm), the 4 repeat wells were averaged for each condition and this was normalised to the positive control mean. This experiment was repeated 4 times for both the 2 and 20 hour particle incubation time points, and the cell viability results are presented in section 6.3.2.2.

6.2.3 Preliminary OCT screenings in water

The 9 uncoated lanthanide particles described in section 6.2.1 (5 carbonates and 4 fluorides) were initially OCT screened in order to determine which ones had the best signal enhancement potential. This was done using the 3-D printed phantom mould described in section 2.3. The sections of the phantom mould were filled with 250 µl of the different particle solutions diluted to 100 mM in distilled water. These were imaged (as well as a water only control) using the Dragonfly™ OPTIS™ OCT catheter and St. Jude Medical OTPIS integrated system.

6.2.4 Agarose phantoms

A simple phantom was made using 1.5% agarose in PBS and each of the 4 different carbonate-lanthanide particles (Dy, Nd, Y and Gd) at final concentrations of 100 mM in different sections of the phantom. The gels were made by combining 300 µl of particle stock solutions (200 mM) with 300 µl of melted agarose. A control gel was also made by combining 300 µl of PBS with 300 µl of melted agarose. Each was thoroughly mixed (while kept warm) to ensure homogenous distribution of the particles in the gel and they were transferred to separate sections of the phantom mould. A second simple phantom was made with the same particles at final concentrations of 10 mM by combining 60 µl of the particle stock solutions (200 mM) with 540 µl of melted agarose. The control gel was made by combining 60µl of PBS with 540 µl of melted agarose. Each was thoroughly mixed (while kept warm) to ensure homogenous distribution of the particles in the gel and they were transferred to separate sections of the phantom mould.

A third simple phantom was made with the 3 differently coated Gd-carbonate particles at 1mM final concentrations in the following way:

- No particle control: 500 µl melted agarose

- 1 mM Gd-PAA: 1.7 µl of Gd-PAA stock (300 mM) and 500 µl melted agarose
- 1 mM Gd-PEG: 1.7 µl of Gd-PEG stock (300 mM) and 500 µl melted agarose
- 1 mM Gd-PEI: 2.5 µl of Gd-PEI stock (200 mM) and 500 µl melted agarose

Each was thoroughly mixed (while kept warm) to ensure homogenous distribution of the particles in the gel and they were transferred to separate sections of the phantom mould.

Additionally, 3 identical macrophage laden phantoms were made. For this, the RAW264.7 murine macrophage cell line was cultured as described in section 2.1 in three separate T162 flasks and each incubated with 67 µl of one of the 3 coated Gd-carbonate particles (Gd-PAA, Gd-PEG and Gd-PEI from 300 mM stock solutions) in a total of 20 ml of media (final concentration of 1mM) for 24 hours. Following washing in Dulbeco's PBS (Gibco), lifting by scraping and counting with a haemocytometer, $20x10^6$ cells were taken from each treatment condition. These were washed, pelleted and fixed in 1ml of 4% PFA for 15 minutes then pelleted again and the supernatant removed. These pellets were warmed up in a water bath then thoroughly mixed with 0.5ml of warm 1.5% agarose using a warmed pipette tip (to avoid setting prematurely) before transferring to the phantom mould.

All these phantoms were made with the 1mm rod insert in place to create a "lumen" through the agarose gel phantom. This rod was removed in order to insert the Dragonfly™ OPTIS™ OCT catheter and image using the St. Jude Medical OTPIS integrated system. Image analysis was performed using the custom methods and software described in section 2.4.

6.2.5 MRI imaging

The third "simple phantom" made with the coated Gd-carbonate particles, as well as one of the "macrophage phantoms" were imaged by Dr. M.A. Jansen at Edinburgh Preclinical Imaging (BHF Centre for Cardiovascular Science). The individual agarose gel cubes were taken out of the phantom mould sections and each placed in wells of a 24-well plate.

MRI of these phantom cubes was performed on a 7 T horizontal bore Biospec AVANCE neo preclinical imaging system equipped with a 116 mm bore gradient insert (Bruker BioSpin GmbH, Germany, maximum gradient strength 660 mT/m). A 86 mm quadrature volume coil (Bruker BioSpin GmbH, Germany) was used for signal transmission and reception. Scout images were taken to confirm correct positioning and the magnetic field was optimised using an automated shimming routine. For all subsequent sequences, the field of view was 80 × 60 mm, matrix size 200 × 150 and slice thickness 2.0 mm. For T2 mapping, 1 horizontal slice

through the centre of the phantoms was acquired using a Multi-Slice-Multi-Echo sequence with the following parameters: TR 2200 ms, 14 images with echo time varying from 14 – 98 ms, number of signal averages 4. The scan time was 22 min. T1 maps were acquired of the same slice as for T2 mapping using a Rapid Acquisition with Relaxation Enhancement (RARE) sequence with the following parameters: TR 200, 500, 1200, 2500, 5000, and 10000 ms, TE 6 ms, RARE factor 2, number of signal averages 3. The scan time was 35 min. T1 and T2 maps were generated in Paravision 360 using built-in fitting routines, they are presented in section 6.3.2.4.

6.3 RESULTS

6.3.1 Preliminary OCT screening of nine lanthanide particles

To determine the potential of the lanthanide particles for OCT contrast enhancement a screening was done with each of the particles diluted to 100 mM in distilled water, using water alone as a control. These solutions were imaged in the chambers of the 3D printed phantom mould described in section 2.3 in order to use the IV-OCT imaging catheter. Figure 6-1 shows representative OCT images of each sample particle and one of the water only control. The chambers of the phantom mould were half filled with the particle solutions which results in the images being roughly half dark (representing the air half of the chamber) and half bright and speckled (representing the sample half of the chamber) with an air-liquid (AL) interface which appears as a bright line draped over the catheter artefact. However, in the water only control image, the sample and air halves of the image look almost identical and the AL interface is barely visible, since water is transparent at this wavelength. The fluoride Er, Nd and Dy particles have in comparison, a much brighter AL interface but their sample portion of the image is only slightly brighter than that of the air and water control.

However, the fluoride Yb particle as well as each of the carbonates (Yb, Er, Nd, Dy and Gd) have very bright OCT images, suggesting that they are potential good contrast agents for OCT imaging. When comparing these 6 brighter particles, the Nd carbonate image stands out as containing many more bright dots which could be a sign of being a stronger contrast agent but could also suggest that it is less soluble in water and more prone to aggregation. The Gd and Dy carbonates stand out as having the brightest images of the 10 presented here. Following this initial simple screening, the 5 carbonate particles were selected to carry out more robust screenings. Due to a technical issue the Er carbonate could not be included in further work.

Two agarose phantoms containing the 4 remaining carbonate particles (Yb, Nd, Dy, Gd) at concentrations of 10 and 100mM were therefore made as described in section 6.2.4. Representative OCT images of each section of the 100mM phantom are shown in Figure 6-2. The images corresponding to the particle laden gels look clearly different to the agarose control, with a lot of large bright speckles present throughout the image which are absent in the control. Between each other, the different particle images look very similar, however, it does seem that Yb and Gd cause a reduced depth penetration of the signal (the image is dark towards the edges) and the Gd image looks to have the brightest speckles.

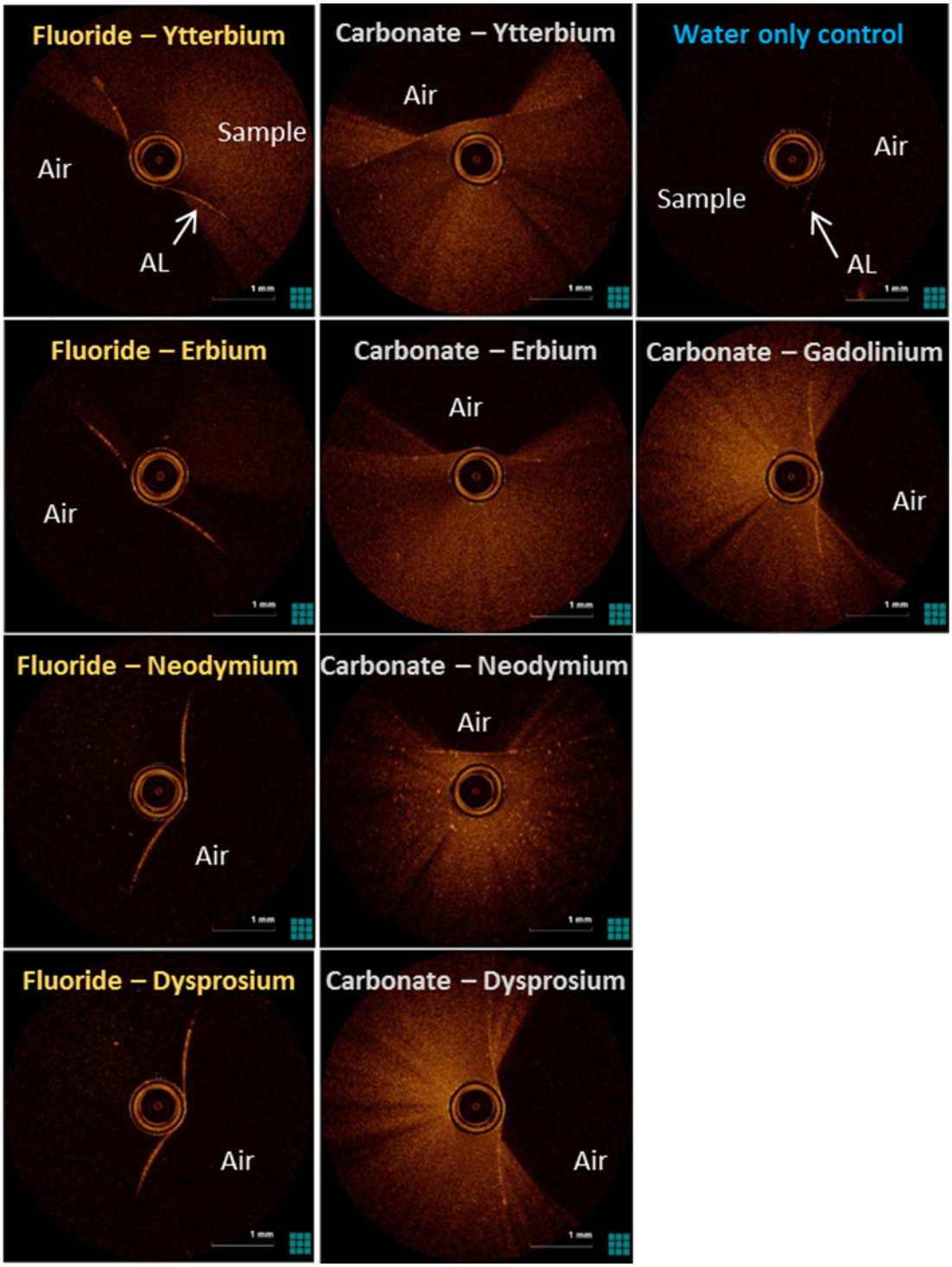

Figure 6-1: Initial OCT screening of 9 different Lanthanide based nanoparticles with either a fluoride or carbonate structure. All particle solutions were diluted to 100 mM in distilled water and imaged as such in the 3D-printed phantom mould. The images show approximately half the content of the mould section to be air (dark) and half to be the sample solution with usually a bright air-liquid (AL) interface in between.

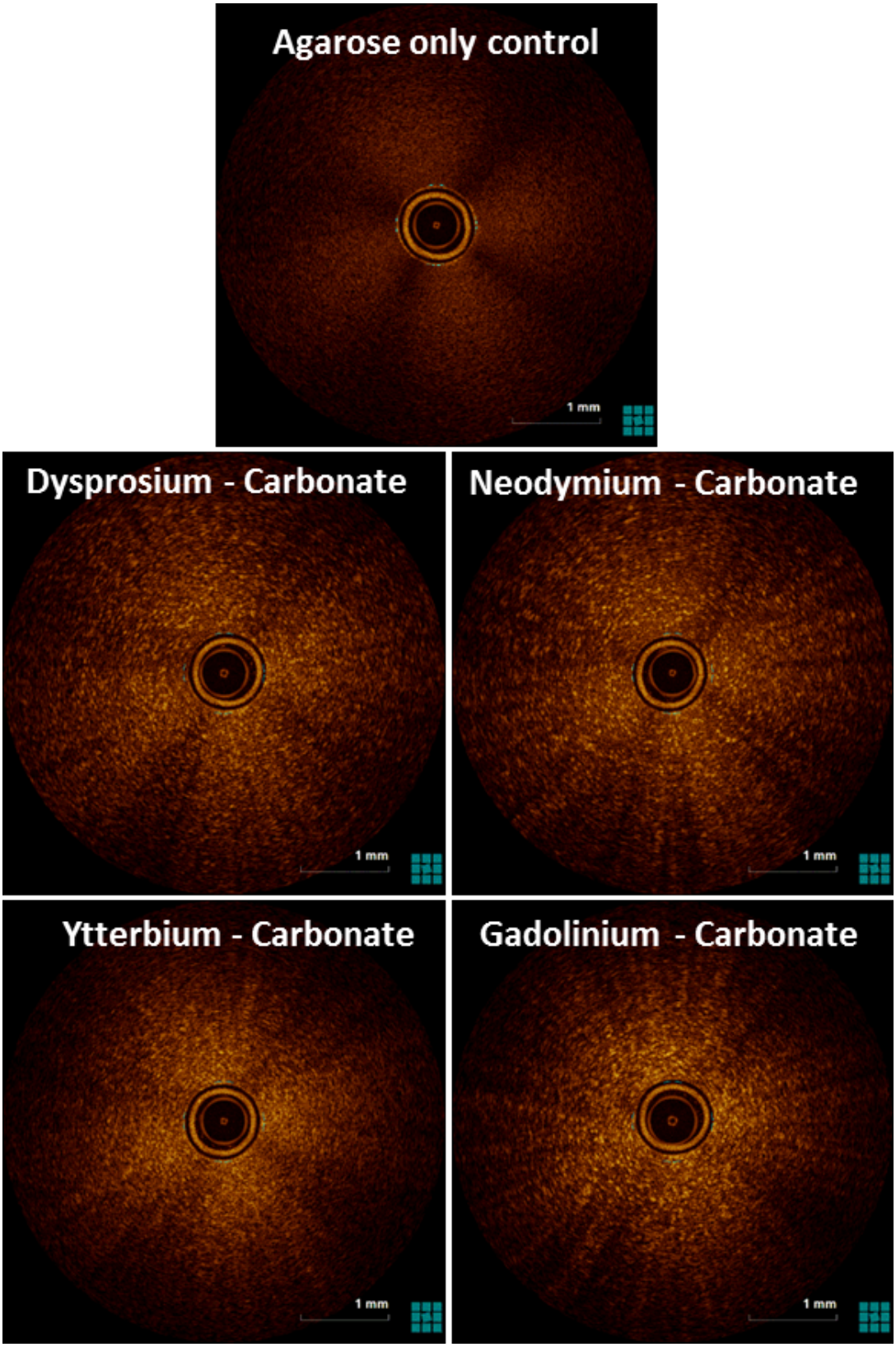

Figure 6-2: OCT imaging of an agarose phantom made with 4 different lanthanide carbonate nanoparticles. Each section of the phantom was made up of 1.5% agarose mixed with the stated particle at 100mM final concentration. One representative OCT slice for each particle gel and the agarose only control are shown.

As explained and demonstrated in previous chapters, the standard deviation (SD) of the mean pixel intensity within certain regions of the OCT images was used as a metric of the "granularity" to measure the effects of the different phantom compositions. In order to avoid imaging artefacts, ROIs were drawn on each of the OCT slices and the SD values for each ROI were processed in Matlab as described in methods section 2.4. Figure 6-3, presents the mean of these SD values for each section of the two "simple" phantoms laden with lanthanide-carbonate particles (Dy, Nd, Y, Gd) at concentrations of 100mM (phantom introduced in Figure 6-2) and 10mM. The image analysis results of the 100mM phantom do corroborate the qualitative assessment of the OCT images presented previously. Indeed, each of the nanoparticles tested (at both 100 and 10mM) led to a significantly higher mean standard deviation of pixel intensity (MSD) within the OCT images compared to the agarose only control images. Furthermore, at 100mM the Gd particle gave a significantly higher OCT contrast compared to each of the 3 other lanthanide carbonates. In the case of the 10mM phantom, both Y and Gd particles show significantly higher MSDs than Dy and Nd with Y itself being significantly higher than Gd.

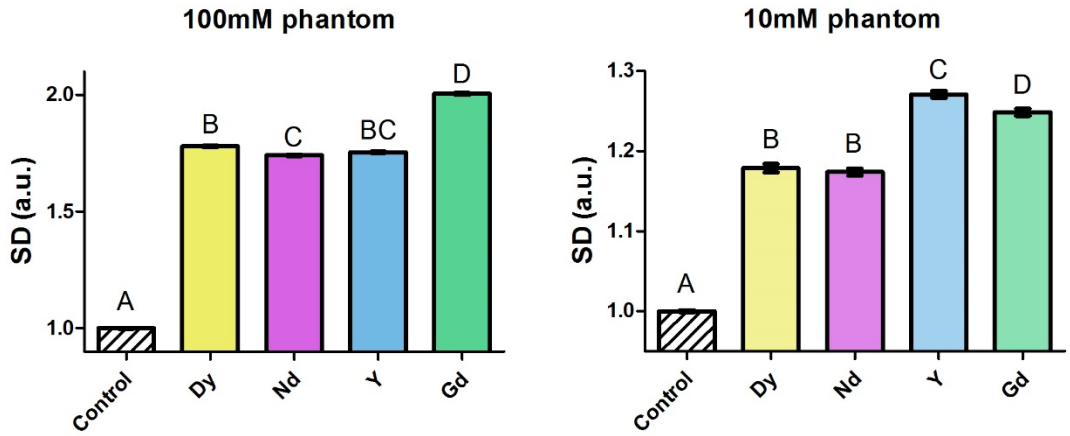

Figure 6-3: Standard deviation of pixel intensity analysis of OCT images from 2 phantoms made with 1.5% agarose and 4 different lanthanide carbonate particles. All values normalised to the agarose only control. Letters show results of statistical test, when two bars share the same letter they are not significantly different whereas different letters indicate significant difference ($p<0.05$). Error bars = SEM.

6.3.2 Comparison of 3 differently coated Gd-carbonate particles

From the results presented in the previous section it was clear that all the lanthanide carbonate particles were able to effectively increase the OCT signal. Of the 4 particles tested, the Gd and Y based ones were found to have the highest effect and due to its multi-modal capabilities (and previous approval for use in humans)[145] Gd was selected to move forward with the OCT study. In order to commence work with cells, the Gd-carbonate particle was produced with 3 different coatings: polyacrylic acid (PAA), polyethylene glycol (PEG) and polyethyleneimine (PEI). The three new particles, Gd-PAA, Gd-PEG and Gd-PEI were subsequently tested for OCT signal enhancement on their own in simple phantoms (section 6.3.2.1). Then they were tested for biocompatibility with RAW macrophages (section 6.3.2.2) before being used in macrophage phantoms to determine whether they retain their OCT contrast properties when packaged inside cells (section 6.3.2.3). Lastly, their MRI imaging potential was determined (section 6.3.2.4).

6.3.2.1 OCT testing particles alone

Similarly to section 6.3.1, a simple phantom was made with the differently coated Gd-carbonate particles (Gd-PAA, Gd-PEG, Gd-PEI) embedded in separate agarose sections at final concentrations of 1mM. This was done in order to verify that the coatings do not have a detrimental effect on the OCT signal enhancement and also to test the efficacy of the particles at a concentration more suitable for use with cells. Representative images of each section of the simple phantom are shown in Figure 6-4. The images corresponding to the particle-laden gels look very similar to the agarose only control aside from being overall slightly brighter and having a few bright speckles. Indeed, the Gd-PAA, Gd-PEG and Gd-PEI images have some bright specks whereas the control image has none. When comparing between the different particle images it seems that Gd-PEI has the most bright speckles which could mean that it has the highest OCT contrast or that it aggregates more than the other two.

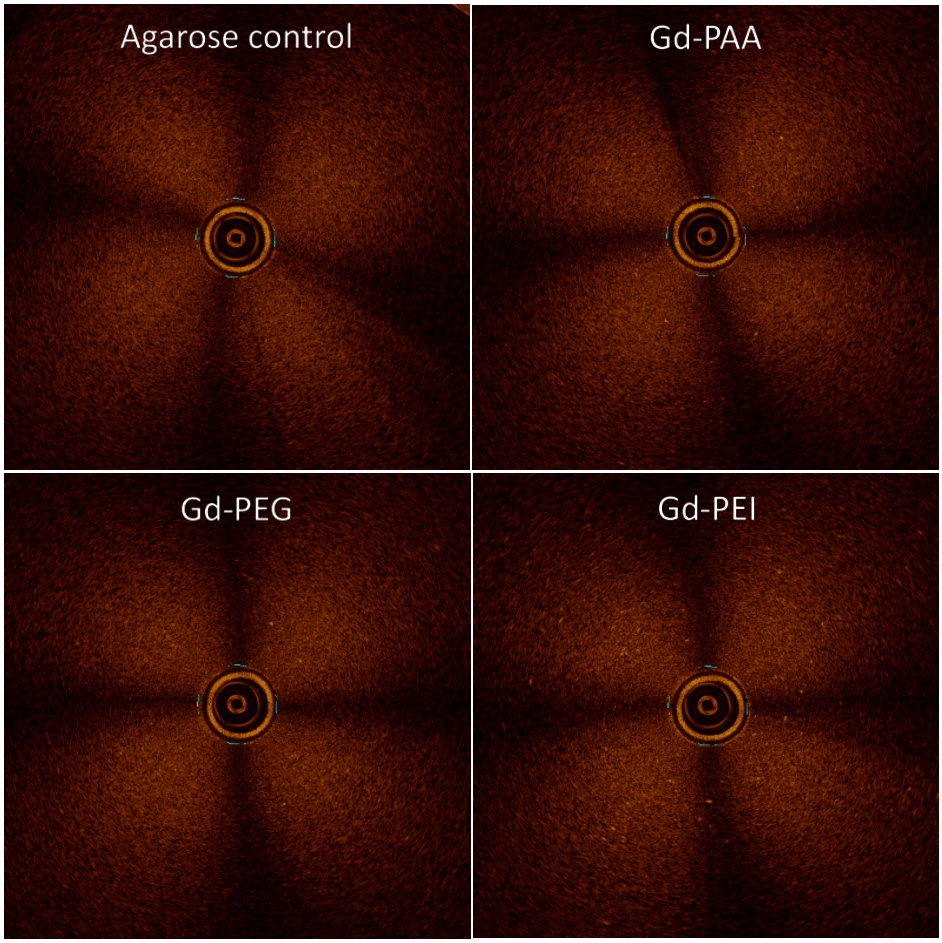

Figure 6-4: OCT images of an agarose phantom made with 3 differently coated (PAA, PEG and PEI) Gd-carbonate particles. Each section of the phantom was made up of 1.5% agarose mixed with the stated particle at 1mM final concentration. One representative OCT slice for each particle gel and the agarose only control are shown.

Although there seem to be little qualitative differences between the particle images and the control, the image analysis results (Figure 6-5) show more definitive differences. Indeed, each particle-laden gel has a significantly higher MSD than that of the agarose only control gel ($p<0.001$), with Gd-PEI being the highest. This indicates that all three coated Gd-carbonate particles are effective OCT contrast agents in agarose at 1mM. Although there was no significant difference between the MSDs of Gd-PAA and Gd-PEG, the third coating, Gd-PEI actually had a significantly higher MSD ($p<0.001$) than each of the other two. This suggests that the PEI coating significantly enhances the light scattering properties of lanthanide-doped particles when held homogeneously in an agarose gel. However, during experimental manipulation of the particles we did encounter some aggregation, particularly with the PEI coating (not shown here) which could explain why this coating causes higher OCT signal.

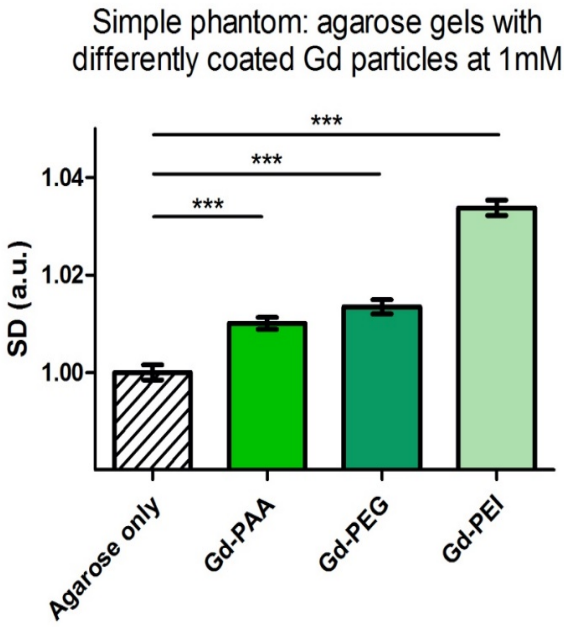

*Figure 6-5: Standard deviation analysis results of a "simple" phantom containing agarose with Gd-carbonate particles of 3 different coatings (PAA, PEG and PEI). All values normalised to agarose only control, ns=not significant, * p<0.05, ** p<0.01, *** p<0.001. Error bars=SEM.*

6.3.2.2 Cell viability

In order to determine the toxicity of the 3 differently coated Gd-carbonate particles, MTT cell proliferation assays were performed on RAW cells after incubation with each of the particles at concentrations of 1mM for either 2 or 20 hours. The results in Figure 6-6 show that cells have over 60% viability after 2-hour exposure to each of the particles whereas they have only about 5% viability after 2 hour exposure to the negative control, DMSO. At the 2-hour incubation timepoint, Gd-PEG shows the lowest toxicity, with around 95% cell viability compared to 65% and 60% for Gd-PAA and Gd-PEI respectively. When the macrophages were incubated with the particles for 20 hours Gd-PEG was again the least toxic with around 55% viability compared to 25% for Gd-PAA and Gd-PEI. Clearly the 20-hour time point is more important in terms of clinical relevance so it should be noted that all particles had a significant increase in toxicity when incubated with RAW cells for that length of time.

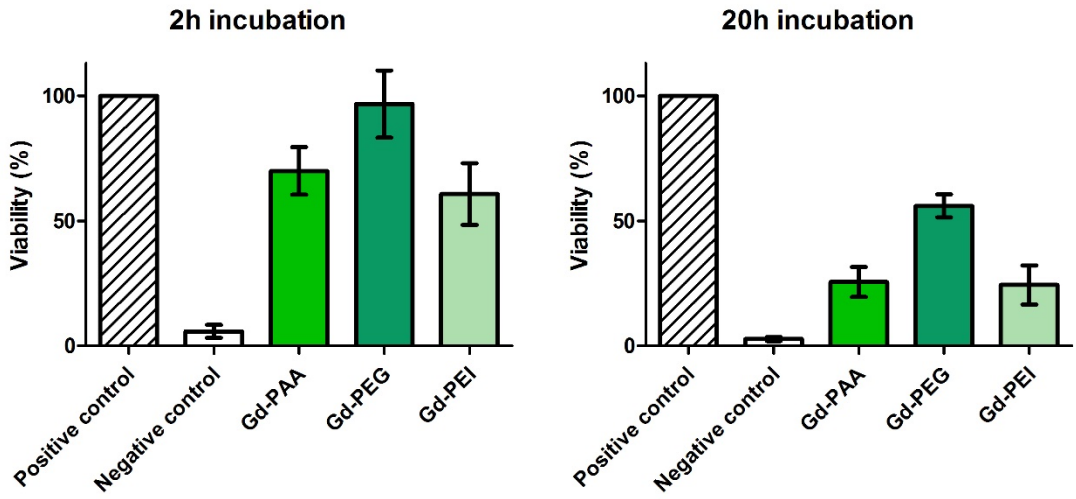

Figure 6-6: Cell viability of mouse macrophages after incubation with differently coated Gd-carbonate particles for 2 and 20 hours. Mouse macrophages were incubated with the particles at concentrations of 1mM before performing an MTT colorimetric assay to assess viability (shown as percentage of positive control). N= 4 and Error bars = SEM.

6.3.2.3 OCT testing particle-laden macrophages

The next step was to test the efficacy of the three coated Gd particles for OCT signal enhancement of macrophages. To this end, a set of "macrophage phantoms" were made as described in section 6.2.4. The 5 sections of each phantom contained the following: 1) agarose only control, 2) 20 million untreated murine macrophages, 3, 4 and 5) 20 million murine macrophages loaded with each of the 3 Gd coated particles: Gd-PAA, Gd-PEG and Gd-PEI. The loading of the particles into the macrophages was performed by incubations with the particles at 1mM concentrations in media for 24 hours. Three repeats of this phantom were made and imaged with IV-OCT. Representative OCT images of each macrophage gel from one of the phantoms are shown in Figure 6-7. It is immediately clear that these are brighter and more granular than those of the simple phantom in Figure 6-4, confirming that once again, macrophages on their own are detectable with OCT. Moreover, the particle loaded macrophage gel images in Figure 6-7 are substantially brighter, with more very bright spots than the macrophage only gel. However, it is hard to differentiate the images of the 3 differently coated particle treatments (Gd-PAA, Gd-PEG and Gd-PEI) from each other. This suggests that, regardless of coating, Gd-carbonate particles are effective at the enhancing OCT contrast of macrophages.

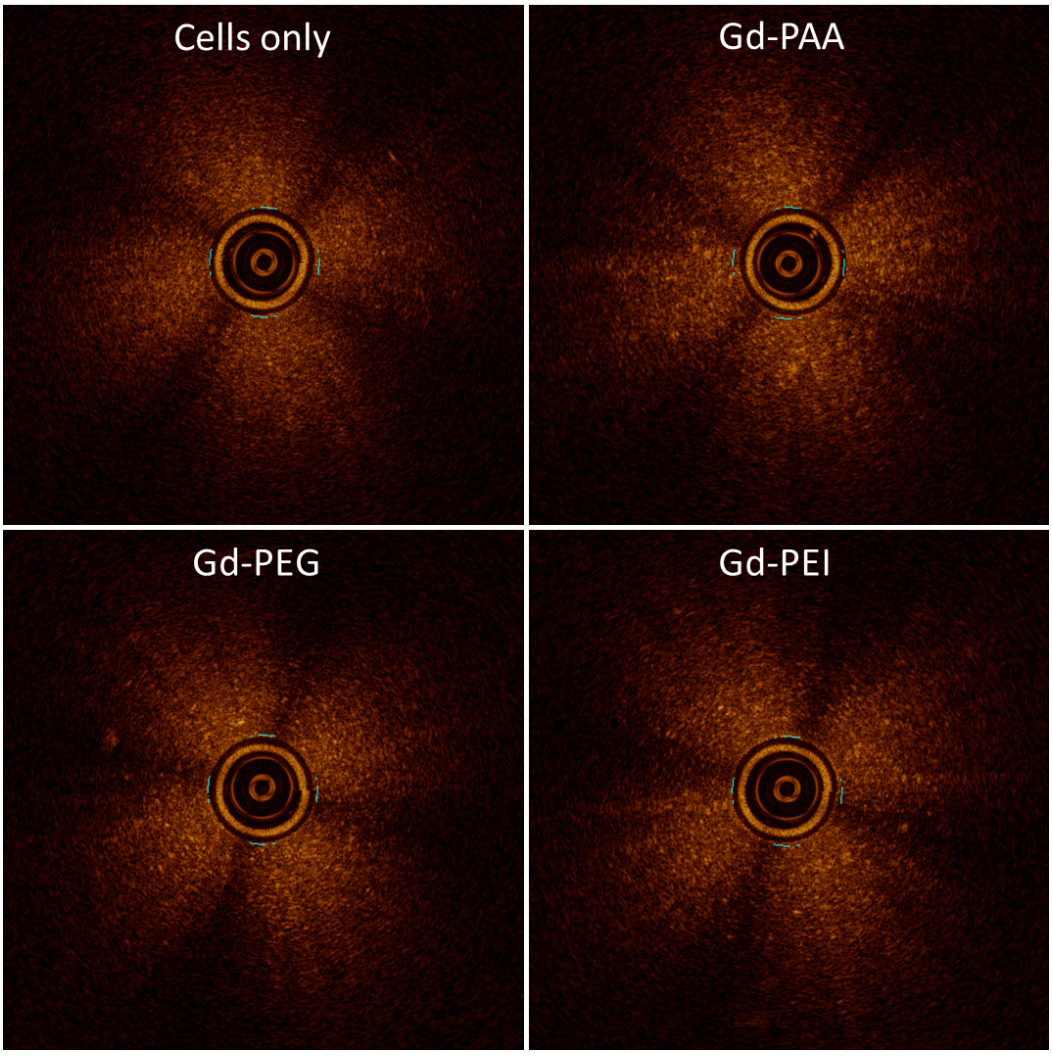

Figure 6-7: OCT images of an agarose phantom made with macrophage s loaded with 3 differently coated (PAA, PEG and PEI) Gd particles. Each section of the phantom was made up of 1.5% agarose with 20x10^6 macrophages having been incubated with the stated particle at 1mM. One representative OCT slice for each particle gel and the cells only control are shown.

These findings are confirmed by the quantitative image analysis results from the 3 macrophage phantoms made, shown in Figure 6-8. Indeed, in the pooled results of the phantoms, all 3 Gd coated particles significantly enhanced the MSD of OCT images compared to the cells only control. Gd-PAA showed the largest increase compared to cells control, followed by Gd-PEG and then Gd-PEI. This was also the case in the individual image analysis results for all 3 phantoms, the only difference being that Gd-PEI did not significantly increase the MSD compared to the cells control in phantom 1. It is clear from this figure that all three Gd coated particles are effective OCT contrast agents for murine macrophages, with Gd-PEI being the least consistent of the 3.

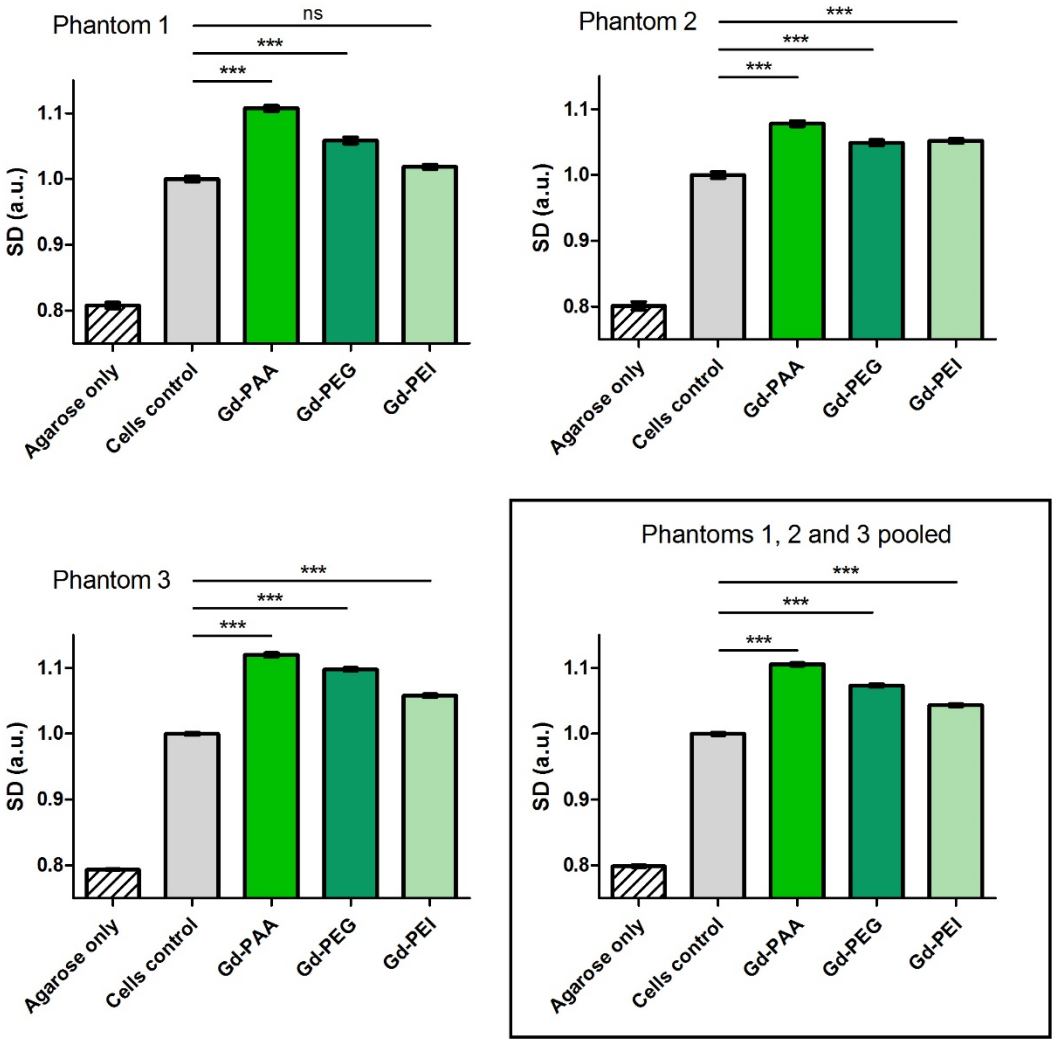

*Figure 6-8: Standard deviation analysis results of 3 identical phantoms containing cells loaded with Gadolinium particles of 3 different coatings (PAA, PEG and PEI). The bottom figure shows the results of these 3 phantoms pooled together. All values normalised to cells only control, ns= not significant, * p<0.05, ** p<0.01, *** p<0.001. Error bars = SEM.*

6.3.2.4 MRI contrast confirmation

After the initial OCT screenings of a panel of 9 different lanthanide particles (section 6.3.1), the Gd carbonate particle was selected, in part for its good OCT contrast properties but also in part for its potential for multi-modal imaging. Indeed, gadolinium is widely used as an MRI contrast agent in humans. In view of this, it is important to verify that the coated Gd carbonate particles screened in this section are good MRI contrast agents as well as OCT ones.

Each proton in the hydrogen atoms of the human body has a magnetic moment (it spins on an axis) so when exposed to a large magnetic field (from the MRI machine), the protons line

up and spin at a particular frequency. When the magnet is turned off, the protons relax to their initial positions at different frequencies depending on the tissue type. The rate at which the protons return to their relaxed state is what is measured by the MRI machine and determines the image contrast between different tissues which all have slightly different relaxation times. T1 refers to the relaxation time of magnetisation occurring in the same direction as the MRI magnetic field whereas T2 refers to the relaxation time of magnetisation occurring perpendicular to it. T1 and T2 weighted images confer different advantages in different tissue types, which we will not detail here. When considering an MRI contrast agent, it is of interest to determine whether the agent significantly changes the T1 or T2 relaxation times compared to the control by making them shorter or longer.

MRI imaging of the simple phantom (presented in section 6.3.2.1) and the macrophage phantom 3 (presented in section 6.3.2.3) of the 3 differently coated Gd particles was performed and the results are shown in Figure 6-9. The T1 and T2 relaxation times of the gels containing particles or particle-laden cells were all shorter than the agarose only and cell only control gels. Interestingly, the particle-laden cell gels all had shorter T1 and T2 relaxation times than the gels with particles alone. Looking at the macrophage gels, Gd-PEI shows the shortest T1 relaxation time, followed by Gd-PAA and the Gd-PEG, with less than 0.3s between each. However, the Gd-PAA laden macrophage gel had the shortest T2 relaxation time by about 9ms with Gd-PEG and Gd-PEI next and only 0.1ms apart. These results clearly show that the three coated Gd-carbonate particles are effective MRI contrast agents, but it is difficult to definitively say which of the 3 produces the best contrast.

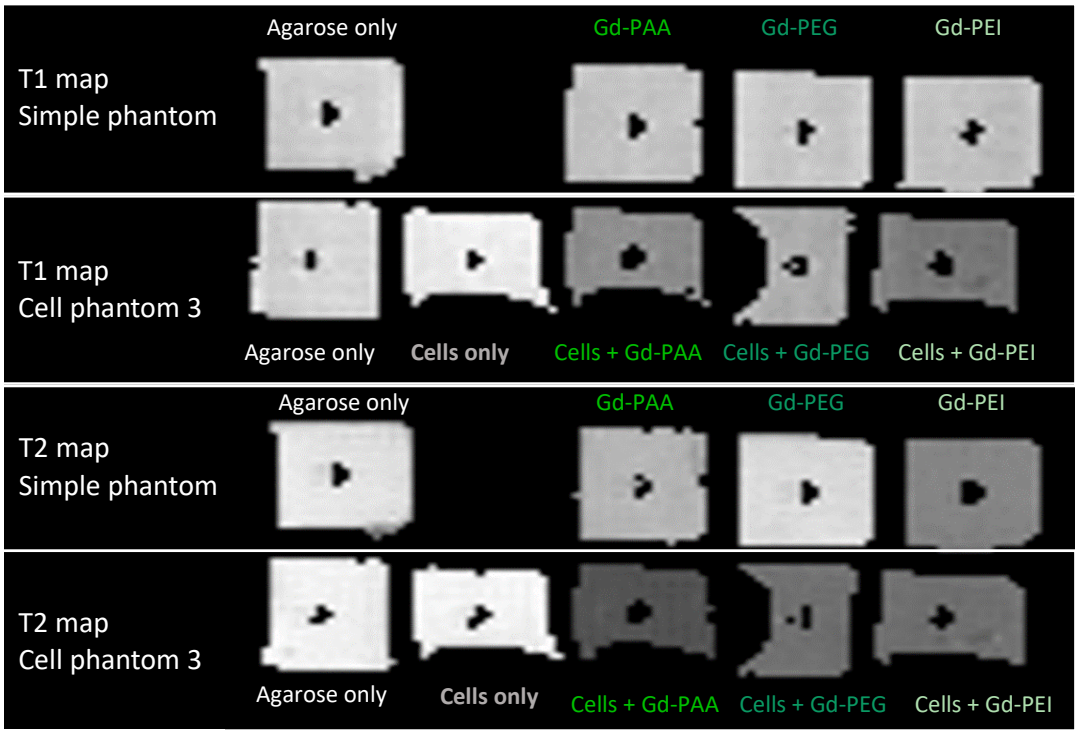

	Agarose only	Cells only	Gd-PAA	Gd-PEG	Gd-PEI
T1 map Simple phantom	1.93 s	X	1.81 s	1.87 s	1.82 s
T1 map Cell phantom 3	2 s	2.14 s	1.32 s	1.6 s	1.17 s
T2 map Simple phantom	70.2 ms	X	56.5 ms	67.8 ms	41.2 ms
T2 map Cell phantom 3	74.3 ms	76.1 ms	25.8 ms	34.7 ms	34.8 ms

Figure 6-9: Results of MRI imaging of two phantoms, the "simple" phantom containing solely agarose mixed with the differently coated Gd-carbonate particles and the cell phantom 3 containing mouse macrophages loaded with the same particles, embedded in agarose.

6.4 Discussion

To summarize, in this chapter the IV-OCT imaging properties of novel lanthanide-based nanoparticles were investigated in vitro and there were three main outcomes. The first is that the phantom methodology developed in Chapter 3 enabled the effective screening of multiple nanoparticles and the identification of the Gd-based particle as the one with highest IV-OCT contrast potential. Secondly, the particle selected to take into subsequent cell experiments ($Gd(OH)CO_3$) was shown to still produce a high IV-OCT signal when coated for

biocompatibility and was not found to be significantly cytotoxic. And finally, when loaded into cells, the Gd based particles were found to significantly increase the IV-OCT signal of these cells and retained their MRI contrast capabilities. Each of these three outcomes will be discussed in more detail subsequently.

Firstly, section 6.3.1 presented the results of screening the 9 lanthanide-based particles with IV-OCT using the previously developed phantom mould (section 2.3) and analysis method (section 2.4) and this enabled us to select Gd-based particles as those with the highest potential for future OCT investigations, confirming **hypothesis 1** of this chapter. The first step of this investigation was to IV-OCT image all the particles simply in solution and the resulting images made it immediately obvious that the carbonate structure particles were far superior contrast agents to the fluoride structure ones. Therefore, 4 carbonate particles doped with different lanthanides (Yb, Nd, Dy, Gd) were taken to the next screening step: imaging in agarose phantoms. The image analysis results of the phantoms showed that all particles, when held homogeneously in an agarose gel, yielded significantly higher OCT contrast than the control gel. In addition, the Gd-based carbonate particle showed the highest OCT signal of the 4. Prompting us to select it for future optimisation involving cell work. For this purpose, Zhigao Yi coated the Gd based nanoparticle with three different coatings: PEI, PEG and PAA.

Subsequently, section 6.3.2 presented the results of investigations of this Gd-based particle having been given 3 different coatings for biocompatibility. In a first instance, these investigations showed that the coated particles (when held homogeneously in an agarose gel) still produced high OCT contrast and were not found to be cytotoxic, confirming **hypothesis 2** of this chapter. Indeed, section 6.3.2.1 tested the IV-OCT properties of the three coated Gd particles held homogeneously in agarose gels with the same methods as previously and found them to each cause a significant increase in the OCT signal compared to the agarose only control. Interestingly, the PEI coated Gd particle showed significantly higher OCT contrast than the other two coatings suggesting the PEI coating confers additional light scattering properties to the particle. However, we did observe the Gd-PEI particles aggregating which could explain their higher OCT standard deviation: a bigger clump of particles will cause higher light scattering. It would be interesting to properly investigate the aggregation rate of all the Gd-coated particles but that was beyond the scope of this screening study. In section 6.3.2.2 we presented the results of cell viability assays with the coated particles and were able to conclude that none of the particles had high toxicity and

that the PEG coating conferred the least toxicity to RAW cells both at 2-hour (5% toxicity) and 20-hour (45% toxicity) time points. These results make sense given the widely accepted biocompatibility that PEGylation confers in many biological systems[146–148]. Additionally, many Gadolinium based MRI contrast agents have been FDA approved and used extensively in the past 30 years[145], giving a good precedent for the safety of our Gadolinium doped upconversion particle. However, these cell viability assays were simply preliminary experiments and should of course be further validated in the future with safety studies in different cell types, animals and eventually humans.

Finally, sections 6.3.2.3 and 6.3.2.4 presented the investigation of the effects that these coated Gd particles have on imaging when loaded into macrophages. The phantoms created showed that pre-treatment with each of the coated particles significantly enhanced the OCT signal and MRI contrast of macrophages, confirming **hypothesis 3** of this chapter. Indeed, thanks to the in vitro phantom framework developed in Chapter 3 we were able to test the OCT and MRI imaging properties of macrophages pre-loaded with Gd-based upconversion nanoparticles for the very first time. Interestingly cell loading with Gd-PAA yielded the highest OCT signal, followed by Gd-PEG and then Gd-PEI. This is in contrast to the results of the particle only phantoms which showed Gd-PEI to have the highest OCT signal enhancement properties. The observation that these particles may aggregate when in solution, along with the fact that they had the highest toxicity of the 3 coatings leads us to believe that Gd-PEI may have been less efficiently taken up by macrophages than the other two particles. Less efficient cell loading would therefore lead to much lower OCT contrast. This theory would of course need to be verified by conducting particle uptake quantification assays, perhaps with flow cytometry by utilising the particles' light emitting abilities. Furthermore, section 6.3.2.4 presented results of MRI imaging of the gels from two phantoms (particles alone and particles in macrophages) in order to confirm the magnetic properties of these coated upconversion particles. It was indeed found that all three coated particles, whether alone in gels or loaded into macrophages had shorter T1 and T2 relaxation times than the controls. This of course was a very simple preliminary MRI experiment which will require more detailed investigations should dual modality OCT-MRI imaging become a priority of this upconversion particle study.

There are a few limitations to this chapter, some of which have already been referred to briefly. In particular, we did not quantify the uptake of the coated Gd particles by the

macrophages. Contrarily to USPIOs (as seen in section 3.3.1) we could not see the particles in the macrophage endosomes under the microscope. Thanks to the significantly enhanced OCT signal of the macrophages when they have been treated with the particles it is pretty safe to assume that the particles have been internalised. It would however be very important for future studies to actually quantify this internalisation and perhaps investigate the mechanisms of uptake. We propose here that this could be done with flow cytometry by utilising the particles' remarkable ability to re-emit light absorbed at a different wavelength. This is also how we suggest macrophage functionalisation could be implemented. Indeed, so far we have not made any modifications to the particle to make it macrophage specific. An important aim of future studies will be to turn the Gd-PEG particle into a probe which can target pro-inflammatory macrophages for their specific detection in vivo with IV-OCT. Another limitation of this chapter is the lack of comparison to other imaging agents. It would be interesting to see how these new particles fair in terms of IV-OCT contrast up against the published gold nanostructures[126–129] but this was beyond the scope of this study. A quick comparison between Figure 3-8 and Figure 6-8 suggests that the Gd-doped particles are better at enhancing the IV-OCT signal of macrophages than USPIOs are but a more robust analysis, with more Gd-macrophage phantoms would be necessary for confirmation of this observation. Finally, as mentioned previously, further biocompatibility and safety experiments will be necessary when moving forward with this investigation.

In conclusion, this novel in vitro study has for the first time proven the IV-OCT contrast enhancement abilities of lanthanide-doped upconversion nanoparticles. A bespoke phantom model and image analysis method were used to screen a panel of lanthanide based particles and identify ones with highest OCT contrast. The Gd-doped upconversion particle was then PEG coated for biocompatibility, shown not to be significantly cytotoxic and found to significantly enhance the IV-OCT detection of macrophages. This perspective study utilised the robust OCT phantom framework developed in this thesis and made a first step towards the development of a truly OCT and macrophage specific contrast agent. The ability of this particle to be fine-tuned for many applications is unmatched and will prove invaluable for its development into a plaque macrophage OCT probe.

7 CHAPTER SEVEN: SUMMARY AND FUTURE DIRECTIONS

The work in this thesis has concentrated on advancing methodologies aimed at enhanced detection of macrophages with a clinical IV-OCT system. This was investigated in vitro, in a mouse model of atherosclerosis and finally in humans presenting with symptomatic coronary artery disease. In this concluding chapter we will first give a brief summary of the findings of each individual chapter, followed by an overview of the translational USPIO-OCT study as a whole (chapters 3, 4 and 5). Finally, the limitations of the work of this thesis and possible future directions will be described.

7.1 Summary of Thesis Chapters

7.1.1 Chapter Three: In vitro Phantom USPIO-OCT Study

In Chapter 3, for the first time, we presented a robust in vitro phantom model and image analysis methodology which is highly translatable to in-vivo clinical imaging and allows easy, standardised screening of imaging agents with IV-OCT. Nothing of this kind has previously been published in the literature. Indeed, although a few authors have investigated the OCT contrast properties of nanoparticles in vitro[126–130], only one has done this with particles loaded into macrophages[93]. In this study we confirmed USPIO uptake by macrophages in a dose dependent fashion and confirmed our **chapter 3 hypothesis: intra-cellular USPIOs enhanced the detection of macrophages on IV-OCT images**. Indeed, we demonstrated that RAW macrophages loaded with USPIOs produced significantly higher standard deviation of pixel intensity on OCT images (OCT SD) compared to untreated macrophages across seven repeat experiments and over a thousand total images analysed. The optimal USPIO concentration for this enhanced OCT signal was found to be between 0.05 and 0.25 mg/ml, an observation that then informed the dosing in the subsequent *in vivo* studies.

7.1.2 Chapter Four: Ex vivo Mouse USPIO-OCT Study

In Chapter 4, for the first time, we imaged the aortic plaques of ApoE$^{-/-}$ mice with a current clinical IV-OCT system. Indeed the only published study[83] having attempted this did so with a now redundant, lower quality IV-OCT system which used a catheter half the diameter of the one currently used in the clinic. Our study confirmed the ability of IV-OCT to clearly depict the miniaturised plaque structures in mice (fibrous cap and lipid pool were easily identified). And image analysis comparison of mice treated with USPIO and saline confirmed the main **chapter 4 hypothesis that the plaques of USPIO treated mice will have a higher signal on IV-OCT images compared to untreated mice**. Indeed, the local OCT SD values were

significantly higher in the plaque caps of USPIO treated mice compared to saline treated mice and compared to non-plaque areas of the aortic wall. This increased signal is expected to correlate with the presence of activated USPIO-laden macrophages on histology, however this data, whilst acquired is not yet available. Importantly, no increase in OCT signal variance was observed within regions of normal aorta that were free from atherosclerosis and activated macrophages. To get around the large size of the current clinical IV-OCT catheter, we had to excise the mouse aortas and cut them open for ex vivo imaging. It would be preferable to confirm these findings with an in vivo whole vessel imaging approach, however this is only possible in a larger animal model (pig or hyperlipidaemic rabbit) which we did not have access to.

7.1.3 Chapter Five: In vivo Human USPIO-OCT Clinical Trial

In Chapter 5, we translated this novel USPIO-OCT approach into humans within the context of a randomised clinical trial. Even though USPIOs have been approved for clinical use in over 10 years, this is the first attempt to use them as an OCT contrast agent in vivo. In this study we confirmed the main **Chapter 5 hypothesis that culprit plaques of USPIO treated ACS patients will yield higher OCT signal compared to saline treated ACS patient culprit plaques and compared to all non-culprit plaques**. Indeed, the local OCT SD values in culprit plaque caps of patients who had been administered USPIO were significantly higher than in those who had received saline placebo treatment. And they were also significantly higher than local OCT SD values in the caps of all non-culprit plaques. Following myocardial infarction there is generalised atherosclerotic plaque inflammation, so it is reassuring that the local SD was also increased in the non-culprit plaques of patients administered USPIO versus similar plaques in patients pre-treated with saline. These findings confirm the clinical translatability of USPIO enhanced detection of coronary plaque inflammation with OCT.

7.1.4 Chapter Six: Novel OCT Contrast Agents for Macrophage Detection

As mentioned above, in chapter 3 we demonstrated the capability of USPIOs to enhance the IV-OCT signal associated with macrophages when loaded into the cells by using a bespoke 3D printed phantom artery mould. These results were subsequently confirmed in both murine and human in vivo settings. Despite this success, we postulated that there must be other agents with high scattering properties which could be made more specific to OCT and importantly, targeted to activated plaque macrophages. With this in mind, in Chapter 6 we utilised this in vitro IV-OCT screening framework to start anew, with lanthanide-doped

upconversion particles. The advantage being that they are tuneable in all aspects: light scattering (for OCT detectability), magnetism (for MRI detection) and light emission (for fluorescence imaging). In this novel in vitro study, we showed for the first time that lanthanide-doped upconversion particles significantly increase IV-OCT local SD and many of them would make excellent candidates for macrophage tagging. In particular we tested the Gd-based particle ($Gd(OH)CO_3$) loaded into macrophages and found it to significantly enhance their OCT detection (even more so than USPIOs). This confirms the main **Chapter 6 hypothesis: that a novel lanthanide based particle will significantly enhance the OCT detection of macrophages in-vitro.** This perspective study utilised the robust OCT phantom framework developed in this thesis and made a first step towards the development of a truly OCT and macrophage specific contrast agent. The ability of this particle to be fine-tuned for many applications is unmatched and will prove invaluable for its development into a plaque macrophage OCT probe.

7.2 Overview of our translational USPIO-OCT study

Together Chapters 3, 4 and 5 present a translational molecular imaging study in which we have demonstrated that USPIOs enhance the visualisation and quantification of vascular macrophages on OCT in vitro, in mouse models of atherosclerosis and in a clinical randomised controlled trial of patients presenting with acute myocardial infarction. The in vitro phantom and murine studies confirmed that increased OCT local SD is associated with the accumulation of USPIO particles in vascular macrophages, whilst the clinical studies demonstrated increased USPIO-enhanced OCT local SD in the culprit plaques and areas of recent plaque rupture responsible for myocardial infarction. This novel approach holds major promise in providing real time assessments of inflammatory activity in individual coronary plaques and could soon be ready for widespread investigation in patients undergoing invasive coronary angiography.

Inflammation is a key pathological process underlying the development of atherosclerosis and an important trigger to plaque rupture and myocardial infarction. Whilst novel anti-inflammatory therapies have demonstrated their ability to reduce cardiovascular events[59–63], imaging techniques capable of directly imaging inflammation in the coronary arteries are lacking. For the first time we have demonstrated the ability of USPIO-enhanced OCT to detect macrophage accumulation in atherosclerotic plaque. A major advantage of our approach is that it makes use of a contrast agent and invasive imaging technology that have already

established an excellent safety profile in humans. It is therefore ready for widespread investigation in humans without the need for lengthy approvals. Moreover, OCT imaging systems are available in most invasive catheter laboratories and are familiar to many interventional cardiologists, potentially facilitating rapid future adoption of this technique. By comparison many other intravascular contrast agents are either not yet approved for human application or require bespoke catheters that are themselves not clinically approved or are expensive to purchase and install.

In this translational imaging study, we have demonstrated the potential of USPIO-enhanced OCT imaging across a range of different experimental settings. In vitro we confirmed USPIO uptake by macrophages in a dose dependent fashion, and that intra-cellular USPIOs enhanced the detection of macrophages on IV-OCT images. The optimal USPIO concentration was found to be 0.05 mg/ml, an observation that then informed the dosing in the subsequent in vivo studies. The atherosclerotic mouse model study provided confirmation that similar mechanisms are occurring in vivo: increased OCT signal was observed in the atherosclerotic plaques of mice pre-treated with USPIO as compared to those administered saline. Finally, we have translated this novel approach into humans within the context of a randomised clinical trial in Chapter 5. Here the highest OCT signal was observed in the culprit plaques of patients with a recent MI who had been administered USPIO. These studies therefore suggest that the increased OCT signal observed with USPIO administration is specific to activated macrophages within atherosclerotic plaque.

Our work supports and extends the original observations by Tearney and colleagues[89] that macrophages present within atheroma demonstrate greater OCT signal intensity and variance than their surroundings causing an increase in the local standard deviation of pixel intensity (SD). Whilst differences due to USPIO accumulation are not readily discernible on visual assessment of raw OCT images, the enhanced signal becomes readily apparent when the OCT local SD is quantified. We believe this is because the metallic properties of the USPIO particles scatter the OCT light and increase variance in pixel intensity.

Building on these observations we developed a novel image analysis approach that overlays this SD information on top of the anatomical information provided by OCT. A colour scale is used to highlight hotspots where the local SD is increased above a specific threshold, facilitating anatomical mapping of regions of USPIO accumulation and therefore macrophage inflammation. Such maps allow for a rapid visual assessment of the inflammatory activity

highlighted by this approach and combine it with the structural information familiar to interventional cardiologists. The spatial distribution of macrophages within the plaque can therefore also be appreciated, allowing differentiation from the many other plaque constituents (microcalcifications, cholesterol crystals, or internal and external elastic membranes) that share similar visual characteristics on OCT. If real time analysis can be successfully developed, then this technique would hold major promise as a biomarker of atherosclerotic plaque inflammation that might be used to aid clinical decision making for patients undergoing invasive coronary angiography.

7.3 Limitations and Future Directions

The work of this thesis has several important limitations which will influence and inform future work in this field. Firstly, the contrast agents tested are not yet explicitly specific to activated macrophages and could be functionalised in the future. Secondly, we lack histological validation of our OCT findings in mice and humans. Thirdly, our murine and clinical studies are small and whilst their randomized nature and the blinded image analysis are strengths, this data needs to be confirmed in larger studies and in different patient populations. A fourth important limitation is that the image analysis methods, particularly the SD hotspot overlay tool are not fully automated and still currently require manual ROI drawing. Finally, once the image analysis tools will be ready to use in the clinic, treatment strategies will need to be developed and tested in randomised clinical trials. These limitations will be discussed in more detail subsequently.

7.3.1 Specificity to activated macrophages

Our work in the in vitro chapters (3 and 6) did not investigate specifically targeting activated plaque macrophages. In these chapters we relied on the premise that macrophages readily take up nanoparticles and that this is enhanced when they are activated. In the case of USPIOs this is partly true in that these particles have been previously been found to accumulate in activated plaque macrophages in humans[105–107] and animal models[98–104], however the mechanism of uptake is not well studied. It would be interesting to investigate which macrophage profiles preferentially uptake USPIOs, if other immune cells also take them up and whether this affects the efficacy of their use in vivo. In the case of the lanthanide-doped particles studied in chapter 6, there was evidence in our studies that the PEI coated Gd particles were aggregating and this was affecting their cellular uptake. Although we didn't notice any of these issues with the other particles, it is important to

investigate this in the future. How efficiently are particles being taken up? Which type of cells preferentially take them up? Can this mechanism be tuned for more specific and efficient uptake by activated plaque macrophages? Indeed, the limitations outlined here with our in vitro work highlight the need for a macrophage profiling and targeting study in order to better functionalise future OCT contrast agents. There have been many published studies of plaque macrophage profiling, some of which are cited here[149–151] and reviewed here[152]. The methods developed in these papers could be used as a starting point for functionalising our OCT contrast agents. As outlined in Chapter 6, the novel lanthanide-doped upconversion particles have a notable advantage for conducting this kind of study: in addition to being excellent at scattering light (essential for good detection with OCT) they have the potential to emit light at almost any wavelength desired[143,144,153].

7.3.2 Histological validation of USPIO-laden macrophages

In our mouse and human studies (Chapters 4 and 5), we lack histological validation of our OCT findings. However, obtaining coronary tissue from patients undergoing percutaneous coronary intervention (PCI) for myocardial infarction is not possible. We must therefore rely on histological validation provided in mouse models, so it is a shame that this investigation was not able to be finalised before the publication of this thesis. In this histology investigation, each ApoE$^{-/-}$ mouse aorta is being sectioned and stained for iron with Perls Prussian blue (shown to stain USPIOs in previous studies) and plaque macrophages with CD68. We expect this analysis to provide confirmation that USPIOs have accumulated in plaque macrophages and that their locations within the fibrous caps will correlate with the "SD hotspots" found on OCT imaging. Without the results of this investigation, we cannot yet properly confirm that the increased OCT local SD in USPIO treated mice is due specifically to USPIO accumulation within plaque macrophages. However, it is highly likely to be the case, given the clear and consistent in vitro data demonstrating increased OCT-SD to be due to USPIO loading of mouse macrophages.

7.3.3 Automation of SD hotspot tool

One of the main limitations of the thesis as a whole is the partially manual nature of the image analysis method. Indeed, for both the SD analysis and the SD hotspot tool overlay, regions of interest had to be drawn on the OCT images in order to avoid artefacts and restrict the analysis to the cap of plaques (in the case of the mouse and human study). This is necessary because many things outside the cap of plaques will cause a high SD. Indeed the

boundaries between different tissue structures such as the fibrous cap and the lipid pool or the intima and a calcium nodule will cause a high SD value due to the structures having such different pixel intensities. For these reasons, all studies currently published on the identification of macrophages with OCT have had to draw ROIs to restrict their analysis to the fibrous caps, as we have [89,92,139,140]. However in recent years there have been many studies attempting to develop automated detection and characterisation of coronary plaque components on IV-OCT images such as lumen and plaque contours, plaque constitution (lipid or calcium rich) and even the fibrous cap[82,154–158]. In these studies, many different computational techniques were tested, resulting in varying degrees of specificity and sensitivity. While we cannot review them all here, it is reasonable to believe that one of these will soon help us achieve automatic real time visualisation of plaque cap macrophage burden using the SD hotspot tool.

7.3.4 USPIO-OCT treatment strategies

Once the automated SD hotspot tool is developed, how might USPIO enhanced OCT imaging be used in clinical practice? The imaging of inflammation within individual coronary plaques holds promise in directing decision making in patients undergoing invasive angiography with a view to PCI. In some patients, uncertainty exists as to the true culprit lesion and therefore which plaque should undergo PCI. A readily available, near real-time measure of local inflammation may help in the identification of such plaques. In addition, controversy persists about whether patients with a recent MI and multi-vessel coronary artery disease should undergo intervention to all obstructive coronary lesions or just the culprit. Here also a readout of inflammation at an individual plaque level may help guide appropriate intervention, avoiding the need for unnecessary stents whilst directing therapy to plaques at highest risk of causing recurrent events. At a more general level, the precise detection of a high burden of inflamed “vulnerable plaques” could aid in patient stratification. This could in the future inform the used of targeted, more expensive anti-inflammatory therapies shown to work extremely well on particularly vulnerable patients[59–63] but perhaps unnecessary and even detrimental to the health of more stable patients. USPIO-OCT holds promise as an easy-to-use, readily accessible technique with which to test these important treatment strategies in randomised clinical trials.

7.4 CONCLUSIONS

In this novel translational thesis, we have established methods for the enhanced detection and quantification of macrophages with the clinical IV-OCT system in-vitro, ex-vivo and in-vivo. We have confirmed our overarching hypothesis that macrophages can be detected and quantified on IV-OCT images using the standard deviation of pixel intensity metric and that this detection can be enhanced and made more specific by labelling with metallic particles, specifically USPIOs and novel lanthanide-based nanoparticles. Administration of USPIO enhances the detection of activated macrophages by OCT in pre-clinical models of atherosclerosis and patients undergoing invasive angiography following myocardial infarction. This novel approach is ready for human application, with major potential to enhance the imaging of inflammation within individual coronary plaques and to help guide clinical decision making in the catheterization lab.

REFERENCES

1. Bhatnagar, P., Wickramasinghe, K., Williams, J., Rayner, M. & Townsend, N. The epidemiology of cardiovascular disease in the UK 2014. *Heart* **101,** 1182–1189 (2015).

2. British Heart Foundation. UK Factsheet. *British Heart Foundation* 1–21 (2020).

3. Mendis, S., Puska, P. & Norrving, B. Global atlas on cardiovascular disease prevention and control. *World Health Organization* 2–14 (2011).

4. Arbab-Zadeh, A., Nakano, M., Virmani, R. & Fuster, V. Acute Coronary Events. *Circulation* **125,** 1147–1156 (2012).

5. Libby, P. Mechanisms of Acute Coronary Syndromes and Their Implications for Therapy. *New England Journal of Medicine* **368,** 2004–2013 (2013).

6. Thygesen, K., Alpert, J. S., Jaffe, A. S., Simoons, M. L., Chaitman, B. R. & White, H. D. Third universal definition of myocardial infarction. *European Heart Journal* **33,** 2551–2567 (2012).

7. Grech, E. D. & Ramsdale, D. R. Acute coronary syndrome : unstable angina and non-ST segment elevation myocardial infarction Pathogenesis. *Bmj* 1259–1261 (2003). doi:10.1136/bmj.326.7401.1259

8. Yeghiazarians, Y., Braunstein, J. B., Skari, A. A. & Stone, P. H. Unstable Angina Pectoris. *The New England Journal of Medicine* **342,** 101–114 (2000).

9. Crea, F. & Liuzzo, G. Pathogenesis of Acute Coronary Syndromes. *Journal of the American College of Cardiology* **61,** 1–11 (2013).

10. Weber, C. & Noels, H. Atherosclerosis: current pathogenesis and therapeutic options. *Nature Medicine* **17,** 1410–1422 (2011).

11. Tabas, I., Williams, K. J. & Boren, J. Subendothelial Lipoprotein Retention as the Initiating Process in Atherosclerosis: Update and Therapeutic Implications. *Circulation* **116,** 1832–1844 (2007).

12. Libby, P., Ridker, P. M. & Hansson, G. K. Progress and challenges in translating the

biology of atherosclerosis. *Nature* **473,** 317–25 (2011).

13. Libby, P. & Theroux, P. Pathophysiology of Coronary Artery Disease. *Circulation* **111,** 3481–3488 (2005).

14. Tabas, I. Macrophage death and defective inflammation resolution in atherosclerosis. *Nature Reviews Immunology* **10,** 117 (2010).

15. Toschi, V., Gallo, R., Lettino, M., Fallon, J. T., Gertz, S. D., Fernandez-Ortiz, A., Chesebro, J. H., Badimon, L., Nemerson, Y., Fuster, V. & Badimon, J. J. Tissue Factor Modulates the Thrombogenicity of Human Atherosclerotic Plaques. *Circulation* **95,** 594–599 (1997).

16. Wilcox, J. N., Smith, K. M., Schwartz, S. M. & Gordon, D. Localization of tissue factor in the normal vessel wall and in the atherosclerotic plaque. *Proceedings of the National Academy of Sciences* **86,** 2839–2843 (1989).

17. Nikkari, S. T., O'Brien, K. D., Ferguson, M., Hatsukami, T., Welgus, H. G., Alpers, C. E. & Clowes, A. W. Interstitial Collagenase (MMP-1) Expression in Human Carotid Atherosclerosis. *Circulation* **92,** 1393–1398 (1995).

18. Herman, M. P., Sukhova, G. K., Libby, P., Gerdes, N., Tang, N., Horton, D. B., Kilbride, M. & Breitbart, R. E. Expression of Neutrophil Collagenase (Matrix Metalloproteinase-8) in Human Atheroma A Novel Collagenolytic Pathway Suggested by Transcriptional Profiling. *Circulation* **104,** 1899–1904 (2001).

19. Sukhova, G. K., Schönbeck, U., Rabkin, E., Schoen, F. J., Poole, A. R., Billinghurst, R. C. & Libby, P. Evidence for increased collagenolysis by interstitial collagenases-1 and -3 in vulnerable human atheromatous plaques. *Circulation* **99,** 2503–2509 (1999).

20. Shah, P. K., Falk, E., Badimon, J. J., Fernandez-Ortiz, A., Mailhac, A., Villareal-Levy, G., Fallon, J. T., Regnstrom, J. & Fuster, V. Human monocyte-derived macrophages induce collagen breakdown in fibrous caps of atherosclerotic plaques. Potential role of matrix-degrading metalloproteinases and implications for plaque rupture. *Circulation* **92,** 1565–9 (1995).

21. Getz, G. S. & Reardon, C. A. Animal models of Atherosclerosis. *Arteriosclerosis, Thrombosis, and Vascular Biology* **32,** 1104–1115 (2012).

22. Lent-Schochet, D. & Jialal, I. *Biochemistry, Lipoprotein Metabolism*. *StatPearls* (StatPearls Publishing, 2020). at <http://www.ncbi.nlm.nih.gov/pubmed/31985986>

23. Kapourchali, F. R., Surendiran, G., Goulet, A. & Moghadasian, M. H. The Role of Dietary Cholesterol in Lipoprotein Metabolism and Related Metabolic Abnormalities: A Mini-review. *Critical Reviews in Food Science and Nutrition* **56,** 2408–2415 (2016).

24. Biggerstaff, K. D. & Wooten, J. S. Understanding lipoproteins as transporters of cholesterol and other lipids. *Advances in Physiology Education* **28,** 105–106 (2004).

25. Kapourchali, F. R., Surendiran, G., Chen, L., Uitz, E., Bahadori, B. & Moghadasian, M. H. Animal models of atherosclerosis. *World Journal of Clinical Cases* 126–132 (2014). doi:10.12998/wjcc.v2.i5.126

26. Eichner, J. E., Dunn, S. T., Perveen, G., Thompson, D. M., Stewart, K. E. & Stroehla, B. C. Apolipoprotein E polymorphism and cardiovascular disease: A HuGE review. *American Journal of Epidemiology* **155,** 487–495 (2002).

27. Plump, A. S., Smith, J. D., Hayek, T., Aalto-Setälä, K., Walsh, A., Verstuyft, J. G., Rubin, E. M. & Breslow, J. L. Severe hypercholesterolemia and atherosclerosis in apolipoprotein E-deficient mice created by homologous recombination in ES cells. *Cell* **71,** 343–353 (1992).

28. Hobbs, H. H., Russell, D. W., Brown, M. S. & Goldstein, J. L. The LDL Receptor Locus in Familial Hypercholesterolemia: Mutational Analysis of a Membrane Protein. *Annual Review of Genetics* **24,** 133–170 (1990).

29. Watanabe, Y. Serial inbreeding of rabbits with hereditary hyperlipidemia (WHHL-rabbit). Incidence and development of atherosclerosis and xanthoma. *Atherosclerosis* **36,** 261–268 (1980).

30. Shiomi, M. & Ito, T. The Watanabe heritable hyperlipidemic (WHHL) rabbit, its characteristics and history of development: A tribute to the late Dr. Yoshio Watanabe. *Atherosclerosis* **207,** 1–7 (2009).

31. Epstein, F. H., Goldstein, J. L., Kita, T. & Brown, M. S. Defective Lipoprotein Receptors and Atherosclerosis: Lessons from an Animal Counterpart of Familial Hypercholesterolemia. *New England Journal of Medicine* **309,** 288–296 (1983).

32. Libby, P. Molecular Bases of the Acute Coronary Syndromes. *Circulation* **91,** 2844–2850 (1995).

33. Boden, W. E., O'Rourke, R. A., Teo, K. K., Hartigan, P. M., Maron, D. J., Kostuk, W. J., Knudtson, M., Dada, M., Casperson, P., Harris, C. L., Pharm, D., Chaitman, B. R., Shaw, L., Gosselin, G., Nawaz, S., *et al.* Optimal Medical Therapy with or without PCI for Stable Coronary Disease. *The New England Journal of Medicine* **356,** 1503–1516 (2007).

34. Giroud, D., Li, J. M., Urban, P., Meier, B. & Rutishauer, W. Relation of the site of acute myocardial infarction to the most severe coronary arterial stenosis at prior angiography. *The American journal of cardiology* **69,** 729–32 (1992).

35. Ambrose, J. A., Tannenbaum, M. A., Alexopoulos, D., Hjemdahl-Monsen, C. E., Leavy, J., Weiss, M., Borrico, S., Gorlin, R. & Fuster, V. Angiographic progression of coronary artery disease and the development of myocardial infarction. *Journal of the American College of Cardiology* **12,** 56–62 (1988).

36. Nobuyoshi, M., Tanaka, M., Nosaka, H., Kimura, T., Yokoi, H., Hamasaki, N., Kim, K., Shindo, T. & Kimura, K. Progression of coronary atherosclerosis: is coronary spasm related to progression? *Journal of the American College of Cardiology* **18,** 904–10 (1991).

37. Hackett, D., Davies, G. & Maseri, A. Pre-existing coronary stenoses in patients with first myocardial infarction are not necessarily severe. *Eur Heart J* **9,** 1317–1323 (1988).

38. Richardson, P. D., Davies, M. J. & Born, G. V. Influence of plaque configuration and stress distribution on fissuring of coronary atherosclerotic plaques. *Lancet (London, England)* **2,** 941–4 (1989).

39. Loree, H. M., Kamm, R. D., Stringfellow, R. G. & Lee, R. T. Effects of fibrous cap thickness on peak circumferential stress in model atherosclerotic vessels. *Circulation Research* **71,** 850–858 (1992).

40. Muller, J. E., Tofler, G. H. & Stone, P. H. Circadian Variation and Triggers of Onset of Acute Cardiovascular Disease. *Circulation* **79,** 733–743 (1989).

41. Virmani, R., Burke, A. P., Farb, A. & Kolodgie, F. D. Pathology of the Vulnerable Plaque. *Journal of the American College of Cardiology* **47,** 0–5 (2006).

42. Finn, A. V., Nakano, M., Narula, J., Kolodgie, F. D. & Virmani, R. Concept of vulnerable/unstable plaque. *Arteriosclerosis, Thrombosis, and Vascular Biology* **30,** 1282–1292 (2010).

43. Tarkin, J. M., Dweck, M. R., Evans, N. R., Takx, R. A. P., Brown, A. J., Tawakol, A., Fayad, Z. A. & Rudd, J. H. F. Imaging Atherosclerosis. *Circulation Research* **118,** 750–769 (2016).

44. Arbab-Zadeh, A. & Fuster, V. From Detecting the Vulnerable Plaque to Managing the Vulnerable Patient. *Journal of the American College of Cardiology* **74,** 1582–1593 (2019).

45. Arbab-Zadeh, A. & Fuster, V. The myth of the 'vulnerable plaque': Transitioning from a focus on individual lesions to atherosclerotic disease burden for coronary artery disease risk assessment. *Journal of the American College of Cardiology* **65,** 846–855 (2015).

46. Adamson, P. D., Dweck, M. R. & Newby, D. E. The vulnerable atherosclerotic plaque : in vivo identification and potential therapeutic avenues. *Heart* 1755–1766 (2015). doi:10.1136/heartjnl-2014-307099

47. Tian, J., Ren, X., Vergallo, R., Xing, L., Yu, H., Jia, H., Soeda, T., McNulty, I., Hu, S., Lee, H., Yu, B. & Jang, I. K. Distinct morphological features of ruptured culprit plaque for acute coronary events compared to those with silent rupture and thin-cap fibroatheroma: A combined optical coherence tomography and intravascular ultrasound study. *Journal of the American College of Cardiology* **63,** 2209–2216 (2014).

48. Tanaka, A., Imanishi, T., Kitabata, H., Kubo, T., Takarada, S., Kataiwa, H., Kuroi, A., Tsujioka, H., Tanimoto, T., Nakamura, N., Mizukoshi, M., Hirata, K. & Akasaka, T. Distribution and frequency of thin-capped fibroatheromas and ruptured plaques in the entire culprit coronary artery in patients with acute coronary syndrome as determined by optical coherence tomography. *American Journal of Cardiology* **102,** 975–979 (2008).

49. Shimamura, K., Ino, Y., Kubo, T., Nishiguchi, T., Tanimoto, T., Ozaki, Y., Satogami, K., Orii, M., Shiono, Y., Komukai, K., Yamano, T., Matsuo, Y., Kitabata, H., Yamaguchi, T.,

Hirata, K., *et al.* Difference of ruptured plaque morphology between asymptomatic coronary artery disease and non-ST elevation acute coronary syndrome patients: An optical coherence tomography study. *Atherosclerosis* **235,** 532–537 (2014).

50. Schoenhagen, P., Stone, G. W., Nissen, S. E., Grines, C. L., Griffin, J., Clemson, B. S., Vince, D. G., Ziada, K., Crowe, T., Apperson-Hanson, C., Kapadia, S. R. & Tuzcu, E. M. Coronary plaque morphology and frequency of ulceration distant from culprit lesions in patients with unstable and stable presentation. *Arteriosclerosis, Thrombosis, and Vascular Biology* **23,** 1895–1900 (2003).

51. Cheruvu, P. K., Finn, A. V., Gardner, C., Caplan, J., Goldstein, J., Stone, G. W., Virmani, R. & Muller, J. E. Frequency and Distribution of Thin-Cap Fibroatheroma and Ruptured Plaques in Human Coronary Arteries. A Pathologic Study. *Journal of the American College of Cardiology* **50,** 940–949 (2007).

52. Burke, A. P., Kolodgie, F. D., Farb, A., Weber, D. K., Malcom, G. T., Smialek, J. & Virmani, R. Healed plaque ruptures and sudden coronary death: Evidence that subclinical rupture has a role in plaque progression. *Circulation* **103,** 934–940 (2001).

53. Mann, J. & Davies, M. J. Mechanisms of progression in native coronary artery disease: Role of healed plaque disruption. *Heart* **82,** 265–268 (1999).

54. Williams, M. C., Moss, A. J., Dweck, M., Adamson, P. D., Alam, S., Hunter, A., Shah, A. S. V., Pawade, T., Weir-McCall, J. R., Roditi, G., van Beek, E. J. R., Newby, D. E. & Nicol, E. D. Coronary Artery Plaque Characteristics Associated With Adverse Outcomes in the SCOT-HEART Study. *Journal of the American College of Cardiology* **73,** 291–301 (2019).

55. Williams, M. C., Kwiecinski, J., Doris, M., McElhinney, P., D'Souza, M. S., Cadet, S., Adamson, P. D., Moss, A. J., Alam, S., Hunter, A., Shah, A. S. V., Mills, N. L., Pawade, T., Wang, C., Weir McCall, J., *et al.* Low-Attenuation Noncalcified Plaque on Coronary Computed Tomography Angiography Predicts Myocardial Infarction: Results from the Multicenter SCOT-HEART Trial (Scottish Computed Tomography of the HEART). *Circulation* 1452–1462 (2020). doi:10.1161/CIRCULATIONAHA.119.044720

56. Brezinski, M. E., Tearney, G. J., Weissman, N. J., Boppart, S. A., Bouma, B. E., Hee, M. R., Weyman, A. E., Swanson, E. A., Southern, J. F. & Fujimoto, J. G. Assessing

atherosclerotic plaque morphology: comparison of optical coherence tomography and high frequency intravascular ultrasound. *Heart* **77,** 397–403 (1997).

57. Tanaka, A., Tearney, G. J. & Bouma, B. E. Challenges on the frontier of intracoronary imaging: atherosclerotic plaque macrophage measurement by optical coherence tomography. *Journal of Biomedical Optics* **15,** (2010).

58. Libby, P., Loscalzo, J., Ridker, P. M., Farkouh, M. E., Hsue, P. Y., Fuster, V., Hasan, A. A. & Amar, S. Inflammation, Immunity, and Infection in Atherothrombosis. *Journal of the American College of Cardiology* **72,** 2071–2081 (2018).

59. Ridker, P. M., Everett, B. M., Thuren, T., MacFadyen, J. G., Chang, W. H., Ballantyne, C., Fonseca, F., Nicolau, J., Koenig, W., Anker, S. D., Kastelein, J. J. P., Cornel, J. H., Pais, P., Pella, D., Genest, J., *et al.* Antiinflammatory therapy with canakinumab for atherosclerotic disease. *New England Journal of Medicine* **377,** 1119–1131 (2017).

60. Ridker, P. M., Danielson, E., Fonseca, F. A. H., Genest, J., Gotto, A. M., Kastelein, J. J. P., Koenig, W., Libby, P., Lorenzatti, A. J., MacFadyen, J. G., Nordestgaard, B. G., Shepherd, J., Willerson, J. T. & Glynn, R. J. Rosuvastatin to Prevent Vascular Events in Men and Women with Elevated C-Reactive Protein. *New England Journal of Medicine* **359,** 2195–2207 (2008).

61. Ridker, P. M. A test in context: High-sensitivity C-reactive protein. *Journal of the American College of Cardiology* **67,** 712–723 (2016).

62. Ridker, P. M., MacFadyen, J. G., Everett, B. M., Libby, P., Thuren, T., Glynn, R. J., Kastelein, J., Koenig, W., Genest, J., Lorenzatti, A., Varigos, J., Siostrzonek, P., Sinnaeve, P., Fonseca, F., Nicolau, J., *et al.* Relationship of C-reactive protein reduction to cardiovascular event reduction following treatment with canakinumab: a secondary analysis from the CANTOS randomised controlled trial. *The Lancet* **391,** 319–328 (2018).

63. Libby, P. Interleukin-1 Beta as a Target for Atherosclerosis Therapy: Biological Basis of CANTOS and Beyond. *Journal of the American College of Cardiology* **70,** 2278–2289 (2017).

64. Huang, D., Swanson, E. A., Lin, C. P., Schuman, J. S., Stinson, W. G., Chang, W., Hee, M. R., Flotte, T., Gregory, K., Puliafito, C. A. & Fujimoto, J. G. Optical Coherence

Tomography. *Science* **254,** 1178–1181 (1991).

65. Serranho, P., Morgado, A. M. & Bernardes, R. in *Optical Coherence Tomography* 139–156 (2012). doi:10.1007/978-3-319-06419-2

66. Gambichler, T., Jaedicke, V. & Terras, S. Optical coherence tomography in dermatology: technical and clinical aspects. *Archives of Dermatological Research* **303,** 457–473 (2011).

67. Brezinski, M. E. & Fujimoto, J. G. Optical Coherence Tomography : High-Resolution Imaging in Nontransparent Tissue. *IEEE Journal of Selected Topics in Quantum Electronics* **5,** 1185–1192 (1999).

68. Bezerra, H. G., Costa, M. A., Guagliumi, G., Rollins, A. M. & Simon, D. I. Intracoronary Optical Coherence Tomography: A Comprehensive Review. *JACC: Cardiovascular Interventions* **2,** 1035–1046 (2009).

69. Fercher, A. F. & Roth, E. Ophthalmic laser interferometry. in *Proceedings of the SPIE—The International Society for Optical Engineering* (ed. Mueller, G. J.) 48–51 (International Society for Optics and Photonics, 1986). doi:10.1117/12.938523

70. Fercher, A. F., Mengedoht, K. & Werner, W. Eye-length measurement by interferometry with partially coherent light. *Optics letters* **13,** 186–188 (1988).

71. Fercher, A. F. Optical coherence tomography. *Journal of Biomedical Optics* **1,** 157 (1996).

72. Fercher, A. F., Hitzenberger, C. K., Drexler, W., Kamp, G. & Sattmann, H. In Vivo Optical Coherence Tomography. *American Journal of Ophthalmology* **116,** 113–114 (1993).

73. Swanson, E. A., Izatt, J. A., Hee, M. R., Huang, D., Lin, C. P., Schuman, J. S., Puliafito, C. A. & Fujimoto, J. G. In vivo retinal imaging by optical coherence tomography. *Optics letters* **18,** 1864–1866 (1993).

74. Brezinski, M. E., Tearney, G. J., Bouma, B. E., Boppart, S. A., Hee, M. R., Swanson, E. A., Southern, J. F. & Fujimoto, J. G. Imaging of Coronary Artery Microstructure (In Vitro) With Optical Coherence Tomography. *American Journal of Cardiology* **77,** 92–93 (1996).

75. Gonzalo, N. Optical Coherence Tomography for the Assessment of Coronary

Atherosclerosis and Vessel Response after Stent Implantation. (2010).

76. Choma, M., Sarunic, M., Yang, C. & Izatt, J. Sensitivity advantage of swept source and Fourier domain optical coherence tomography. *Optics Express* **11,** 2183–2189 (2003).

77. Leitgeb, R., Hitzenberger, C. K. & Fercher, A. F. Performance of fourier domain vs. time domain optical coherence tomography. *Optics express* **11,** 889–894 (2003).

78. de Boer, J. F., Cense, B., Park, B. H., Pierce, M. C., Tearney, G. J. & Bouma, B. E. Improved signal-to-noise ratio in spectral-domain compared with time-domain optical coherence tomography. *Optics letters* **28,** 2067–2069 (2003).

79. Schaar, J. A., Muller, J. E., Falk, E., Virmani, R., Fuster, V., Serruys, P. W., Colombo, A., Stefanadis, C., Casscells, S. W., Moreno, P. R., Maseri, A. & van der Steen, A. F. W. Terminology for high-risk and vulnerable coronary artery plaques. *European Heart Journal* **25,** 1077–1082 (2004).

80. Cilingiroglu, M., Oh, J. H., Sugunan, B., Kemp, N. J., Kim, J., Lee, S., Zaatari, H. N., Escobedo, D., Thomsen, S., Milner, T. E. & Feldman, M. D. Detection of Vulnerable Plaque in a Murine Model of Atherosclerosis With Optical Coherence Tomography. *Catheterization and Cardiovascular Interventions* **67,** 915–923 (2006).

81. Pande, A. N., Kohler, R. H., Aikawa, E., Weissleder, R. & Jaffer, F. A. Detection of macrophage activity in atherosclerosis in vivo using multichannel, high-resolution laser scanning fluorescence microscopy. *Journal of biomedical optics* **11,** 021009 (2006).

82. Nam, H. S., Song, J. W., Jang, S.-J., Lee, J. J., Oh, W.-Y., Kim, J. W. & Yoo, H. Characterization of lipid-rich plaques using spectroscopic optical coherence tomography. *Journal of Biomedical Optics* **21,** 075004 (2016).

83. Tahara, S., Morooka, T., Wang, Z., Bezerra, H. G., Rollins, A. M., Simon, D. I. & Costa, M. A. Intravascular optical coherence tomography detection of atherosclerosis and inflammation in Murine aorta. *Arteriosclerosis, Thrombosis, and Vascular Biology* **32,** 1150–1157 (2012).

84. van der Meer, F. J., Faber, D. J., Baraznji Sassoon, D. M., Aalders, M. C., Pasterkamp, G., van Leeuwen, T. G., Sassoon, D. M. B., Aalders, M. C., Pasterkamp, G. & van Leeuwen, T. G. Localized measurement of optical attenuation coefficients of

atherosclerotic plaque constituents by quantitative optical coherence tomography. *IEEE transactions on medical imaging* **24,** 1369–76 (2005).

85. Yonetsu, T., Lee, T., Murai, T., Suzuki, M., Matsumura, A., Hashimoto, Y. & Kakuta, T. Plaque morphologies and the clinical prognosis of acute coronary syndrome caused by lesions with intact fibrous cap diagnosed by optical coherence tomography. *International Journal of Cardiology* **203,** (2016).

86. Zhou, P., Zhu, T., He, C. & Li, Z. Automatic classification of atherosclerotic tissue in intravascular optical coherence tomography images. *Journal of the Optical Society of America A* **34,** 1152 (2017).

87. Yonetsu, T., Kakuta, T., Lee, T., Takahashi, K., Kawaguchi, N., Yamamoto, G., Koura, K., Hishikari, K., Iesaka, Y., Fujiwara, H. & Isobe, M. In vivo critical fibrous cap thickness for rupture-prone coronary plaques assessed by optical coherence tomography. *European Heart Journal* **32,** 1251–1259 (2011).

88. Phipps, J. E., Vela, D., Hoyt, T., Halaney, D. L., Mancuso, J. J., Buja, L. M., Asmis, R., Milner, T. E. & Feldman, M. D. Macrophages and intravascular OCT bright spots: A quantitative study. *JACC: Cardiovascular Imaging* **8,** 63–72 (2015).

89. Tearney, G. J., Yabushita, H., Houser, S. L., Aretz, H. T., Jang, I., Schlendorf, K. H., Kauffman, C. R., Shishkov, M., Halpern, E. F. & Bouma, B. E. Quantification of Macrophage Content in Atherosclerotic Plaques by Optical Coherence Tomography. *Circulation* **107,** 113–119 (2003).

90. Di Vito, L., Agozzino, M., Marco, V., Ricciardi, A., Concardi, M., Romagnoli, E., Gatto, L., Calogero, G., Tavazzi, L., Arbustini, E. & Prati, F. Identification and quantification of macrophage presence in coronary atherosclerotic plaques by optical coherence tomography. *European Heart Journal - Cardiovascular Imaging* **16,** 807–813 (2015).

91. van Soest, G., Goderie, T., Regar, E., Koljenović, S., van Leenders, G. L. J. H., Gonzalo, N., van Noorden, S., Okamura, T., Bouma, B. E., Tearney, G. J., Oosterhuis, J. W., Serruys, P. W. & van der Steen, A. F. W. Atherosclerotic tissue characterization in vivo by optical coherence tomography attenuation imaging. *Journal of Biomedical Optics* **15,** 011105 (2010).

92. MacNeill, B. D., Jang, I.-K., Bouma, B. E., Iftimia, N., Takano, M., Yabushita, H.,

Shishkov, M., Kauffman, C. R., Houser, S. L., Aretz, H. T., DeJoseph, D., Halpern, E. F. & Tearney, G. J. Focal and multi-focal plaque macrophage distributions in patients with acute and stable presentations of coronary artery disease. *Journal of the American College of Cardiology* **44,** 972–979 (2004).

93. Ariza de Schellenberger, A., Poller, W., Stangl, V., Landmesser, U. & Schellenberger, E. Macrophage uptake switches on OCT contrast of superparamagnetic nanoparticles for imaging of atherosclerotic plaques. *International Journal of Nanomedicine* **13,** 7905–7913 (2018).

94. Di Marco, M., Sadun, C., Port, M., Guilbert, I., Couvreur, P. & Dubernet, C. Physicochemical characterization of ultrasmall superparamagnetic iron oxide particles (USPIO) for biomedical application as MRI contrast agents. *International Journal of Nanomedicine* **2,** 609–622 (2007).

95. Daldrup-link, H. E., Golovko, D., Ruffell, B., Denardo, D. G., Castaneda, R., Ansari, C., Rao, J., Tikhomirov, G. A., Wendland, M. F., Corot, C. & Coussens, L. M. MRI of Tumor-Associated Macrophages with Clinically Applicable Iron Oxide Nanoparticles. *American Association for Cancer Research* 5695–5705 (2011). doi:10.1158/1078-0432.CCR-10-3420

96. Muller, K., Skepper, J. N., Posfai, M., Trivedi, R., Howarth, S., Corot, C., Lancelot, E., Thompson, P. W., Brown, A. P. & Gillard, J. H. Effect of ultrasmall superparamagnetic iron oxide nanoparticles (Ferumoxtran-10) on human monocyte-macrophages in vitro. *Biomaterials* **28,** 1629–1642 (2007).

97. Tang, T. Y., Muller, K. H., Graves, M. J., Li, Z. Y., Walsh, S. R., Young, V., Sadat, U., Howarth, S. P. S. & Gillard, J. H. Iron oxide particles for atheroma imaging. *Arteriosclerosis, Thrombosis, and Vascular Biology* **29,** 1001–1008 (2009).

98. Ruehm, S. G., Corot, C., Vogt, P., Kolb, S. & Debatin, J. F. Magnetic resonance imaging of atherosclerotic plaque with ultrasmall superparamagnetic particles of iron oxide in hyperlipidemic rabbits. *Circulation* **103,** 415–422 (2001).

99. Yancy, A. D., Olzinski, A. R., Hu, T. C., Lenhard, S. C., Aravindhan, K., Gruver, S. M., Jacobs, P. M., Willette, R. N. & Jucker, B. M. Differential Uptake of Ferumoxtran-10 and Ferumoxytol , Ultrasmall Superparamagnetic Iron Oxide Contrast Agents in

Rabbit : Critical Determinants of Atherosclerotic Plaque Labeling. *Journal of Magnetic Resonance Imaging* **21,** 432–442 (2005).

100. Hyafil, F., Laissy, J. P., Mazighi, M., Tchétché, D., Louedec, L., Adle-Biassette, H., Chillon, S., Henin, D., Jacob, M. P., Letourneur, D. & Feldman, L. J. Ferumoxtran-10-enhanced MRI of the hypercholesterolemic rabbit aorta: Relationship between signal loss and macrophage infiltration. *Arteriosclerosis, Thrombosis, and Vascular Biology* **26,** 176–181 (2006).

101. Herborn, C. U., Vogt, F. M., Lauenstein, T. C., Dirsch, O., Corot, C., Robert, P. & Ruehm, S. G. Magnetic resonance imaging of experimental atherosclerotic plaque: Comparison of two ultrasmall superparamagnetic particles of iron oxide. *Journal of Magnetic Resonance Imaging* **24,** 388–393 (2006).

102. Litovsky, S., Madjid, M., Zarrabi, A., Casscells, S. W., Willerson, J. T. & Naghavi, M. Superparamagnetic iron oxide-based method for quantifying recruitment of monocytes to mouse atherosclerotic lesions in vivo: Enhancement by tissue necrosis factor-α, interleukin-1β, and interferon-γ. *Circulation* **107,** 1545–1549 (2003).

103. Morris, J. B., Olzinski, A. R., Bernard, R. E., Aravindhan, K., Mirabile, R. C., Boyce, R., Willette, R. N. & Jucker, B. M. p38 MAPK inhibition reduces aortic ultrasmall superparamagnetic iron oxide uptake in a mouse model of atherosclerosis: MRI assessment. *Arteriosclerosis, Thrombosis, and Vascular Biology* **28,** 265–271 (2008).

104. Klug, G., Kampf, T., Ziener, C., Parczyk, M., Bauer, E., Herold, V., Rommel, E., Jakob, P. M. & Bauer, W. R. Murine atherosclerotic plaque imaging with the USPIO Ferumoxtran-10. *Front Biosci (Landmark Ed)* **14,** 2546–2552 (2009).

105. Kooi, M. E. E., Cappendijk, V. C., Cleutjens, K. B. J. M., Kessels, A. G. H., Kitslaar, P. J. E. H. M., Borgers, M., Frederik, P. M., Daemen, M. J. A. P. & Engelshoven, J. M. A. Van. Accumulation of Ultrasmall Superparamagnetic Particles of Iron Oxide in Human Atherosclerotic Plaques Can Be Detected by In Vivo Magnetic Resonance Imaging. *Circulation* **107,** 2453–2459 (2003).

106. Tang, T. Y., Howarth, S. P. S., Miller, S. R., Graves, M. J., U-King-Im, J. M., Trivedi, R. A., Zhi, Y. L., Walsh, S. R., Brown, A. P., Kirkpatrick, P. J., Gaunt, M. E. & Gillard, J. H. Comparison of the inflammatory burden of truly asymptomatic carotid atheroma with

atherosclerotic plaques contralateral to symptomatic carotid stenosis: An ultra small superparamagnetic iron oxide enhanced magnetic resonance study. *Journal of Neurology, Neurosurgery and Psychiatry* **78,** 1337–1343 (2007).

107. Trivedi, R. A., Mallawarachi, C., U-King-Im, J.-M., Graves, M. J., Horsley, J., Goddard, M. J., Brown, A., Wang, L., Kirkpatrick, P. J., Brown, J. & Gillard, J. H. Identifying inflamed carotid plaques using in vivo USPIO-enhanced MR imaging to label plaque macrophages. *Arteriosclerosis, thrombosis, and vascular biology* **26,** 1601–6 (2006).

108. Lutz, A. M., Göpfert, K., Jochum, W., Nanz, D., Fröhlich, J. M. & Weishaupt, D. USPIO-enhanced MR imaging for visualization of synovial hyperperfusion and detection of synovial macrophages: preliminary results in an experimental model of antigen-induced arthritis. *Journal of magnetic resonance imaging : JMRI* **24,** 657–66 (2006).

109. Jo, S.-K., Hu, X., Kobayashi, H., Lizak, M., Miyaji, T., Koretsky, A. & Star, R. a. Detection of inflammation following renal ischemia by magnetic resonance imaging. *Kidney international* **64,** 43–51 (2003).

110. Corot, C., Petry, K. G., Trivedi, R., Saleh, A., Jonkmanns, C., Le Bas, J.-F., Blezer, E., Rausch, M., Brochet, B., Foster-Gareau, P., Balériaux, D., Gaillard, S. & Dousset, V. Macrophage Imaging in Central Nervous System and in Carotid Atherosclerotic Plaque Using Ultrasmall Superparamagnetic Iron Oxide in Magnetic Resonance Imaging. *Investigative Radiology* **39,** (2004).

111. Alam, S. R., Stirrat, C., Richards, J., Mirsadraee, S., Semple, S. I. K., Tse, G., Henriksen, P. & Newby, D. E. Vascular and plaque imaging with ultrasmall superparamagnetic particles of iron oxide. *Journal of Cardiovascular Magnetic Resonance* 1–9 (2015). doi:10.1186/s12968-015-0183-4

112. Hsiao, J. K., Chu, H. H., Wang, Y. H., Lai, C. W., Chou, P. T., Hsieh, S. T., Wang, J. L. & Liu, H. M. Macrophage physiological function after superparamagnetic iron oxide labeling. *NMR in Biomedicine* (2008). doi:10.1002/nbm.1260

113. Oude Engberink, R. D., Van Der Pol, S. M. A., Döpp, E. A., De Vries, H. E. & Blezer, E. L. A. Comparison of SPIO and USPIO for in vitro labeling of human monocytes: MR detection and cell function. *Radiology* (2007). doi:10.1148/radiol.2432060120

114. Beduneau, A., Ma, Z., Grotepas, C. B., Kabanov, A., Rabinow, B. E., Gong, N., Mosley,

R. L., Dou, H., Boska, M. D. & Gendelman, H. E. Facilitated monocyte-macrophage uptake and tissue distribution of superparmagnetic iron-oxide nanoparticles. *PLoS ONE* (2009). doi:10.1371/journal.pone.0004343

115. Weissleder, R., Nahrendorf, M. & Pittet, M. J. Imaging macrophages with nanoparticles. *Nature materials* **13,** 125–138 (2014).

116. Bullivant, J. P., Zhao, S., Willenberg, B. J., Kozissnik, B., Batich, C. D. & Dobson, J. Materials Characterization of Feraheme / Ferumoxytol and Preliminary Evaluation of Its Potential for Magnetic Fluid Hyperthermia. *International Journal of Molecular Sciences* **14,** 17501–17510 (2013).

117. Lu, M., Cohen, M. H., Rieves, D. & Pazdur, R. FDA report: Ferumoxytol for intravenous iron therapy in adult patients with chronic kidney disease. *American Journal of Hematology* **85,** 315–319 (2010).

118. Finn, J. P., Nguyen, K. L., Han, F., Zhou, Z., Salusky, I., Ayad, I. & Hu, P. Cardiovascular MRI with ferumoxytol. *Clinical Radiology* **71,** 796–806 (2016).

119. Fish, W. W. Rapid colorimetric micromethod for quantitation of complexed iron in biological samples. *Methods in Enzymology* **54,** 357–364 (1988).

120. Patil, U. S., Adireddy, S., Jaiswal, A., Mandava, S. & Lee, B. R. In Vitro / In Vivo Toxicity Evaluation and Quantification of Iron Oxide Nanoparticles. *International Journal of Molecular Sciences* **16,** 24417–24450 (2015).

121. Yang, L., Kuang, H., Zhang, W., Aguilar, Z. P., Xiong, Y., Lai, W., Xu, H. & Wei, H. Size dependent biodistribution and toxicokinetics of iron oxide magnetic nanoparticles in mice. *Nanoscale* **7,** 625–636 (2015).

122. Bellusci, M., La Barbera, A., Padella, F., Mancuso, M., Pasquo, A., Grollino, M. G., Leter, G., Nardi, E., Cremisini, C., Giardullo, P. & Pacchierotti, F. Biodistribution and acute toxicity of a nanofluid containing manganese iron oxide nanoparticles produced by a mechanochemical process. *International journal of nanomedicine* **9,** 1919–29 (2014).

123. Di Bona, K. R., Xu, Y., Ramirez, P. A., DeLaine, J., Parker, C., Bao, Y. & Rasco, J. F. Surface charge and dosage dependent potential developmental toxicity and biodistribution of iron oxide nanoparticles in pregnant CD-1 mice. *Reproductive Toxicology* **50,** 36–42 (2014).

124. Kim, J. S., Yoon, T.-J., Yu, K. N., Kim, B. G., Park, S. J., Kim, H. W., Lee, K. H., Park, S. B., Lee, J.-K. & Cho, M. H. Toxicity and tissue distribution of magnetic nanoparticles in mice. *Toxicological sciences : an official journal of the Society of Toxicology* **89,** 338–47 (2006).

125. Neuwelt, E. A., Hamilton, B. E., Varallyay, C. G., Rooney, W. R., Edelman, R. D., Jacobs, P. M. & Watnick, S. G. Ultrasmall superparamagnetic iron oxides (USPIOs): a future alternative magnetic resonance (MR) contrast agent for patients at risk for nephrogenic systemic fibrosis (NSF)? *Kidney International* **75,** 465–474 (2009).

126. Oldenburg, A. L., Hansen, M. N., Zweifel, D. A., Wei, A. & Boppart, S. A. Plasmon-resonant gold nanorods as low backscattering albedo contrast agents for optical coherence tomography. *Optics Express* **14,** 6724 (2006).

127. Ponce De León, Y., Pichardo-Molina, J. L., Alcalá Ochoa, N. & Luna-Moreno, D. Contrast enhancement of optical coherence tomography images using branched gold nanoparticles. *Journal of Nanomaterials* **2012,** (2012).

128. Cang, H., Sun, T., Li, Z.-Y., Chen, J., Wiley, B. J., Xia, Y. & Li, X. Gold nanocages as contrast agents for spectroscopic optical coherence tomography. *Optics Letters* **30,** 3048 (2005).

129. Hu, J., Rivero, F., Torres, R. A., Loro Ramírez, H., Rodríguez, E. M., Alfonso, F., García Solé, J. & Jaque, D. Dynamic single gold nanoparticle visualization by clinical intracoronary optical coherence tomography. *Journal of Biophotonics* **10,** 674–682 (2017).

130. Hu, J., Ortgies, D. H., Aguliar Torres, R., Fernández, N., Porto, L., Martín Rodríguez, E., García Solé, J., Jaque, D., Alfonso, F. & Rivero, F. Quantum Dots Emitting in the Third Biological Window as Bimodal Contrast Agents for Cardiovascular Imaging. *Advanced Functional Materials* **1703276,** 1703276 (2017).

131. Nakashima, Y., Plump, A. S., Raines, E. W., Breslow, J. L. & Ross, R. ApoE-Deficient Mice Develop Lesions of All Phases of Atherosclerosis Throughout the Arterial Tree. *Arteriosclerosis* 133–140 (1994). doi:10.1161/01.ATV.14.1.133

132. Johnson, J. L. & Jackson, C. L. Atherosclerotic plaque rupture in the apolipoprotein E knockout mouse. *Atherosclerosis* **154,** 399–406 (2001).

133. Johnson, J., Carson, K., Williams, H., Karanam, S., Newby, A., Angelini, G., George, S. & Jackson, C. Plaque rupture after short periods of fat feeding in the apolipoprotein E-knockout mouse: Model characterization and effects of pravastatin treatment. *Circulation* **111,** 1422–1430 (2005).

134. Fazio, S., Lee, Y. L., Ji, Z. S. & Rall, S. C. Type III hyperlipoproteinemic phenotype in transgenic mice expressing dysfunctional apolipoprotein E. *Journal of Clinical Investigation* **92,** 1497–1503 (1993).

135. Zhang, S. H., Reddick, R. L., Piedrahita, J. A. & Maeda, N. Spontaneous hypercholesterolemia and arterial lesions in mice lacking apolipoprotein E. *Science* **258,** 468–471 (1992).

136. Coletta, J., Suzuki, N., Nascimento, B. R., Bezerra, H. G., Rosenthal, N., Guagliumi, G., Rollins, A. M. & Costa, M. A. Use of optical coherence tomography for accurate characterization of atherosclerosis. *Arquivos Brasileiros de Cardiologia* **94,** 250–254 (2010).

137. Bezerra, H. G., Attizzani, G. F., Sirbu, V., Musumeci, G., Lortkipanidze, N., Fujino, Y., Wang, W., Nakamura, S., Erglis, A., Guagliumi, G. & Costa, M. A. Optical coherence tomography versus intravascular ultrasound to evaluate coronary artery disease and percutaneous coronary intervention. *JACC: Cardiovascular Interventions* **6,** 228–236 (2013).

138. Takarada, S., Imanishi, T., Liu, Y., Ikejima, H., Tsujioka, H., Kuroi, A., Ishibashi, K., Komukai, K., Tanimoto, T., Ino, Y., Kitabata, H., Kubo, T., Nakamura, N., Hirata, K., Tanaka, A., *et al.* Advantage of next-generation frequency-domain optical coherence tomography compared with conventional time-domain system in the assessment of coronary lesion. *Catheterization and Cardiovascular Interventions* **75,** 202–206 (2010).

139. Raffel, O. C., Tearney, G. J., Gauthier, D. D., Halpern, E. F., Bouma, B. E. & Jang, I.-K. Relationship Between a Systemic Inflammatory Marker, Plaque Inflammation, and Plaque Characteristics Determined by Intravascular Optical Coherence Tomography. *Arteriosclerosis, Thrombosis, and Vascular Biology* **27,** 1820–1827 (2007).

140. Rico-Jimenez, J. J., Campos-Delgado, D. U., Buja, L. M., Vela, D. & Jo, J. A. Intravascular

optical coherence tomography method for automated detection of macrophage infiltration within atherosclerotic coronary plaques. *Atherosclerosis* **290,** 94–102 (2019).

141. Tearney, G. J., Regar, E., Akasaka, T., Adriaenssens, T., Barlis, P., Bezerra, H. G., Bouma, B., Bruining, N., Cho, J. M., Chowdhary, S., Costa, M. A., De Silva, R., Dijkstra, J., Di Mario, C., Dudeck, D., *et al.* Consensus standards for acquisition, measurement, and reporting of intravascular optical coherence tomography studies: A report from the International Working Group for Intravascular Optical Coherence Tomography Standardization and Validation. *Journal of the American College of Cardiology* **59,** 1058–1072 (2012).

142. Liu, X., Deng, R., Zhang, Y., Wang, Y., Chang, H., Huang, L. & Liu, X. Probing the nature of upconversion nanocrystals: instrumentation matters. *Chem. Soc. Rev* **44,** 1479 (2015).

143. Wang, F., Han, Y., Lim, C. S., Lu, Y., Wang, J., Xu, J., Chen, H., Zhang, C., Hong, M. & Liu, X. Simultaneous phase and size control of upconversion nanocrystals through lanthanide doping. *Nature* **463,** 1061–1065 (2010).

144. Nadort, A., Zhao, J. & Goldys, E. M. Lanthanide upconversion luminescence at the nanoscale: fundamentals and optical properties. *Nanoscale* **8,** 13099–13130 (2016).

145. Kanal, E. Gadolinium based contrast agents (GBCA): Safety overview after 3 decades of clinical experience. *Magnetic Resonance Imaging* **34,** 1341–1345 (2016).

146. Milton Harris, J., Martin, N. E. & Modi, M. Pegylation: A novel process for modifying pharmacokinetics. *Clinical Pharmacokinetics* **40,** 539–551 (2001).

147. Milton Harris, J. & Chess, R. B. Effect of pegylation on pharmaceuticals. *Nature Reviews Drug Discovery* **2,** 214–221 (2003).

148. Alconcel, S. N. S., Baas, A. S. & Maynard, H. D. FDA-approved poly(ethylene glycol)-protein conjugate drugs. *Polymer Chemistry* **2,** 1442–1448 (2011).

149. Shalhoub, J., Viiri, L. E., Cross, A. J., Gregan, S. M., Allin, D. M., Astola, N., Franklin, I. J., Davies, A. H. & Monaco, C. Multi-analyte profiling in human carotid atherosclerosis uncovers pro-inflammatory macrophage programming in plaques. *Thrombosis and Haemostasis* 1064–1072 (2006). doi:10.1160/TH15-08-0650

150. Stöger, J. L., Gijbels, M. J. J., van der Velden, S., Manca, M., van der Loos, C. M., Biessen, E. A. L., Daemen, M. J. A. P., Lutgens, E. & de Winther, M. P. J. Distribution of macrophage polarization markers in human atherosclerosis. *Atherosclerosis* **225,** 461–468 (2012).

151. Sternberg, Z., Ghanim, H., Gillotti, K. M., Tario, J. D., Munschauer, F., Curl, R., Noor, S., Yu, J., Ambrus, J. L., Wallace, P. & Dandona, P. Flow cytometry and gene expression profiling of immune cells of the carotid plaque and peripheral blood. *Atherosclerosis* **229,** 338–347 (2013).

152. Moore, K. J. & Tabas, I. Macrophages in the pathogenesis of atherosclerosis. *Cell* **145,** 341–355 (2011).

153. Zheng, W., Huang, P., Tu, D., Ma, E., Zhu, H. & Chen, X. Lanthanide-doped upconversion nano-bioprobes: electronic structures, optical properties, and biodetection. *Chem. Soc. Rev.* **44,** 1379–1415 (2015).

154. Gnanadesigan, M., Kameyama, T., Karanasos, A., Nienke, ;, Van Ditzhuijzen, S., Van Der Sijde, J. N., Van Geuns, R.-J., Ligthart, J., Witberg, K., Ughi, G. J., Antonius, ;, Van Der Steen, F. W., Regar, E., Gijs Van Soest, ; & Akasaka, T. Automated characterisation of lipid core plaques in vivo by quantitative optical coherence tomography tissue type imaging. *EuroIntervention* **12,** 1490–1497 (2016).

155. Ughi, G. J., Adriaenssens, T., Sinnaeve, P., Desmet, W. & D'hooge, J. Automated tissue characterization of in vivo atherosclerotic plaques by intravascular optical coherence tomography images. *Biomedical Optics Express* **4,** 1014 (2013).

156. Rico-Jimenez, J. J., Campos-Delgado, D. U., Villiger, M., Otsuka, K., Bouma, B. E. & Jo, J. A. Automatic classification of atherosclerotic plaques imaged with intravascular OCT. *Biomedical Optics Express* **7,** 4069 (2016).

157. Lee, J., Prabhu, D., Kolluru, C., Gharaibeh, Y., Zimin, V. N., Bezerra, H. G. & Wilson, D. L. Automated plaque characterization using deep learning on coronary intravascular optical coherence tomographic images. *Biomedical Optics Express* **10,** 6497 (2019).

158. Zhou, P., Zhu, T., He, C. & Li, Z. Automatic classification of atherosclerotic tissue in intravascular optical coherence tomography images. *Journal of the Optical Society of America A* **34,** 1152 (2017).

Appendix 1

Matlab code for automated quantification of ROI metrics from images of the Terumo Lunawave™ system (clinical trial data)

```
% OCT Macrophage study: E151502_OCTMA

% PI: Dr Nick Cruden

% Researchers: Simon Wilson, Andrew Mitchell, and Clara Vergez

% Software Version: 6

% Written: 01/03/16

% Updated: 11/05/17

% Written by Dr Calum Gray

% Edited by Clara Vergez

% Clinical Research Imaging Centre (CRIC)

% The following processing is based on the paper: Quantification of Macrophage Content in Atherosclerotic Plaques by Optical Coherence Tomography(Circulation 2003 Tearney.pdf)

clear

clc

software_version = ('v6_terumo_RAW');

%-----------------------------------------------------------------

% Define the empty arrays which will be added to during processing to give a list/table of results

AllSliceNum = []; %List of slice numbers that contained an ROI

AllROINum = []; %List of the ROI/Tag numbers (i.e. objectmap)

AllblobNum = []; %List of the separate blobs comprising the ROI/Tag

AllROI_min = []; %List of min of the ROI

AllROI_max = []; %List of max of the ROI
```

```
AllROI_mean = []; %List of mean of the ROI

AllROI_var = []; %List of variance of the ROI

AllROI_stdev = []; %List of standard deviation of the ROI

AllTotalROIPixels = []; %List of total number of pixels in the ROI

AllROI_NSD = []; %List of Normalised standard deviation of the ROI

AllBackgroundMean = []; %List of mean background noise level

AllNumExcludedPixels = []; %List of the number of excluded pixels in the stats calculations

AllWI_min = []; %List of min within the whole image

AllWI_max = []; %List of max within the whole image

AllWI_NSD = []; %List of Normalised standard deviation (NSD) to the whole image min and
max values

%-----------------------------------------------------------------

% Load image volume & ROI's

% Load volume image

[volume_filename,pathname] = uigetfile('*.hdr','Select the volume file');

% Split into pathname, filename and file extension

[pathname, volume_filename, volume_ext] = fileparts(strcat(pathname,volume_filename));

volume = analyze75read (fullfile(pathname,strcat(volume_filename,volume_ext)));

volume=flip(volume,1);

% Load ROI file

[ROIfilename,ROIpathname] = uigetfile('*.*','Select the ROI file for processing');

% Split into pathname, filename and file extension

[ROIpathname, ROIfilename, ROIext] = fileparts(strcat(ROIpathname,ROIfilename));
```

```
% Check to see if ROI file is in SliceOmatic (.tag) or Analyze (.obj) format

if strcmp(ROIext,'.tag')  % Check if file extension is a tag file

% Load Tag file
[ROI,x_pixel_size,y_pixel_size,z_pixel_size,x_dim,y_dim,z_dim]=ReadTag(fullfile(ROIpathna
me,[ROIfilename ROIext]));

   % convert ROI to type double

   ROI = double(ROI);

   % impixelinfo

else if strcmp(ROIext,'.obj')  % Check if file extension is an objectmap file

% Load objectmap file

      ROI = AVWObjectMap (fullfile(ROIpathname,strcat(ROIfilename,ROIext)));

% Use only the image within the ROI structure

      ROI=ROI.Image;

% Analyze values range from [1 to 256] whereas we want the values in the range [0 to 255]
so that black is '0' - therefore subtract '1' from the ROI image volume to get it in this range

      ROI = ROI-1;

% The Analyze objectmap format does not contain info on pixel size, however it is a 1-to-1
mapping on the .hdr it was created on. Therefore we can use the header info in the volume
file

info = analyze75info(fullfile(pathname,strcat(volume_filename,volume_ext)));

      x_pixel_size = info.PixelDimensions(1);

      y_pixel_size = info.PixelDimensions(2);

      z_pixel_size = info.PixelDimensions(3);

      x_dim = info.Dimensions(1);

      y_dim = info.Dimensions(2);
```

```
        z_dim = info.Dimensions(3);
    else
% ROI file is not a recognised file format and the program will exit
        error('ROI file format not recognised - exiting program ...')
    end
end
% Find the number of slices in the volume (i.e. in the z-axis)
no_of_slices=size(volume,3);
% Find the number of Sliceomatic tags
no_of_ROIs  = max(max(max(ROI)));
% Define the mask of the crosshair annotations to be applied to each OCT image so that they
are excluded from calculations
[OCTCrosshairMask, screenshot] = mask_crosshairs(volume);
% Save screenshot of mask overlaid on image as a 'sanity check'
screenshot_name = strcat(pathname,'\','Crosshair_Mask_Screenshot.jpg');
imwrite(screenshot,screenshot_name)
for i = 1:no_of_ROIs  % for each Tag/ROI
fprintf('Processing ROI no. %d of %d ...\n',i, no_of_ROIs);
    for j = 1:no_of_slices  % for each slice
fprintf('Processing slice no. %d of %d for ROI no. %d ...\n',j, no_of_slices, i);
    ROINum = i;
  SliceNum = j;
        % Select an image slice and ROI
        image = volume(:,:,j);
```

```
    ROI_temp = ROI(:,:,j);
% Test if the current ROI in the loop exists on the current slice (i.e. only make measurements for slice if the ROI/Tag number = i. If not, then move onto the next slice and re-test
    if ismember(i,ROI_temp)
% If the tag/ROI is present in the current image then set the ROI_temp image to only include this tag so that the other tags are not included in the calculation
     ROI_temp = (ROI_temp==i);
%-------- Remove the effect of crosshair annotations from image
% Invert the OCT crosshair mask image
        OCTCrosshairMask2 = 1-OCTCrosshairMask;
%Mask the image with the OCT crosshair mask by setting values outwith the mask to NaN to exclude crosshair annotations from calculations
        image2 = im2double(image);
        image2(OCTCrosshairMask2==0)=NaN;
%-----------------------------------------------------------------
% Set the background default value to zero (in this version, background value is not being measured and subtracted)          BackgroundMean = 0;
%-----------------------------------------------------------------
% Calculate the number of 'blobs' within the slice
        blobs_label = bwlabel(ROI_temp);
        Numblobs = max(max(blobs_label));
        for z = 1:Numblobs
        blobNum = z;
%select each blob individually to process
        blob = (blobs_label==blobNum);
```

```
%-----------------------------------------------------------------

% Calculate the standard deviation within the objectmap/ROI

%change to type double so that we can use NaN's

image3 = double(image2);

        ROI_mask = double(blob);

        ROI_mask(ROI_mask==0)=NaN;

        filter_ROI = image3.*ROI_mask;

% It is very unlikely that there will be 'true' zero values within the image. These may cause issues when calculating statistics therefore it is in practice a good idea to set these to NaN's before calculating stats. However it is also a good idea to record the number of these pixels which have been excluded from the calculation.

        NumExcludedPixels = sum(filter_ROI(:)<=0);

        filter_ROI(filter_ROI<=0)=NaN;

        ROI_min = min(filter_ROI(~isnan(filter_ROI)));  %calculate the min of the ROI

        ROI_max = max(filter_ROI(~isnan(filter_ROI)));  %calculate the max of the ROI

        ROI_mean = mean(filter_ROI(~isnan(filter_ROI)));   %calculate the mean of the ROI

        ROI_var = var(filter_ROI(~isnan(filter_ROI)));   %calculate the variance of the ROI

        ROI_stdev = std(filter_ROI(~isnan(filter_ROI)));  %calculate the standard deviation of the ROI

        TotalROIPixels = sum(ROI_mask(:)==1);

%calculate the number of pixels in the ROI

        ROI_NSD = ROI_stdev / (ROI_max - ROI_min);

%calculate the normalised standard deviation of the OCT signal

%-----------------------------------------------------------------
```

```
% Calculate the Max and Min values of the whole image - the prefix WI_ stands for 'whole
image'
        WI_min = min(image3(image3>0));
%find the minimum 'non zero' value
        WI_max = max(max(image3));
%Calculate the normalised standard deviation of the OCT signal
        WI_NSD = ROI_stdev / (WI_max - WI_min);
%-----------------------------------------------------------------
% Concatenate the cell columns by adding newly read values to previously read values
AllSliceNum = [AllSliceNum ; SliceNum];
AllROINum = [AllROINum ; ROINum];
AllblobNum = [AllblobNum ; blobNum];
AllBackgroundMean = [AllBackgroundMean ; BackgroundMean];
AllROI_min = [AllROI_min ; ROI_min];
AllROI_max = [AllROI_max ; ROI_max];
AllROI_mean = [AllROI_mean ; ROI_mean];
AllROI_var = [AllROI_var ; ROI_var];
AllROI_stdev = [AllROI_stdev ; ROI_stdev];
AllTotalROIPixels = [AllTotalROIPixels ; TotalROIPixels];
AllROI_NSD = [AllROI_NSD ; ROI_NSD];
AllNumExcludedPixels = [AllNumExcludedPixels ; NumExcludedPixels];
AllWI_min = [AllWI_min ; WI_min];
AllWI_max = [AllWI_max ; WI_max];
AllWI_NSD = [AllWI_NSD ; WI_NSD];
```

```
        end
      end
    end
end
%-------------------------------------------------------------------
% Save the results from processing OCT data to a text file
fid_tag_results_file                                                    =
fopen((fullfile(pathname,strcat(volume_filename,'_',software_version,'.txt'))),'at');
   if (fid_tag_results_file < 0)
      error('could not open file "*_results_v6_terumo_RAW.txt"');
   end;
% Write the name of the software
fprintf(fid_tag_results_file, 'OCT Macrophage Study: Metrics for SliceOmatic or Analyze ROI
files \n\n');
% Write the path and filename of the tag file
fprintf(fid_tag_results_file, '%s \n\n',fullfile(ROIpathname,strcat(ROIfilename,ROIext)));
% Write the software version
fprintf(fid_tag_results_file, 'Software Version: %s \n',software_version);
% Write the date data was processed
fprintf(fid_tag_results_file, 'Data Processed: %s \n',date);
% Write the volume dimensions
fprintf(fid_tag_results_file, 'Volume Dimensions: \t');
fprintf(fid_tag_results_file, 'Width=%g \t',x_dim);
fprintf(fid_tag_results_file, 'Height=%g \t',y_dim);
```

```
fprintf(fid_tag_results_file, 'Depth= %g \n',z_dim);

% Write the voxel size

fprintf(fid_tag_results_file, 'Voxel Size: \t');

fprintf(fid_tag_results_file, 'VoxelWidth=%g \t',x_pixel_size);

fprintf(fid_tag_results_file, 'VoxelHeight=%g \t',y_pixel_size);

fprintf(fid_tag_results_file, 'VoxelDepth=%g \n\n',z_pixel_size);

% Write the column headers for the batch_results text file

fprintf(fid_tag_results_file, 'Slice No. \t');

fprintf(fid_tag_results_file, 'Tag No. \t');

fprintf(fid_tag_results_file, 'Blob No. \t');

fprintf(fid_tag_results_file, 'Mean Background Noise Level \t');

fprintf(fid_tag_results_file, 'ROI Min \t');

fprintf(fid_tag_results_file, 'ROI Max \t');

fprintf(fid_tag_results_file, 'ROI Mean \t');

fprintf(fid_tag_results_file, 'ROI Variance \t');

fprintf(fid_tag_results_file, 'ROI Std Dev \t');

fprintf(fid_tag_results_file, 'ROI Total Pixels \t');

fprintf(fid_tag_results_file, 'ROI Normalised Standard Deviation (NSD) \t');

fprintf(fid_tag_results_file, 'No. of Excluded Pixels from ROI Calculation \t');

fprintf(fid_tag_results_file, 'Slice Min \t');

fprintf(fid_tag_results_file, 'Slice Max \t');

fprintf(fid_tag_results_file, 'Slice Normalised Standard Deviation (NSD) \n');

for k = 1:numel(AllSliceNum)

%   Write the Image Metrics results to the text file
```

```
fprintf(fid_tag_results_file, '%d \t', AllSliceNum(k));

fprintf(fid_tag_results_file, '%d \t', AllROINum(k));

fprintf(fid_tag_results_file, '%d \t', AllblobNum(k));

fprintf(fid_tag_results_file, '%f \t', AllBackgroundMean(k));

fprintf(fid_tag_results_file, '%f \t', AllROI_min(k));

fprintf(fid_tag_results_file, '%f \t',  AllROI_max(k));

fprintf(fid_tag_results_file, '%f \t', AllROI_mean(k));

fprintf(fid_tag_results_file, '%f \t', AllROI_var(k));

fprintf(fid_tag_results_file, '%f \t', AllROI_stdev(k));

fprintf(fid_tag_results_file, '%d \t', AllTotalROIPixels(k));

fprintf(fid_tag_results_file, '%f \t', AllROI_NSD(k));

fprintf(fid_tag_results_file, '%d \t', AllNumExcludedPixels(k));

fprintf(fid_tag_results_file, '%f \t', AllWI_min(k));

fprintf(fid_tag_results_file, '%f \t',  AllWI_max(k));

fprintf(fid_tag_results_file, '%f \n', AllWI_NSD(k));

end

fclose(fid_tag_results_file);
```

APPENDIX 2

Matlab code for automated quantification of ROI metrics from images of the Ilumien Optis™ system (in-vitro phantoms and ex-vivo mouse data)

```
% OCT Macrophage study: E151502_OCTMA

% PI: Dr Nick Cruden

% Researchers: Simon Wilson, Andrew Mitchell, and Clara Vergez

% Software Version: 5

% Written: 01/03/16

% Updated: 10/05/17

% Written by Dr Calum Gray

% Edited by Clara Vergez (simplification)

% Clinical Research Imaging Centre (CRIC)

% The following processing is based on the paper: Quantification of Macrophage Content in Atherosclerotic Plaques by Optical Coherence Tomography (Circulation 2003 Tearney.pdf)

**********************************************************************

clear

clc

software_version = ('v5_jude_RAW');

%----------------------------------------------------------------

% Define the empty arrays which will be added to during processing to give a list/table of results (to be written to Excel spreadsheet)

AllSliceNum = []; %List of slice numbers that contained an ROI

AllROINum = []; %List of the ROI/Tag numbers (i.e. objectmap)

AllblobNum = []; %List of the separate blobs comprising the ROI/Tag
```

```
AllROI_min = []; %List of min of the ROI

AllROI_max = []; %List of max of the ROI

AllROI_mean = []; %List of mean of the ROI

AllROI_var = [];   %List of variance of the ROI

AllROI_stdev = []; %List of standard deviation of the ROI

AllTotalROIPixels = []; %List of total number of pixels in the ROI

AllROI_NSD = []; %List of Normalised standard deviation of the ROI

AllBackgroundMean = []; %List of mean background noise level

AllNumExcludedPixels = []; %List of the number of excluded pixels in the stats calculations

AllWI_min = []; %List of min within the whole image

AllWI_max = []; %List of max within the whole image

AllWI_NSD = []; %List of Normalised standard deviation (NSD) to the whole image min and
max values

%-----------------------------------------------------------------

% Load volume image (to remove for multiple files)

[volume_filename,pathname] = uigetfile('*.hdr','Select the volume file');

% Split into pathname, filename and file extension

[pathname, volume_filename, volume_ext] = fileparts(strcat(pathname,volume_filename));

volume = analyze75read (fullfile(pathname,strcat(volume_filename,volume_ext)));

volume=flip(volume,1);

%-----------------------------------------------------------------

% Load ROI file

[ROIfilename,ROIpathname] = uigetfile('*.*','Select the ROI file for processing');

% Split into pathname, filename and file extension
```

```
[ROIpathname, ROIfilename, ROIext] = fileparts(strcat(ROIpathname,ROIfilename));
    % Analyze objectmap file format
    ROI = AVWObjectMap (fullfile(ROIpathname,strcat(ROIfilename,ROIext)));
    % Use only the image within the ROI structure
    ROI=ROI.Image;
% Analyze values range from [1 to 256] whereas we want the values in the range [0 to 255] so that black is '0' - therefore subtract '1' from the ROI image volume to get it in this range
    ROI = ROI-1;
% The Analyze objectmap format does not contain info on pixel size, however it is a 1-to-1 mapping on the hdr it was created on. Therefore we can use the header info in the volume file
info = analyze75info(fullfile(pathname,strcat(volume_filename,volume_ext));
    x_pixel_size = info.PixelDimensions(1);
    y_pixel_size = info.PixelDimensions(2);
    z_pixel_size = info.PixelDimensions(3);
    x_dim = info.Dimensions(1);
    y_dim = info.Dimensions(2);
    z_dim = info.Dimensions(3);
% Find the number of slices in the volume (i.e. in the z-axis)
no_of_slices=size(volume,3);
% Find the number of tags
no_of_ROIs  = max(max(max(ROI)));
for i = 1:no_of_ROIs  % for each Tag/ROI
fprintf('Processing ROI no. %d of %d ...\n',i, no_of_ROIs);
```

```
   for j = 1:no_of_slices  % for each slice
fprintf('Processing slice no. %d of %d for ROI no. %d ...\n',j, no_of_slices, i);
   ROINum = i;
 SliceNum = j;
      % Select an image slice and ROI
      image = volume(:,:,j);
      ROI_temp = ROI(:,:,j);
% Test if the current ROI in the loop exists on the current slice (i.e. only make measurements for slice if the ROI/Tag number = i). If not, then move onto the next slice and re-test
      if ismember(i,ROI_temp)
% If the tag/ROI is present in the current image then set the ROI_temp image to only include this tag so that the other tags are also not included in the calculation
        ROI_temp = (ROI_temp==i);
         image2 = im2double(image);
%--------------------------------------------------------------------
% Set the background default value to zero (in this version, background value is not being measured and subtracted)
         BackgroundMean = 0;
%--------------------------------------------------------------------
% Calculate the number of 'blobs' within the slice
         blobs_label = bwlabel(ROI_temp);
         Numblobs = max(max(blobs_label));
         for z = 1:Numblobs
         blobNum = z;
         blob = (blobs_label==blobNum);
```

```
%select each blob individually to process

%-------------------------------------------------------------------

% Calculate the standard deviation within the objectmap/ROI

        image3 = double(image2);

%change to type double so that we can use NaN's

        ROI_mask = double(blob);

%change to type double so that we can use NaN's

        ROI_mask(ROI_mask==0)=NaN;

        filter_ROI = image3.*ROI_mask;

% It is very unlikely that there will be 'true' zero values within the image. These may cause issues when calculating statistics therefore it is in practice a good idea to set these to NaN's before calculating stats. However it is also a good idea to note/record the number of these pixels which have been excluded from the calculation.

        NumExcludedPixels = sum(filter_ROI(:)<=0);

        filter_ROI(filter_ROI<=0)=NaN;

        ROI_min = min(filter_ROI(~isnan(filter_ROI)));  %calculate the min of the ROI

        ROI_max = max(filter_ROI(~isnan(filter_ROI)));  %calculate the max of the ROI

        ROI_mean = mean(filter_ROI(~isnan(filter_ROI)));   %calculate the mean of the ROI

        ROI_var = var(filter_ROI(~isnan(filter_ROI)));   %calculate the variance of the ROI

        ROI_stdev = std(filter_ROI(~isnan(filter_ROI)));  %calculate the standard deviation of the ROI

        TotalROIPixels = sum(ROI_mask(:)==1); %calculate the number of pixels in the ROI (i.e. within the masked area)

        ROI_NSD = ROI_stdev / (ROI_max - ROI_min);

%calculate the normalised standard deviation of the OCT signal
```

```
%-----------------------------------------------------------------

%Find the NSD value using the min & max values of the whole image (WI) rather than just
the max & min of the ROI (WI_NSD).

        WI_min = min(image3(image3>0));

        WI_max = max(max(image3));

% Calculate the normalised standard deviation of the OCT signal

        WI_NSD = ROI_stdev / (WI_max - WI_min);

%-----------------------------------------------------------------

% Concatenate the cell columns by adding newly read values to previously read values

AllSliceNum = [AllSliceNum ; SliceNum];

AllROINum = [AllROINum ; ROINum];

AllblobNum = [AllblobNum ; blobNum];

AllBackgroundMean = [AllBackgroundMean ; BackgroundMean];

AllROI_min = [AllROI_min ; ROI_min];

AllROI_max = [AllROI_max ; ROI_max];

AllROI_mean = [AllROI_mean ; ROI_mean];

AllROI_var = [AllROI_var ; ROI_var];

AllROI_stdev = [AllROI_stdev ; ROI_stdev];

AllTotalROIPixels = [AllTotalROIPixels ; TotalROIPixels];

AllROI_NSD = [AllROI_NSD ; ROI_NSD];

AllNumExcludedPixels = [AllNumExcludedPixels ; NumExcludedPixels];

AllWI_min = [AllWI_min ; WI_min];

AllWI_max = [AllWI_max ; WI_max];

AllWI_NSD = [AllWI_NSD ; WI_NSD];
```

```
        end
      end
    end
end
%-------------------------------------------------------------------
% Save the results from processing OCT data to a text file
fid_tag_results_file                                                    =
fopen((fullfile(pathname,strcat(volume_filename,'_',software_version,'.txt'))),'at');
   if (fid_tag_results_file < 0)
      error('could not open file "*_results_v5_jude_RAW.txt"');
   end;
% Write the name of the software
fprintf(fid_tag_results_file, 'OCT Macrophage Study: Metrics for Analyze ROI files \n\n');
% Write the path and filename of the tag file
fprintf(fid_tag_results_file, '%s \n\n',fullfile(ROIpathname,strcat(ROIfilename,ROIext)));
% Write the software filename
fprintf(fid_tag_results_file, 'Software name: %s.m \n',mfilename);
% Write the software version
fprintf(fid_tag_results_file, 'Software Version: %s \n',software_version);
% Write the date data was processed
fprintf(fid_tag_results_file, 'Data Processed: %s \n',date);
% Write the volume dimensions
fprintf(fid_tag_results_file, 'Volume Dimensions: \t');
fprintf(fid_tag_results_file, 'Width=%g \t',x_dim);
```

```
fprintf(fid_tag_results_file, 'Height=%g \t',y_dim);

fprintf(fid_tag_results_file, 'Depth= %g \n',z_dim);

% Write the voxel size

fprintf(fid_tag_results_file, 'Voxel Size: \t');

fprintf(fid_tag_results_file, 'VoxelWidth=%g \t',x_pixel_size);

fprintf(fid_tag_results_file, 'VoxelHeight=%g \t',y_pixel_size);

fprintf(fid_tag_results_file, 'VoxelDepth=%g \n\n',z_pixel_size);

% Write the column headers for the batch_results text file

fprintf(fid_tag_results_file, 'Slice No. \t');

fprintf(fid_tag_results_file, 'Tag No. \t');

fprintf(fid_tag_results_file, 'Blob No. \t');

fprintf(fid_tag_results_file, 'Mean Background Noise Level \t');

fprintf(fid_tag_results_file, 'ROI Min \t');

fprintf(fid_tag_results_file, 'ROI Max \t');

fprintf(fid_tag_results_file, 'ROI Mean \t');

fprintf(fid_tag_results_file, 'ROI Variance \t');

fprintf(fid_tag_results_file, 'ROI Std Dev \t');

fprintf(fid_tag_results_file, 'ROI Total Pixels \t');

fprintf(fid_tag_results_file, 'ROI Normalised Standard Deviation (NSD) \t');

fprintf(fid_tag_results_file, 'No. of Excluded Pixels from ROI Calculation \t');

fprintf(fid_tag_results_file, 'Slice Min \t');

fprintf(fid_tag_results_file, 'Slice Max \t');

fprintf(fid_tag_results_file, 'Slice Normalised Standard Deviation (NSD) \n');
```

```
for k = 1:numel(AllSliceNum)

%   Write the Image Metrics results to the text file

fprintf(fid_tag_results_file, '%d \t', AllSliceNum(k));

fprintf(fid_tag_results_file, '%d \t', AllROINum(k));

fprintf(fid_tag_results_file, '%d \t', AllblobNum(k));

fprintf(fid_tag_results_file, '%f \t', AllBackgroundMean(k));

fprintf(fid_tag_results_file, '%f \t', AllROI_min(k));

fprintf(fid_tag_results_file, '%f \t',  AllROI_max(k));

fprintf(fid_tag_results_file, '%f \t', AllROI_mean(k));

fprintf(fid_tag_results_file, '%f \t', AllROI_var(k));

fprintf(fid_tag_results_file, '%f \t', AllROI_stdev(k));

fprintf(fid_tag_results_file, '%d \t', AllTotalROIPixels(k));

fprintf(fid_tag_results_file, '%f \t', AllROI_NSD(k));

fprintf(fid_tag_results_file, '%d \t', AllNumExcludedPixels(k));

fprintf(fid_tag_results_file, '%f \t', AllWI_min(k));

fprintf(fid_tag_results_file, '%f \t',  AllWI_max(k));

fprintf(fid_tag_results_file, '%f \n', AllWI_NSD(k));

end

%close the text results file

fclose(fid_tag_results_file);
```

APPENDIX 3

Matlab code for automated production of SD hotspot maps for images from both Terumo and St Jude OCT systems

```
% OCT Macrophage study: E151502_OCTMA

% PI: Dr Nick Cruden

% Researchers: Simon Wilson, Andrew Mitchell, and Clara Vergez

% Software Version: 2

% Written: 05/10/16

% Updated: 01/07/19

% Written by Dr Calum Gray

% Edited and repurposed by Dr Pierre Bagnaninchi and Clara Vergez

% Edinburgh Imaging Facility QMRI

% The following processing is based on the paper: Focal and Multi-Focal Plaque Macrophage Distributions in Patients With Acute and Stable Presentations of Coronary Artery Disease (OCT_Macrophage_distribution_colourmap.pdf)

clear

clc

close all;

opengl hardware

opengl info

% Sweeping block size to adjust: use 9 for st jude images (phantoms and mice) and 5 for terumo images (clinical trial)

STD_block_zize =9;
```

```
%-----------------------------------------------------------------

% Add Matlab paths required to run code

% Determine where this m-file's folder is.

folder = fileparts(which(mfilename));

% Add that folder plus all subfolders to the path.

addpath(genpath(folder));

%-----------------------------------------------------------------

% Load volume image

[volume_filename,pathname] = uigetfile('*.tif','Select the volume file');

% Split into pathname, filename and file extension

[pathname, volume_filename, volume_ext] = fileparts(strcat(pathname,volume_filename));

volume = imread (fullfile(pathname,strcat(volume_filename,volume_ext)));

% Find the number of slices in the volume (i.e. in the z-axis)

no_of_slices=size(volume,3);

j = 1; %only process a single image

fprintf('Processing Slice no. %d of %d ...\n',j, no_of_slices);

% Select an image slice and ROI

image = volume(:,:,j);

%-----------------------------------------------------------------

image2 = im2double(image);

% Mask the image using user-drawn ROI (as Analyze .obj)

% Load ROI file

[ROI_filename,ROIpathname] = uigetfile('*.obj','Select the volume file');

% Split into pathname, filename and file extension
```

```
[ROIpathname, ROI_filename, ROI_ext] = fileparts(strcat(ROIpathname,ROI_filename));

 ROI = AVWObjectMap (fullfile(ROIpathname,strcat(ROI_filename,ROI_ext)));

% Use only the image within the ROI structure

 ROI=ROI.Image;

% Analyze values range from [1 to 256] whereas we want the values in the range [0 to 255] so that black is '0' - therefore subtract '1' from the ROI image volume to get it in this range

 ROI = ROI-1;

% Make it a binary image (i.e. all pixel values > 1 == 1)

image2(ROI==0)=NaN;

image6 = double(image2); %change to type double so that we can use NaN's

% Calculate the Max and Min values of the whole image (WI) rather than just the max & min of the ROI

WI_min = nanmin(nanmin(image6));  %find the minimum 'non zero' value

WI_max = nanmax(nanmax(image6));

% Custom filter: Standard Deviation

% Create a 'nlfilter' - a General sliding-neighbourhood operation using a function (fun)

% calculate the standard deviation (omitting NaN's in the calculation), divided by the difference between the OCT signal max and min values, multiplied by 100

fun = @(x) (std(x(:),'omitnan')/(WI_max - WI_min))*100;

% Apply filter to a block of neighbouring pixels (of predefined size)

image7 = nlfilter(image6,[STD_block_zize STD_block_zize],fun);

% Create new image comprising variance map image overlaid onto original grayscale image, with a colorbar on the side

% set threshold above which the colormap pixels will be displayed on the grayscale image

ColMapThresh = max(max(image7)).*0.5; % Threshold 50% of the std map
```

```
figure;

ax1 = axes;

imagesc(image,[0 255]);

colormap(ax1,'gray');

ax2 = axes;

imagesc(ax2,image7,'alphadata',image7>ColMapThresh);

% best colour is "hot" but flipped and restricted to 13 colours (st jude) and 20 for terumo

colormap(ax2,flipud(hot(13)));

caxis(ax2, [0 25]) ; % Max and min of axis: To keep axis and colour values the same across different images - For St Jude, set max to 25, for Terumo, 34

ax2.Visible = 'off';

linkprop([ax1 ax2],'Position');

ax1.DataAspectRatioMode = 'manual';

ax2.DataAspectRatioMode = 'manual';

colorbar;

% remove the X & Y axis tick labels

set(ax1,'xticklabel',[])

set(ax1,'yticklabel',[])

set(ax1,'xtick',[])

set(ax1,'ytick',[])


% save the image as a tiff with name of original file and "_map" appended

 mapfigname = strcat(volume_filename,'_','map');

 saveas(gcf,mapfigname,'tif')
```